Analysis of extended emission and *Fermi* Bubbles from H.E.S.S. observations in the vicinity of the Galactic Center

Master's Thesis in Physics

Presented by

Fabian Richter

July 1, 2022

Erlangen Centre for Astroparticle Physics

Friedrich-Alexander-Universität Erlangen-Nürnberg

Supervisor: Prof. Dr. Stefan Funk
Co-advisor: Dr. Dmitry Malyshev

Abstract

In 2010, *Fermi*-LAT observations revealed a bilobular shaped large-scale emission in the γ-ray sky extending 55° above and below the Galactic center (GC). The origin of this remarkable feature is unresolved to this day. In this thesis, H.E.S.S. observations from 2004 to 2019 between $\approx$ 300 GeV and 100 TeV, i.e. in an energy range where *Fermi*-LAT has low statistics, are analysed with the HAP-HD chain. Data in a Region of interest (ROI) spanning $\pm 10°$ in galactic longitude and $\pm 5°$ in galactic latitude are taken into account for the analysis.

In a first approach, *Fermi* Bubbles emission is searched in HESS I data. Therefore, all known γ-ray emitting sources in the ROI (astrophysical sources detected by H.E.S.S. and the *Central molecular zone*) are modelled. No clear correlation between the residuals observed in this analysis and the *Fermi* Bubbles can be stated.

The main *Fermi* Bubbles analysis is performed using HESS Iu Inner Galaxy Survey (IGS) runs since these runs are taken in close vicinity of the location of the *Fermi* Bubbles as expected from *Fermi*-LAT observations.

Two different analyses are performed for HESS Iu data: In the first approach, all known γ-ray emitting sources in the ROI are masked from the analysis. Then, the HAP 3D background model is used to determine residuals in addition to the background. A *Fermi* Bubbles template based on the results from *Fermi*-LAT is built. Inside this template, the spectrum of the *Fermi* Bubbles is computed considering the detected counts and the background counts predicted by the background model. This analysis is referred to as the *Fermi* Bubbles template analysis. In addition, a *Fermi* Bubbles template based on the observed HESS Iu residuals is defined, resulting in a calculated spectrum that is in good agreement with the determined one using the *Fermi*-LAT template. In addition, multiple checks are performed to estimate the statistical and systematic uncertainties of this analysis. Results from HESS I and II are used as a cross-check and turn out to be consistent with the HESS Iu analysis. Finally, an analysis using combined HESS I, II and Iu data is performed.

The second approach is to apply models to all γ-ray emitting sources in the ROI similar to the HESS I analysis carried out first. For HESS Iu data, a Gaussian spatial model is added to describe the emission in the vicinity of the expected *Fermi* Bubbles. The results of both analyses inside the *Fermi*-LAT data-based *Fermi* Bubbles template are consistent for HESS Iu data within the uncertainties.

Moreover, the results from the HAP HESS Iu *Fermi* Bubbles template analyses are in accordance with data achieved using the PA analysis pipeline and 2014 to 2020 H.E.S.S. data. At energies between 1 and 10 TeV, a statistically significant signal above the systematic uncertainties in the computed HAP HESS Iu spectrum using std ImPACT is observed. For the analysis with std zeta, the statistical significance of the flux is comparable to the one achieved with the std ImPACT analysis, but systematic uncertainties are approximately in the same order of magnitude as the flux points above 2 TeV. Interestingly, no cutoff in the HAP HESS Iu spectra is found.

Contents

1. Introduction

In 1912, Viktor F. Hess made seven balloon flights between April and August. His objective was to investigate the height dependence of the measured γ-radiation rate. Therefore, Hess used detectors containing ionisation sources that were stimulated by incoming ionising γ-radiation and consecutively produced ions. Measuring the saturation current generated by these ions, it is possible to determine the density of ionising γ-radiation. During his last balloon flight, Hess reached a maximum height of almost 5400 meters. Former experiments aiming to measure the density of ionising radiation have been performed at different heights of skyscrapers like the Eiffel Tower. The results of these measurements suggested that the investigated density decreases as height increases. Hess could confirm these results up to heights of 1400 meters. However, above altitudes of more than 2500 meters, he observed an exponential growth of ionising γ-radiation rate [1]. Hence, he concluded - due to absorption effects of radiation originating at Earth's crust - that radiation with very high penetrating power might enter Earth's atmosphere from above; for this insight Hess has been awarded the 1936 Nobel Prize in Physics [2].
Hess named the detected radiation *Höhenstrahlung*. Nowadays, it is known as *secondary cosmic radiation*. It is caused by *primary cosmic rays* (CRs) mainly consisting of protons and further ionised particles, mostly alpha particles. After Hess discovered the existence of CRs in our atmosphere, the object of today's research is to study their origin. Investigating the CRs directly to gain information on their origin is impossible due to electromagnetic deflection of charged particles. This is not the case for γ-radiation that is produced by the CRs via leptonic or hadronic processes. Thus, it is possible to determine the originating site of the CRs at relatively high precision via detection of the γ-radiation [3].
The initial γ-radiation can only be detected directly via measurements outside of Earth's atmosphere because of secondary particle production processes - pair-production and Bremsstrahlung - when these γ-rays enter the atmosphere [4]. Consequently, there are two different methods to observe γ-rays.
On the one hand, satellite-based telescopes outside Earth's atmosphere equipped with suitable detectors can be used for a direct measurement of γ-rays. The main problem of these telescopes is the limited detection surface because of the satellite's mass limitation. As a consequence, these space-based telescopes are only sensitive up to ≈ 1 TeV because the photon flux decreases at higher energies requiring larger detection areas [5].
On the other hand, γ-rays can be indirectly detected by ground-based telescopes. One possibility therefore, is to use telescopes that are capable of directly detecting the Cherenkov light of the charged secondary particles produced by the γ-rays entering the atmosphere. Using this strategy, it is possible to reconstruct energy as well as direction of the originally incoming γ-rays. Such telescopes are called *Imaging Atmospheric Cherenkov Telescopes* (IACTs) and can be used to observe γ-rays in the *Very High Energy* (VHE) range, i.e. from approximately 100 GeV up to 100 TeV [6].
An example for satellite-based telescopes is the *Fermi Gamma-ray Space Telescope* [1]. Its main instrument for detection of γ-rays is called *Large Area Telescope* (LAT). It has been launched in 2008 and observes electromagnetic radiation at energies from ≈ 50 MeV up to 1 or 2 TeV. Only low statistics are available at the highest detectable energies. It revealed one of the greatest mysteries in the γ-ray sky, the *Fermi* Bubbles.
In 2010, Dobler et al. [7] stated that a diffuse γ-ray signal in the inner part of the *Milky Way* has been detected by *Fermi*-LAT. The observed spatial morphology resembles the one of the microwave haze that has been observed by the *Wilkinson Microwave Anisotropy Probe* (WMAP)

[1] `https://fermi.gsfc.nasa.gov/`

[2], making the found γ-rays a possible counterpart of the microwave emission. However, *Fermi* Bubbles are a bilobular-shaped large-scale emission extending $\approx 50°$ above and below the GC [8]. Their spatial morphology appears symmetric with respect to reflection across the Galactic Plane (GP). Furthermore, the *Fermi* Bubbles have a width of approximately 40° in galactic longitude [9]. The *Fermi* Bubbles lobes additionally show sharp emission edges that might be coincident with X-ray features observed in *ROSAT* [3] data [8], [10]. Furthermore, Crocker et al. [11] suggested that the *S-PASS* radio Lobes (extending up to $|b| < 60°$) may be associated to the *Fermi* Bubbles. The spatial extend of the *Fermi* Bubbles is shown in figure 1 as an artistic impression. The energy injection of both, the upper and the lower structure is $\sim 10^{54} - 10^{55}$ erg [8].

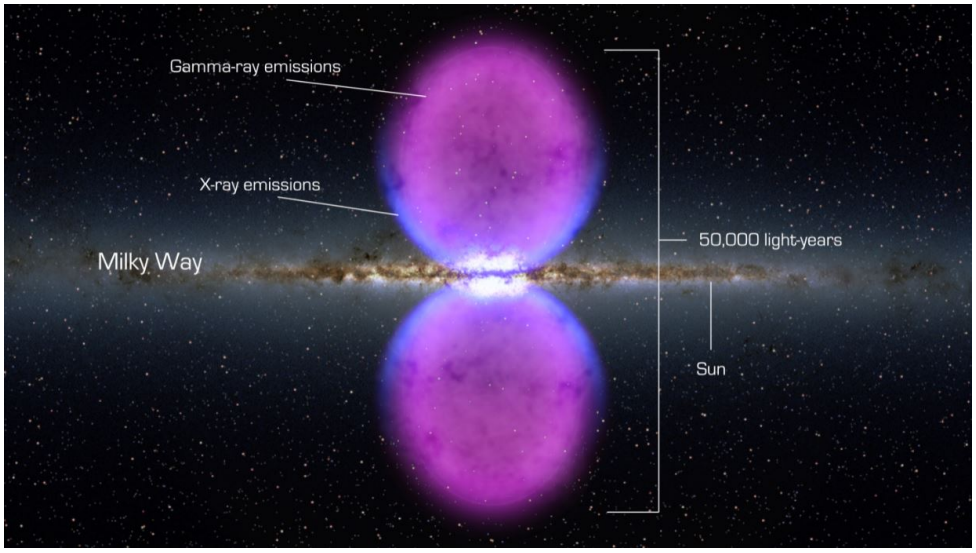

Figure 1: Artistic impression of the *Fermi* Bubbles. The radius of each of the two lobes is ~ 5 kpc, the distance between GC and the sun is ~ 8.5 kpc [8]. The magenta coloured lobes represent the *Fermi* Bubbles γ-ray emission and the blue regions at the edges of the *Fermi* Bubbles the X-ray excess seen by *ROSAT*. Figure taken from [12].

At galactic latitudes $|b| > 10°$, the spectrum of the *Fermi* Bubbles is spatially uniform. It can be described by a power law $\sim E^{-2}$ which is harder than conventional foreground sources [13] and an exponential cutoff at approximately 100 GeV. The low latitude *Fermi* Bubbles, in particular for $|b| < 10°$ are of special interest since they are brighter than those at larger latitudes and their spectrum is harder [14]. Investigating the *Fermi* Bubbles at low latitudes may be a key to resolve their origin that is still not clear. There are different models that aim to describe the *Fermi* Bubbles production mechanism. The two most popular ones are either an *Active galactic nucleus* (AGN) like emission from the *Super massive black hole* (SMBH) SGR A* located at the GC or a starburst close to the GC (both scenarios will be discussed in more detail in section 2.2) [8]. Furthermore, the production mechanism of the γ-ray emission itself remains an open question. The γ-rays can be either of hadronic or leptonic origin. In the hadronic case, CRs interact with surrounding gas, while in the leptonic case the γ-ray emission is produced by *Inverse Compton scattering* (ICS).
In the former process, protons, that have been accelerated by astrophysical sources, interact with the interstellar medium, most likely atomic nuclei or other protons. Decay products of this reaction are pions (π^0, $\pi^{\pm}$). γ-rays are then produced as a consequence of the nearly

[2] `https://map.gsfc.nasa.gov/`
[3] `https://www.mpe.mpg.de/ROSAT`

instantaneous decay of the neutral pion π^0 into 2 γ-quanta (see for example [4, p. 21]) via

$$\pi^0 \rightarrow \gamma + \gamma. \tag{1}$$

However, in the leptonic model, ICS means that the energy of low energetic photons can be increased via scattering processes with high energetic electrons or positrons [15, p. 181]. In this way, electrons that have been emitted by astrophysical accelerators - for example AGNs - interact with photons of the *Interstellar radiation field* (ISRF). The ISRF predominately consists - among others - of the *cosmic microwave background* (CMB), starlight and infrared emission caused by dust [14]. Hadronic and leptonic scenarios regarding the *Fermi* Bubbles will be discussed in section 2.1.

Because of the larger brightness of the low latitude *Fermi* Bubbles, it may be possible to observe them not only using *Fermi*-LAT data, but also in IACT observations at energies above 100 GeV. For this purpose, data of the *High Energy Stereoscopic System* (H.E.S.S.) [4] have been analysed during this thesis in the vicinity of the GC, in particular, in a ROI spanning $\pm 10^\circ$ in galactic longitude and $\pm 5^\circ$ in galactic latitude. More details on the H.E.S.S. telescope array can be found in chapter 3.5.

In the first part of the data analysis, performed with the Python package Gammapy, all γ-ray emitting regions in the whole ROI are investigated using HESS I data; among them astrophysical sources that can be seen by H.E.S.S. and the *central molecular zone* (CMZ), a region close to the GC that is outstanding because of its high hydrogen density. After all these sources have been modelled, three regions with remaining diffuse γ-ray emission are observed. Since the connection to the *Fermi* Bubbles is not yet clear for these diffuse emission regions, they are not referred to as *Fermi* Bubbles at this point, but more general as extended sources close to the GC. The objective of this analysis is to describe these emission regions by applying suitable models. This is done adding simple Gaussian spatial models or hydrogen templates.

The second part of this thesis focuses on the *Fermi* Bubbles template analysis. Therefore, mainly HESS Iu data are used. To check the consistency of the results achieved by the different H.E.S.S. eras, this analysis is repeated using HESS I and II data separately as well as combined data from all eras. The idea is to define a template around the region where *Fermi* Bubbles are expected from *Fermi*-LAT observations. All other physical γ-ray emitters (e.g. the CMZ) are masked from this analysis. Using the HAP 3D background model, the spectrum inside this *Fermi* Bubbles template is computed. An analysis where all sources in the full ROI are modelled for HESS Iu data (similar to the HESS I analysis of the full ROI carried out first) is performed as a cross-check of the HAP HESS Iu *Fermi* Bubbles template analysis.

[4] `https://www.mpi-hd.mpg.de/hfm/HESS/`

2. *Fermi* Bubbles in the γ-ray sky

As already mentioned, the origin of the *Fermi* Bubbles as well as the production mechanisms of the γ-rays could not be resolved to this day. The following section picks up the rough overview given in the introduction. In the first step, different scenarios leading to the γ-ray emission within the *Fermi* Bubbles will be explained in more detail, namely the hadronic and leptonic production mechanism. Furthermore, the two most popular models for the origin of the *Fermi* Bubbles are presented. It is supposed that the *Fermi* Bubbles are either originating from an active past of the SMBH Sgr A* in the GC or due to a starburst event near the GC. As the last step, the low latitude *Fermi* Bubbles are discussed in more detail because these are the object of interest in this thesis.

2.1. γ-ray production mechanisms

The γ-ray creation within the *Fermi* Bubbles can take place via leptonic or hadronic processes. In former case, ISRF photons are energetically up-scattered by high-energy electrons, while in the latter case photons result from interactions between hadronic CRs and the surrounding gas.

2.1.1. Leptonic model

In this scenario, the γ-rays are produced due to ICS of high energy electrons contained within the *Fermi* Bubbles and photons of the ISRF, mainly the CMB [16], but also starlight and infrared light due to dust. Hence, the photon energies increase up to the γ-ray range. It turns out that the γ-ray spectrum of the *Fermi* Bubbles can be well explained by a power law electron spectrum with an index of ~ -2.2 and an exponential cutoff at $\sim 1.25\,\mathrm{TeV}$. The emission because of Bremsstrahlung is negligibly small compared to the radiation produced by ICS. For galactic latitudes $|b| < 35°$, the microwave haze detected by WMAP and Planck [5] spatially overlaps with the *Fermi* Bubbles. The microwave emission decreases significantly above $|b| \sim 35°$ [16]. The vanishing intensity of the microwave haze at higher latitudes can be traced back to the decrease of the magnetic field with increasing height above the GP and the fact that the microwave haze is caused by synchrotron radiation. Nevertheless, microwave and γ-ray emission can be explained by the same population of electrons for magnetic field strengths in a range from $5\,\mu\mathrm{G}$ to $20\,\mu\mathrm{G}$. The best consistency is found for a magnetic field strength of $\sim 8.4\,\mu\mathrm{G}$. However, it cannot be ruled out that microwave and γ-ray emission are resulting from two distinct electron populations, because further investigations reveal that for the ICS signal mainly electrons at energies $> 100\,\mathrm{GeV}$ contribute, while the energies of the electrons causing the microwave emission are lower; in particular, in the range of few tens of GeV [9].
But there are also some discrepancies of this leptonic model. Electron energies of $\sim 2\,\mathrm{TeV}$ are necessary to produce GeV photons by IC scattering of the electrons and photons of the CMB. It can be shown (for example in [9]) that the cooling time for electrons of such energies would be roughly 1 Myr if just IC losses are considered. Assuming that the electrons have been produced within the GP and travel up to high latitudes (i.e. $\sim 10\,\mathrm{kpc}$ above the GP), their expansion velocity has to be larger than 10,000 km/s. This corresponds to a velocity much larger than the speed of sound in the region around the GP. Consequently, a shock front at the bubbles boundaries would be expected, that has not been discovered yet [17]. Nevertheless, ROSAT data reveal evidence for such shocks [13]. Additionally, Fox et al. published a paper in 2015 [18] where they kinetically modelled a biconical gas outflow expanding from the GC. They stated that the outflow velocity would be slightly above 900 km/s which is approximately one order of magnitude smaller than the required travelling speed of the electrons [18]. One suggestion to

[5] `https://www.esa.int/Enabling_Support/Operations/Planck`

address the latter issue would be a series of consecutive shocks - as a consequence of periodic injection of hot plasma - to obtain freshly accelerated electrons within the whole *Fermi* Bubbles. This approach has been suggested by Cheng et al. in 2011 [19]. Another possibility would be the re-acceleration of the electrons via the 2^{nd} order Fermi acceleration mechanism [13].

2.1.2. Hadronic model

In the hadronic scenario, hadronic CRs interact with the surrounding gas. As a consequence, further particles like the neutral pion π^0 are created. Latter one decays into two (γ-ray) photons following equation (1) given in chapter 1. In case of the hadronic model regarding the *Fermi* Bubbles, inelastic proton-proton collisions are the dominating energy-loss processes. Hence, the following argumentation is based on the assumption of proton CRs. The *Fermi* Bubbles spectrum in γ-rays can be not only described by an electron spectrum, but also by a proton CR spectrum. Again, the best fitting spectrum is a power law spectrum, in this case with an index of ~ -2.1 and an exponential cutoff at $\sim 14\,\mathrm{TeV}$ which turned out to describe the data better than a simple power law at high energies [9]. This proton spectrum deviates from the γ-ray *Fermi* Bubbles spectrum at energies of $\sim 100\,\mathrm{MeV}$ because of the pion cutoff. This discrepancy can be solved by keeping in mind that also leptons can be products of CR interactions with interstellar gas. The leptons themselves can lead to γ-ray emission via ICS. Adding up these additional emissions to the proton spectrum compensates the deviation from the γ-ray *Fermi* Bubbles spectrum [17], [9]. At high energies, the proton spectrum within the *Fermi* Bubbles has to be harder than the one of CR protons in the GP. The hard spectrum within the *Fermi* Bubbles is given evidence by the fact that the energy-loss time of proton-proton interactions is almost energy-independent and smaller than the particle's escape time. This effect does not hold within the GP where energy-dependent confinement effects occur, leading to a softer spectrum [20]. In other words, protons within the *Fermi* Bubbles have to interact before their escape, which requires them to stay within the bubble for a time span in the range of several Gyr. Protons within the GP, on the other hand, leave the plane before they interact there [9].
One problem of the hadronic emission model that cannot be easily resolved is that the ICS and synchrotron spectra of the secondary produced leptons do not fit the microwave haze spectra measured by WMAP and Planck [21]. Particularly, the WMAP and Planck emission intensities are a factor three to four larger than the spectra of the hadronic model's secondary leptons [9]. This issue does not depend on the magnetic field strength and thus cannot be corrected in this way. Moreover, the spectrum of the secondary leptons is significantly softer than the microwave haze spectrum [9]. Nevertheless, various approaches to encounter this problem have been suggested. One possibility would be that there is an additional population of primary electrons. Furthermore, a re-acceleration of the secondary leptons can be named here [9].
Putting all these pieces together, the hadronic emission model can also well describe the *Fermi* Bubbles γ-ray emission.

2.2. Origin of the *Fermi* Bubbles

Because of the spatial morphology of the *Fermi* Bubbles. i.e. their center close to longitude $l = 0^\circ$ and north-south symmetry, it is reasonable to assume that the *Fermi* Bubbles originate from the GC. However, it is not clear which process(es) - at or in close vicinity of the GC - exactly are responsible for the emission [21]. The two most popular models are on the one hand the activity of the SMBH in the GC and on the other hand a starburst close to the GC. Both are presented more detailed in the following two sub-chapters. One should keep in mind that various mechanisms should work together to explain all the observed features of the *Fermi* Bubbles [16]. Notwithstanding, not all combinations of the different models can describe the

Fermi Bubbles successfully and maintain the correct hard *Fermi* Bubbles spectrum [16], [21].

2.2.1. Active past of the SMBH

At the moment, the SMBH SGR A* in the GC is quiescent, particularly its radiation strength is roughly a factor of eight magnitudes below Eddington limit [8]. Nevertheless, SGR A* might have had an active AGN-like state in the past. Hence, it is possible that SGR A* emitted two jets that have inflated the *Fermi* Bubbles region, having the ability to accelerate CRs up to large energies. These jets can for example be results of a star accretion processes [8]. This approach is promising because it is episodic, i.e. it can explain the sharp edges of the *Fermi* Bubbles [16]. In addition, the jets can produce the amount of integrated radiation power in γ-ray and in microwave signal, respectively. This jet model typically assumes the leptonic γ-ray production process described in chapter 2.1.1.
Simulations by Guo et al. [22], [23] showed that a recent jet event emerging from SGR A* around 1 Myr ago can describe the spatial features - e.g. the elongation and ellipticity - of the *Fermi* Bubbles properly. Moreover, this particular model can explain the fact that the spectral index is roughly uniform within both bubble regions. It is based on extra-galactic AGN jets where CR-filled bubble-shaped radio emission has been observed [23], [24]. One of these observed radio galaxies is *Hercules A*. A multi-wavelength image of *Hercules A* is shown in figure 2.

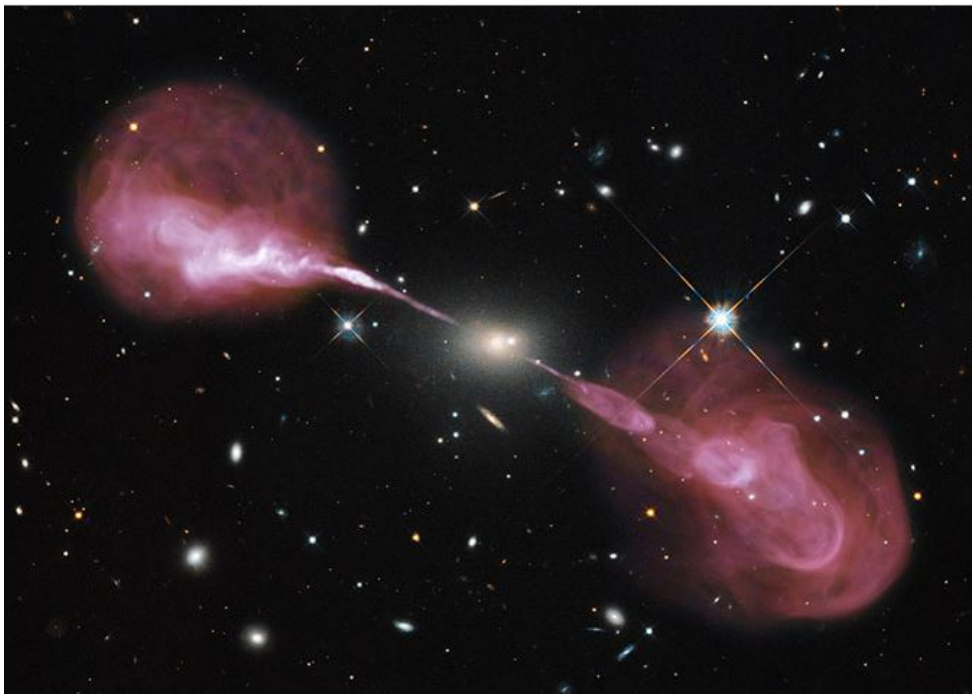

Figure 2: Multi-wavelength image of *Hercules A*. The image consists of data taken by the *Hubble Space Telescope* [6] and the *Very Large Array* radio telescope [7]. The two opposing jets are clearly visible as well as the bubble-shaped emission. Figure taken from [25].

However, there are also a few constraints on the leptonic jet models. The first one is that high accretion rates are required during the active phase of Sgr A*. Additionally, to explain the uniform *Fermi* Bubbles spectrum, very high outflow velocities are necessary. It is still an open question whether these high velocities are consistent with those derived from e.g. X-ray studies of the kinematic structures of the Galactic halo (GH) [21]. One further issue is that the radio

[6] `https://hubblesite.org/`
[7] `https://public.nrao.edu/telescopes/vla/`

lobes produced by jets in other galaxies extend to large distances. WMAP data of the *Fermi* Bubbles region, however, show that the microwave haze is confined to lower latitudes and no radio lobes coincident with the the γ-rays have been found [16].

2.2.2. Starforming region

The second common model assumes galactic winds driven by starbursts. These winds might be generated by high thermal as well as ram pressure. The initial wind can then entrain swept-up material. There are two common scenarios explaining the power supply of these winds: On the one hand, core-collapse *Supernovae* (SNe) provide thermally-driven winds; on the other hand, momentum-driven winds can be powered by starburst radiation [8], [26]. It is possible that the *Milky Way* has been in a starburst phase in the last ≈ 10 Myrs [8]. It has been observed that starburst galaxies also show bipolar outflows along the polar axis of the concerning galaxy [27]. The total energy of starburst galaxies - estimated as $\sim 10^{55} - 10^{56}$ erg - is in the same order of magnitude as the energy contained within the *Fermi* Bubbles [8], [16]. One famous example for a starburst galaxy is *M 82*. In 1996, Strickland et al. [28] reported a galactic wind for *M 82*. The X-ray emission associated to this wind extends ≈ 6 kpc above and below the center of this galaxy and has a bubble-shaped morphology. A multi-wavelength image of *M 82* is presented in figure 3. Additionally, a star-formation event within the inner 0.5 pc of the *Milky Way* approximately 6 Myr ago has been reported by Paumard et al. in 2006 [29]. The time-span of the star-formation is in accordance with the estimated age of the *Fermi* Bubbles.

Figure 3: Multi-wavelength image of *M 82*. The image consists of *XMM-Newton* [8] data. The observed X-rays correspond to the blueish bubble-shaped region. Optical and UV emission are shown via the yellowish coloured regions along the plane of the galaxy. Figure taken from [30].

A star formation scenario has been introduced by Crocker & Aharonian in 2011 [20]. They proposed that a galactic 'super wind' emerging from the nuclei of star-forming galaxies transports hadronic CRs outgoing from the GP. Problematically, this scenario requires that the CR protons

[8] `https://www.esa.int/Science_Exploration/Space_Science/XMM-Newton_overview`

are trapped within the *Fermi* Bubbles for multi Gyr.
An alternative model has been suggested by Zubovas et al. in 2011 [31]. They state that the *Fermi* Bubbles could be remnants of outflows from Sgr A* as a conseqence of a short accretion event onto Sgr A* that happened at the same time as the star-formation process confirmed by Paumard [29]. The mass accreted during this process is approximately the same as the mass of the stars created during the star-formation event, i.e. one half of the available gas has been converted into new stars and the other half has been accreted onto Sgr A*. Thus, the model by Zubovas et al. combines features of an active past of the SMBH Sgr A* and star-formation models. γ-rays in this model are produced by CR protons interacting with gas rather than electrons [31]. This is similar to the case presented by Crocker & Aharonian [20].

2.3. Low latitude *Fermi* Bubbles

As already mentioned in the introduction, the *Fermi* Bubbles at low latitudes (i.e. $|b| < 10°$) are brighter and have a harder spectrum than the bubbles at high latitudes [14]. Thus, it may be possible to detect the *Fermi* Bubbles with the H.E.S.S. telescope array above $\approx$ 100 GeV where *Fermi*-LAT has low statistics.
However, there are some challenges in the analysis of the *Fermi* Bubbles at low latitudes. Within the ROI observed during this thesis ($|b| < 5°$, $|l| < 10°$), there is a large amount of γ-ray emission with different origin. First, there are astrophysical sources like *Pulsar Wind Nebulae* (PWNe) or *Supernova Remnants* (SNRs). Further emission originates from the CMZ in close vicinity of the GC. Additionally, there is a contribution from Galactic and extragalactic γ-ray radiation. During the analysis, these regions of γ-ray emission have been either masked or modelled for a proper description of the selected ROI.
The surface brightness map for low latitude *Fermi* Bubbles is shown in figure 4 b). For this particular region corresponding to the ROI used in this thesis, the map reveals an east-west anisotropy of the *Fermi* Bubbles at negative latitudes with respect to the GC. Particularly, for negative longitudes, the emission is much brighter than for positive longitudes. The maps presented in figure 4 are extracted from *Fermi*-LAT observations published by Ackermann et al. in 2017 [14]. In figure 4 a), the full *Fermi* Bubbles template is shown. A further feature that can be seen by looking at this full map is the so-called cocoon in the southern bubble (i.e. at negative latitudes). It extends extends from $\approx 0°$ to $\approx -40°$ in galactic latitude on the east side (i.e. positive longitudes) of the southern bubble and has been first observed by Su & Finkbeiner in 2012 [32].
Furthermore, a threshold of 8.5 sr-1 has been chosen to define a *Fermi* Bubbles on-region [33] for the H.E.S.S. analysis. This region is indicated via the black contour in figure 4 b). The solid angle of this *Fermi* Bubbles on-region is $\Delta\Omega_{FB,\,Fermi-LAT} = 1.9 \cdot 10^{-3}$ sr.

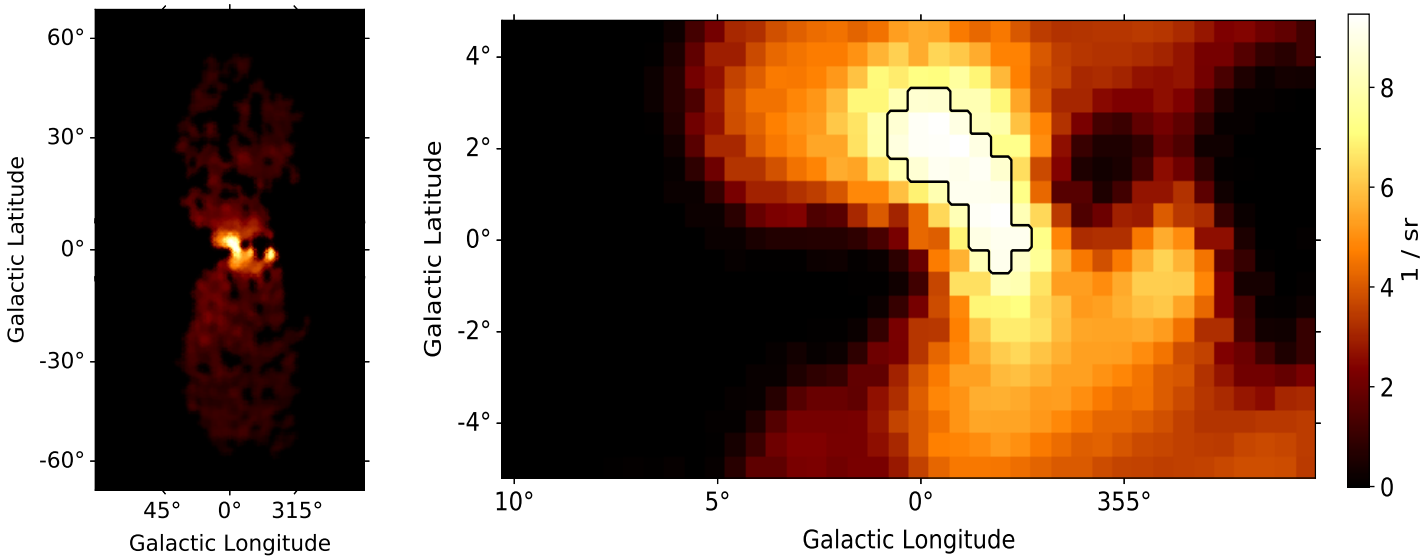

(a) Full *Fermi* Bubbles template

(b) *Fermi* Bubbles template within the ROI investigated in this thesis

Figure 4: *Fermi* Bubbles template derived from *Fermi*-LAT data [14]. (a) Full *Fermi* Bubbles template. It shows that the *Fermi* Bubbles at low latitudes are brighter than at higher latitudes. (b) represents the same template, but in the ROI that hes been investigated in this thesis. At zero latitudes, the bubble is clearly brighter at negative compared to positive longitudes. Note that both plots share the same colorbar. The black contour indicates the *Fermi*-LAT *Fermi* Bubbles template with $\Delta\Omega_{FB,\,Fermi-LAT} = 1.9 \cdot 10^{-3}$ sr.

3. Imaging Atmospheric Cherenkov Telescopes and H.E.S.S.

Since data that have been analysed during this thesis were taken by H.E.S.S., the next chapter is devoted to it. The first two sub-chapters treat the physical mechanisms of particle showers and Cherenkov radiation. These principles are necessary to understand how the detection of γ-rays via IACTs works. The following part gives a rough overview of the general structure of an IACT. The last part of this chapter contains information on H.E.S.S. and the procedure of data taking.

3.1. Evolution of particle showers

Earth's atmosphere is opaque for CRs, i.e. when entering the atmosphere, particle interactions take place, leading to the production of secondary particles that can then again produce further particles. In this way, cascades of secondary particles - the particle showers - evolve. One distinguishes two kinds of showers. The electromagnetic showers are induced by either a lepton or a photon entering the atmosphere. The second kind of showers are the hadronic showers which are created by protons or nuclei entering atmosphere [34].
Due to the different particles involved, hadronic and electromagnetic showers differ regarding their morphology and the amount of produced secondary particles. For example, the lateral extension of hadronic showers is larger than in case of electromagnetic showers because of the large transverse momentum transfer during hadronic interactions [35]. Additionally, within a hadron-induced cascade several sub-showers can appear which are again extended, for example due to π^0 decay [36].
However, electromagnetic showers are the objects of interest when γ-rays have to be detected. Hence, electromagnetic showers are discussed in the first part of this chapter in detail. Information on hadronic showers will also be given, even though kept qualitatively.

3.1.1. Electromagnetic showers

The two main interaction processes taking place when leptons (mostly e^- and e^+) and γ-rays hit the atmosphere are Bremsstrahlung and pair production. In case of the pair-production process, an incoming γ-ray photon can produce an $e^-\,e^+$ pair according to

$$\gamma + N \rightarrow e^- + e^+ + N. \tag{2}$$

Note that this process is only possible because Earth's atmosphere contains - among others - atomic nuclei ensuring momentum conservation [4, p.19]. The interaction in above equation does not take place with the nucleus N itself, but with the electric field (virtual photons) produced by the nucleus.
For high-energetic electrons and positrons, the dominating energy-loss process is Bremsstrahlung [15, p.92]. During this process, the charged particles emit photons in the presence of the electric field of a nucleus. Formally, this process can be written down as

$$e^- + N \rightarrow e^- + \gamma + N. \tag{3}$$

It is possible that the photons that are created during the process of Bremsstrahlung are energetic enough to again undergo pair-production (according to equation (2)). In this way, further $e^-\,e^+$ pairs are produced and can generate further photons via Bremsstrahlung. Since the energy-threshold for pair-production is $\sim 1\,\mathrm{MeV}$ (two times the electron mass at rest, [37, p.57]) and incoming γ-ray photons have energies in the GeV-range and higher, such reaction chains can be repeated multiple times. i.e. a particle shower evolves. The created shower then contains a

large amount of charged particles that can lead to Cherenkov radiation (see next chapter 3.2). The scheme of an evolving electromagnetic shower is shown in figure 5.

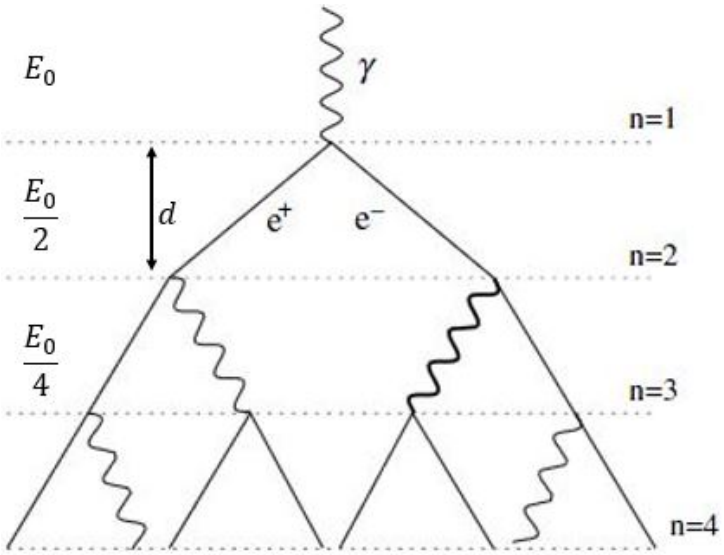

Figure 5: Scheme of an evolving electromagnetic shower following the model by Heitler. Figure adapted from [34].

In this scheme, an extraterrestrial photon with initial energy E_0 hits Earth's atmosphere and induces an electromagnetic shower. Following Heitler [38, p.386 ff.], [34], after one splitting length d the photon splits into an $e^- e^+$ pair. The same length d is also assumed to be the travelled distance at the end of which an electron or positron radiates a single photon due to Bremsstrahlung. More formally, d is defined as the length over which an electron or positron loses half its energy by radiation on average [34]. One of the assumptions of the model by Heitler is, in fact, that in each interaction process, the energy is equally shared by the reaction products. Thus, both, the electron and the positron produced in the first step would have the same energy, i.e. $\frac{E_0}{2}$. The number of particles is doubled after each splitting length. After n splitting lengths the total particle number N is given as

$$N = 2^n \tag{4}$$

including electrons as well as positrons and photons.
It is only possible for the shower to evolve in this way as long as Bremsstrahlung and pair-production are the dominating energy-loss processes. Therefore, a critical energy E_c can be defined. Below this energy, radiation via Bremsstrahlung is highly suppressed, i.e. electrons and positrons lose their energy predominately via ionisation. E_c lies in the range of few 10's of MeV [4, p.20], [37, p.37]. Pair production is the dominating energy-loss process for photons above $\sim 1\,\mathrm{MeV}$. Below this threshold, Compton scattering becomes dominant [4, p.18]. The maximum number N_{max} of shower particles can be consequently estimated as

$$N_{max} = \frac{E_0}{E_c}. \tag{5}$$

Comparing the equations (4) and (5), one finds the energy of the initial photon to be

$$E_0 = E_c\, 2^{n_c} \tag{6}$$

where n_c is the critical number of splitting lengths which can be expressed by

$$n_c = \log_2\left(\frac{E_0}{E_c}\right). \tag{7}$$

Above formulae have been taken from [38, p.386 ff.]. The lateral extend of a shower can be described by the Moliere radius

$$R_M = 21\,\mathrm{MeV}\,\frac{d}{E_c}. \tag{8}$$

More than 90 % of the shower is contained within a distance of about $2\,R_M$ from the longitudinal axis [37, p.61].
As a last remark, it should be mentioned that the model by Heitler is a drastic simplification of the evolution of an electromagnetic shower and just describes an average behaviour of the shower. Even though real showers show large fluctuations mostly because of Bremsstrahlung [37, p.60], simulations confirm that the maximum size of the shower is proportional to E_0 as found in equation (5) and that the maximum depth of the shower, i.e. the maximal number of splitting lengths, increases logarithmically with energy as derived in equation (7). Nevertheless, simulations reveal that the number of particles created in showers can have large deviations from Heitler's predictions [34].

3.1.2. Hadronic showers

The evolution of hadronic showers is dominated by processes of the strong interaction. These showers can contain different sub-showers making them laterally more spread and complicated than electromagnetic showers. When a hadron hits the atmosphere and undergoes inelastic scattering processes with the present nuclei, pions (π^0, $\pi^\pm$) as the lightest mesons are the favoured outcomes. As already mentioned, the neutral pions π^0 immediately decay into two photons [4, p.21]. Since these photons can undergo pair-production, an electromagnetic cascade as described in the previous sub-chapter 3.1.1 evolves. This is shown in the left column of figure 6. The charged pions $\pi^\pm$, however, can interact via strong interaction above a certain critical energy. Below this energy, they decay as

$$\begin{aligned} \pi^+ &\rightarrow \mu^+ + \nu_\mu \\ \pi^- &\rightarrow \mu^- + \overline{\nu_\mu} \end{aligned} \tag{9}$$

via the weak interaction. This sub-shower is then referred to as the muonic component shown in the central column of figure 6. Furthermore, the produced muons $\mu^\pm$ can again lead to electromagnetic cascades, since the decay into electrons and positrons follows

$$\begin{aligned} \mu^+ &\rightarrow e^+ + \overline{\nu_\mu} + \nu_e \\ \mu^- &\rightarrow e^- + \nu_\mu + \overline{\nu_e}. \end{aligned} \tag{10}$$

The hadronic component (right column in figure 6) originates from neutrons and protons resulting from disintegration of an atmospheric atom by a primary particle [39]. The decay channels listed above have been taken from the *Particle Physics Booklet* which is an extraction from [40]. In the performed analysis, the signal of interest is caused by electromagnetic showers induced by γ-rays hitting Earth's atmosphere. Hadronic showers also lead to a signal that is detected by the telescopes. Hence, it is required to filter out these background events that are originating from hadrons penetrating the atmosphere.

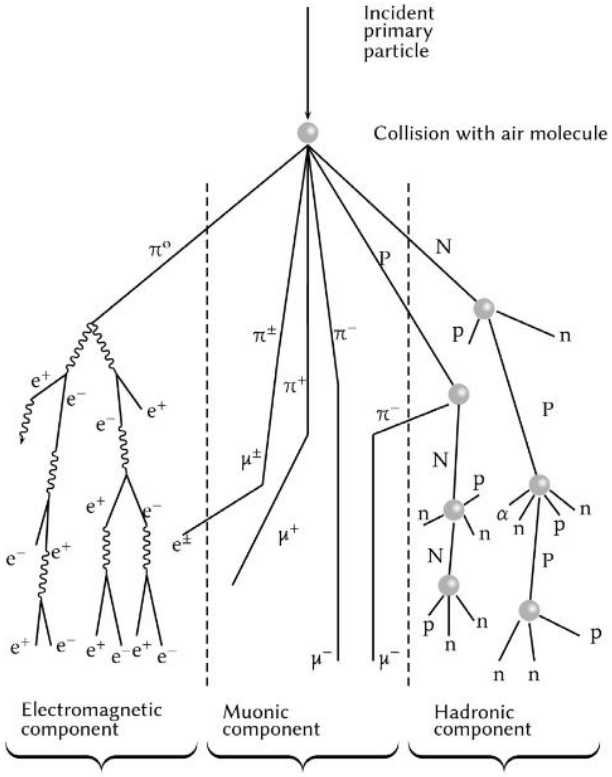

Figure 6: Scheme of an evolving hadronic shower. Three different sub-showers can be created: electromagnetic, muonic and hadronic component. Figure taken from [39].

3.2. Cherenkov radiation

Charged particles moving in a certain medium polarise the surrounding molecules. After the particle has passed, the molecules return to their unpolarised state via emission of photons. Only if the speed v of the charged particle is larger than the phase velocity of light in the corresponding medium with refractive index n, i.e.

$$v > \frac{c}{n}, \tag{11}$$

constructive interference occurs. Here, c denotes the speed of light in vacuum. However, due to the constructive interference, photons are emitted as a coherent wavefront at a fixed angle θ to the trajectory of the charged particle. This is known as Cherenkov radiation. Having a look at figure 7, the opening angle of the cone-shaped wavefront can be determined as

$$\cos(\theta) = \frac{1}{n\,\beta}, \tag{12}$$

where $\beta = \frac{v}{c}$ is the ratio of the charged particle's speed v and the speed of light in vacuum c. Above given information on the Cherenkov radiation have been taken from [4, p.17] and [41]. For high-energetic particles (i.e. $\beta \approx 1$) in air ($n \approx 1$), one finds $\theta \approx 1°$. Consequently, the radius of the cone of the Cherenkov radiation is roughly 125 m at Earth's surface, assuming that the shower originated in a height up to 15 km above the ground and the particle is vertically moving downwards [35].
According to [37, p.36], the number of produced photons dN over the particle's travelling distance dx and unit wavelength $d\lambda$ can be calculated as

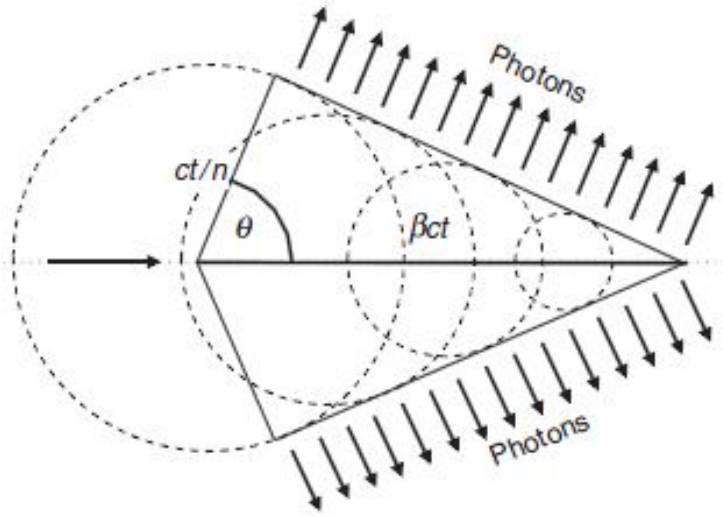

Figure 7: Emergence of the Cherenkov radiation. Figure taken from [4, p.17].

$$\frac{d^2N}{dx\,d\lambda} = \frac{2\pi\alpha z^2}{\lambda^2}\sin^2(\theta). \tag{13}$$

In the above equation, α defines the dimensionless fine structure constant ($\approx \frac{1}{137}$) and z the charge number of the particle leading to emission of Cherenkov radiation. It can be seen by taking a look at equation (13) that more particles are produced with decreasing wavelength, i.e. higher energy. Since the most energetic region of the visible light spectrum is the blue-violet one, Cherenkov lights appears blue. This can be for instance observed at nuclear reactors.

3.3. General structure of IACTs

Elementary, an IACT consists of two main components. The first one is not a mechanical device, but simply Earth's atmosphere where the incoming γ-rays initiate particle showers as discussed in chapter 3.1.1. In particular, the atmosphere works as a calorimeter. The Cherenkov radiation - explained in the previous chapter 3.2 - of secondary products of these showers can be detected by the IACT's second main component, namely the telescope itself.
The telescope's objective is to catch the Cherenkov light that often has low intensities. Therefore, the telescope has nearly spherical mirrors covering large areas. These mirrors reflect the Cherenkov light onto a camera aperture - the Cherenkov camera - that is mounted centrally in front of the mirror dish. This camera consists of an array of photo detectors, either *Photo Multiplier Tubes* (PMTs) or *silicon photomultipliers* (SiPMs). For visualisation, the largest telescope of the H.E.S.S. telescope array is presented in figure 8. When photons are hitting the detectors, a signal is induced that can be evaluated via an appropriate electrical circuitry. It is furthermore important that the photo detectors have a short response time to distinguish the signal of interest - lasting $\approx 2\,\text{ns}$ - from the background [6].

3.4. Detection principle

The propagation of Cherenkov light proceeds as perspectively shown in figure 9. The photons reflected by the mirror hence induce an elliptically shaped pattern on the Cherenkov camera because the shower axis and the telescope axis are in general not in alignment. Such elliptical patterns are shown in figure 10. On the left hand side of this figure a γ-ray induced, narrow

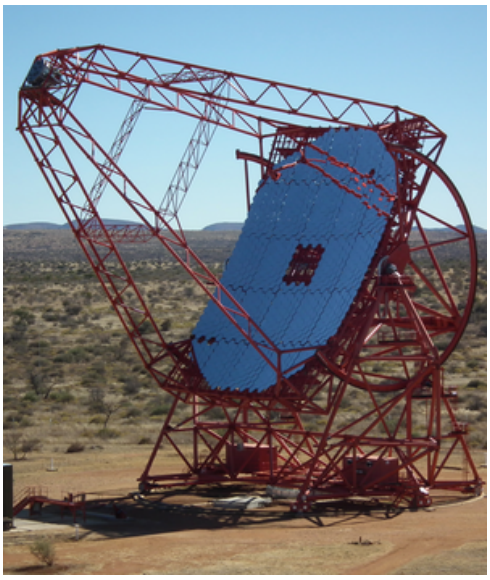

Figure 8: Telescope CT 5 of the H.E.S.S. Telescope Array in Namibia. The diameter of the mirror dish amounts 28 m. In the top left corner of the image, the Cherenkov camera in front of the mirror can be seen. The camera of this telescope has a weight of 2.8 tons and consists of PMTs. At the moment, CT 5 is the largest operating Cherenkov telescope in the world [6], [42].

elliptical shower pattern is shown. Compared to the γ-shower, the proton induced shower pattern on the right hand side of the figure is more spread and extended as discussed in chapter 3.1.
One of the most difficult tasks when operating an IACT is to reduce the background signal, i.e. the recorded signal originating from hadronic showers. It is possible to distinguish γ-ray and hadron induced showers in a more quantitative way to separate the interesting γ-ray signal from the hadronic signal. A.M. Hillas suggested in 1985 [43] to use a geometric technique based on the width, length and orientation of the Cherenkov light-induced camera patterns for event separation and reconstruction of the initial γ-rays. Since this approach is very descriptive and algorithms based on Hillas parameters are still in usage, it is further described in the following lines. Hillas has simulated the shower development using Monte-Carlo simulations; a new tool back in time [43]. The schematic procedure is presented in figure 11.
In a first step, the image major axis and the center of gravity can be determined. The root mean square (RMS) of light directed parallel and perpendicular with respect to the major axis are then referred to as length L and width W [43]. These two parameters are mainly used to discriminate hadron-induced events from γ-ray-induced ones because of the larger width of the hadron-induced patterns. Additionally, the total size of the pattern can be determined via the total charge of photo-electrons in the image [36].
The further parameters are:

- d: Angular distance between center of gravity of the pattern and center of the camera
- ϕ: Azimuthal angle of the image's main axis
- α: Orientation angle

Using all of these parameters provides an enhanced background suppression and also allows for an improved reconstruction of the position of the initial γ-ray [36].
This can be realised taking not only one Cherenkov telescope into account, but multiple telescopes at the same time. This procedure is called stereo-mode and illustrated in figure 12. In

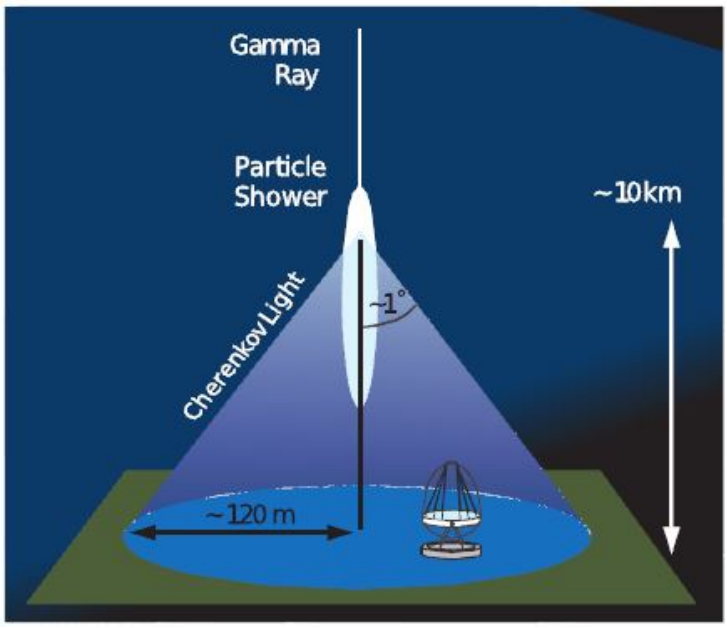

Figure 9: Emergence of a Cherenkov cone caused by a particle shower. Figure taken from [36].

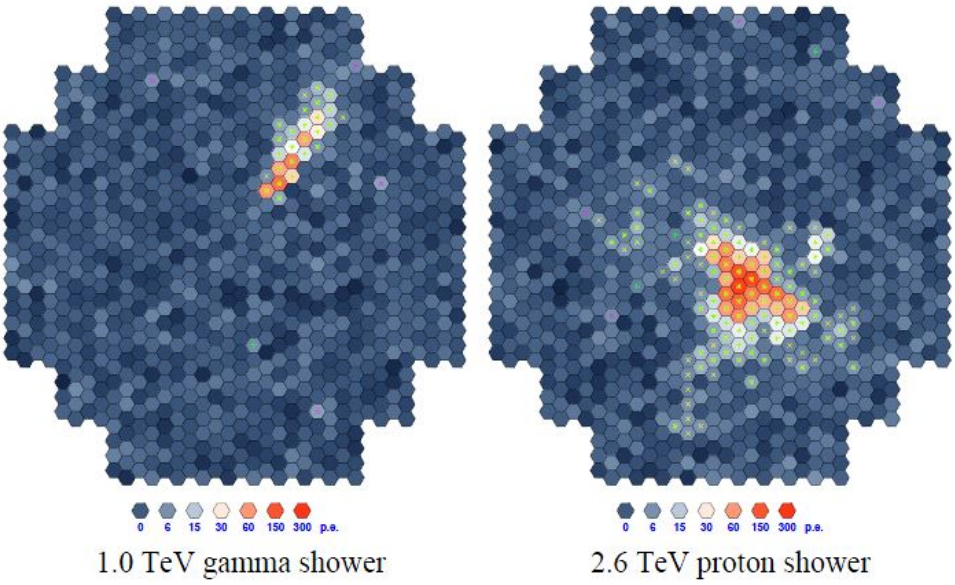

Figure 10: Resulting photon patterns caught by the Cherenkov camera of an IACT for a γ-ray (left) and a proton (right) induced event. Figure taken from [35].

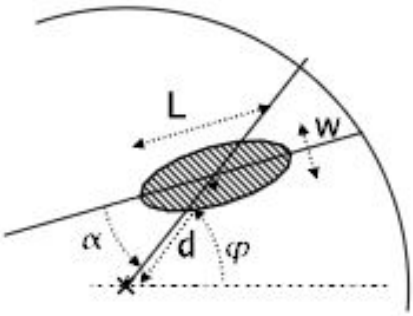

Figure 11: Geometrical properties of a signal pattern. Figure taken from [36].

this case, different neighbouring telescopes observe the same event, but all from a different point of view. Hence, the observed patterns differ. This is illustrated in figure 12 b). When all the different patterns are then projected to one common area (see figure 12 c)), the point where the main axes of all individual showers intersect each other is the impact position of the originating particle [36].
Note that there exist further approaches leading to improved results regarding the pattern reconstruction like the *Image Pixel-wise fit for Atmospheric Cherenkov Telescopes* (ImPACT) algorithm by Parsons & Hinton [44]. ImPACT is based on a set of simulated shower patterns that can be seen by the telescope. In a next step, a Likelihood fit of the measured pattern to the simulated template is performed. This allows for an improved shower reconstruction compared to algorithms based on the Hillas parameters, especially at low energies. For example, in case of points sources, the sensitivity can be improved by roughly a factor of 2 [44]. Nevertheless, the separation of γ-ray and hadron induced events does not work significantly better than in case of using Hillas parameters. In the course of this thesis, two different background reconstruction chains are used. On the one hand, the Hillas parameters based zeta configuration, on the other hand the ImPACT algorithm.

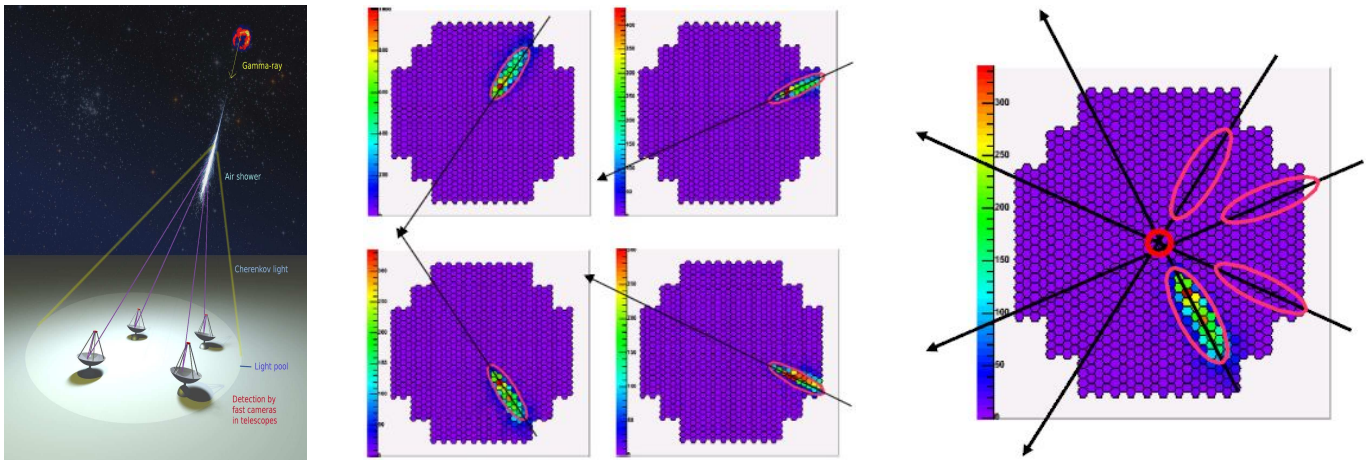

(a) Illustration of the stereo-mode, from [35]

(b) Shower patterns seen by the different telescopes, from [36]

(c) Combined shower pattern, from [36]

Figure 12: Visualisation of the stereo-mode

3.5. H.E.S.S.

In this chapter, information on the H.E.S.S. location, the arrangement of the telescopes and the properties of the telescopes are given in the first part. The second part deals with the observational runs performed by H.E.S.S..

3.5.1. Experimental setup

The information presented in this chapter are extracted from [6] if not stated differently. The H.E.S.S. telescope array is an array consisting of five Cherenkov telescopes in total and is named after Viktor F. Hess who has already been introduced in chapter 1. It is located in the Khomas Highland of Namibia, about 100 km south-west of Windhoek. The arrangement is shown in figure 13. The four outer 12 m telescopes were built in 2002 and 2003. They are arranged in a square of 120 m side length. Note that the radius of the Cherenkov light cone at Earth's surface is $\approx$ 125 m (see chapter 3.2) such that it is possible that all telescopes are illuminated

simultaneously. These outer telescopes are named CT1 to CT4 and represent the first era of H.E.S.S. observations, called HESS I.
However, their hexagonal-shaped mirrors consist of 382 round mirror facets measuring a diameter of 60 cm each and a focal length of 15 m. Each of the HESS I telescopes covers a mirror area of 108 m^2. The cameras have a *field of view* (FoV) of 5° and consist of 960 pixels, i.e. PMTs, each. HESS I is capable of covering an energy range from ~ 0.1 TeV up to ~ 100 TeV.
The large telescope in the center of the four 12 m telescopes, CT5, has been added in 2012 and has a mirror dish corresponding to a 28 m circular area, equivalent to a total area of 614 m^2. Its focal length is 36 m and the single segments of the mirror consist of 875 hexagonal-shaped facets of 90 cm diameter. 2048 PMTs represent the camera of CT5, the FoV covers 3.2°. CT5 has been built to improve sensitivity of the H.E.S.S. array and to observe lower energetic events. Since the intensity of the Cherenkov light decreases with decreasing energy, a larger detector area is required to go to lower energies. However, the era where the 4 unmodified 12 m telescopes worked together with CT5 was called HESS II and started when CT5 has been inaugurated in 2012 and ended in 2016.
The cameras of CT1 to CT4 have been interchanged in 2015 and 2016. This upgrade has been necessary on the one hand, because their physical condition degraded over time and the electronics did not correspond to the state of the art anymore. On the other hand, CT1 to CT4 can only work reasonably together with CT5 when all the five cameras have the same properties like response time. Using this configuration, the detection of γ-ray down to energies of ~ 0.03 TeV is possible [42].
After having upgraded the cameras of the HESS I telescopes, the currently active era of data taking, HESS Iu, started.

Figure 13: The H.E.S.S. telescope array in Namibia. The four 12 m telescopes are quadratically arranged and surround CT5. Figure taken from [42].

3.5.2. Observational runs

One observational run of H.E.S.S. usually lasts 28 min and is performed via pointing with a small offset (1.5° in maximum) regarding the desired target. This allows for a check-up of the background and an estimation of the background level, since also parts of the FoV that do not contain the source are observed [45]. To accept an event detection, a three-level trigger concept is usually used: First, a signal above a certain threshold has to be detected at one single pixel. The next condition is that a certain number of pixels in the vicinity fulfils the same trigger condition as the first pixel within a pre-defined time-span. If multiple IACTs are used, in general at least

two telescopes have to be triggered coincidentally [36].
During the observations, the quality of the runs is checked simultaneously. Possible reasons for the rejection of a certain run could be that the trigger rate drops under a certain threshold (e.g. due to states of Earth's atmosphere that are unsuitable for data taking) or malfunctions of the telescope system [45].

4. Data analysis in a nutshell

In the following section, the theoretical basics of the data analysis are explained. The first part of this section briefly introduces the *HESS Analysis Package* (HAP) used for the low-level data analysis. Afterwards, the Gammapy [9] package suitable for the high-level analysis is presented in more detail. Particularly, the general workflow such as important and handy features are shown. The process of fitting models to the data is explained. In a last step, the *test statistic* which is an important measure of how well the applied models describe the data is described.

4.1. Introducing HAP

The H.E.S.S.-internal software HAP can be understood as the very initial step of evaluating data taken by an IACT. When operating IACTs, it is crucial to properly calibrate and model physical and instrumental effects. The first part of the simulations of the IACT technique consists of the simulation of the development of extended air showers and Cherenkov light emission. In HAP, the CORSIKA [10] algorithm is dedicated to this requirement. Modelling the detector response is implemented in `simtelarray` and marks the second necessary simulation for treatment of IACT data [46], [47]. Additionally, the γ-hadron separation as well as energy-reconstruction of initial γ-rays are performed via algorithms based on either Hillas parameters (zeta) or ImPACT (see chapter 3.4). Furthermore, a correction for the muon coefficient can be carried out.

4.2. Introducing Gammapy

The open-source Python package Gammapy has been developed to evaluate γ-ray data, mainly from IACTs already existing (e.g. H.E.S.S.) or planned in future (*Cherenkov telescope array* (CTA) [11]). Gammapy is built on the Python packages Numpy, Scipy and Astropy. For the data analysis performed during this thesis, versions v0.18.2 and v0.19 of the Gammapy package are used.

4.2.1. Data handling

Initially, the γ-ray data are stored as lists of γ-like events (together with their reconstructed properties) and the corresponding *instrument response functions* (IRFs) both of which have been determined via the HAP analysis chain. Latter ones are detector models that are needed to map the incoming photon flux to detected events [48]. The IRFs are built on the telescope's effective area, point spread function (PSF), energy dispersion and residual hadronic background [49]. Furthermore, information on the data taking run are provided, for example observation time and conditions such as the pointing direction of the telescope.

4.2.2. Datasets

In the course of this thesis, a three dimensional (3D) analysis - that is featured by Gammapy - of the data is performed. In this context, 3D means that the data taken during observations are investigated regarding their spatial and spectral properties at the same time. Hence, one of the three axes is the spectral axis, i.e. the energy axis. The other two axes span a two dimensional spatial coordinate system. During this thesis, the galactic frame has been used for the spatial axes, in particular the x-axis corresponds to the galactic longitude, while the y-axis represents the galactic latitude. It is now possible to configure an own geometry for the following analysis,

[9] `https://gammapy.org/`
[10] `https://www.iap.kit.edu/corsika/index.php`
[11] `https://www.cta-observatory.org/`

i.e. the size of the pixels in the spatial plane such as the energy bins along the spectral axis. The stored data - γ-ray data as well as the IRFs - are consequently mapped onto the chosen geometry. The resulting structure is then referred to as dataset. Gammapy provides the class `MapDataset` to store and deal with datasets. The interesting data of datasets are stored as maps. Besides γ-ray counts maps and background counts maps, the predicted γ-ray (i.e. model) counts as well as the modelled background counts can be inspected. The modelled counts and background counts maps depend on the chosen models. Additionally, the exposure can be extracted from the data.
At this point, it should be mentioned that the geometry of γ-ray event counts maps and exposure maps differs regarding the energy axis. While the energy axis of the exposure map gives the *true energy* (i.e. the energy of the initial photon inducing a particle shower), the count maps contain information on the *reconstructed energy* (the calculated energy of the initial photon). Both energies are spatially connected via the PSF and spectrally via the energy dispersion. These functions can be determined using Monte-Carlo simulations of air-showers. Furthermore, a distinct energy binning for *true energy* and *reconstructed energy* can in principal be chosen; during this thesis, the binning for both axes is selected to be identical [49].
Further, a command allowing for `stacking` of several datasets (for example, datasets of different observations can be stacked within a selected ROI) is implemented in Gammapy. Stacking, in particular, means that event and background counts maps as well as exposure maps are summed up within the data range. The combined PSF and energy dispersion are determined via an exposure weighted average [49].
A further option that comes in handy, is the method to `fake` a `MapDataset`. This means that data counts are simulated following a Poisson-distribution taking into account the assigned models and reduced IRFs. It thus allows for a comparison between the real and simulated data and makes it possible to e.g. estimate the significance of observed emission in a region.
The last important feature of `MapDatasets` is the option to mask certain pixels. Two different types of masks exist: On the one hand, there is the so called `mask_safe`. This mask is computed during the data reduction process (i.e. from the raw data to the desired datasets) according to the specified selection cuts. This mask can be for example set by defining a maximum offset from the pointing direction of an observation. Hence, it is usually not changed manually. On the other hand, a `mask_fit` can be additionally applied to a dataset to exclude desired regions from the fitting procedure. Usually, one initialises the `mask_fit` by simply copying the properties of the `mask_safe`. In a next step, additional pixels that are not excluded by the `mask_safe` and that should not be taken into account during fitting (e.g. known astrophysical sources which are emitting a vast amount of emission) can be masked [49].

4.3. Models

Additionally, models to describe the γ-ray emission can be added to `MapDatasets`. There exist different models that have already been implemented in Gammapy. For the analysis performed in this thesis, two different kinds of models are relevant. The first one is the 3D background model implemented in HAP to take CR emission into account. All the other models are built based on the class `SkyModel` requiring a spatial and a spectral model.

4.3.1. HAP 3D Background model

An additional background model for the hadronic γ-ray background is required, since the γ-hadron separation (see chapter 3.4 where Hillas parameters and ImPACT have been introduced) cannot sort out all the hadronic events. In this thesis, the HAP 3D background model is used, since it turned out to properly describe the background in regions where large-scale diffuse γ-

ray emission exists what is definitely true for the observed ROI. Therefore, Gammapy provides a class, called `FoVBackgroundModel` that can be assigned to a `MapDataset`. Especially, for stacked datasets, it is recommended to use this way of background modelling [49]. The idea of this background model is briefly presented following the description by Mohrmann et al. [50].
The 3D background model is based on archival H.E.S.S. observations. Background models for all three H.E.S.S. eras are available. 3D again means that the expected background rate is binned in terms of FoV coordinates as well as energy. To avoid that the data used to build the background model are contaminated with diffuse γ-ray emission, observations close to the GP (in particular $|b| < 5°$) have been excluded. Runs where the atmospheric conditions were unsuitable or malfunction of the hardware has been found were excluded, too. Additionally, the background rate depends on the telescope's pointing direction, especially a strong dependence on the altitude angle θ can be observed. Thus, the background model is binned into seven different bins regarding this parameter ranging from 30° to 90° [51]. Since the dependence on the azimuth is not that strong, however, two bins are sufficient for a proper description. These bins are given by $-90° < \phi < 90°$ and $90° < \phi < 270°$, respectively, where ϕ denotes the azimuth angle. For an appropriate description, further parameters like the actual state of the atmosphere during an observation or the fact that the telescope's efficiency decreases with time, can be taken into account. Since the efficiency also changes with the different eras (see chapter 3.5), it is furthermore important to use a background model based on the data of the same era as the analysed one.
In the following lines, the creation process of the 3D background model is illustrated using figure 14 as example. The data shown in this figure correspond to a certain energy bin as well as some specific bins for zenith and azimuth angle.

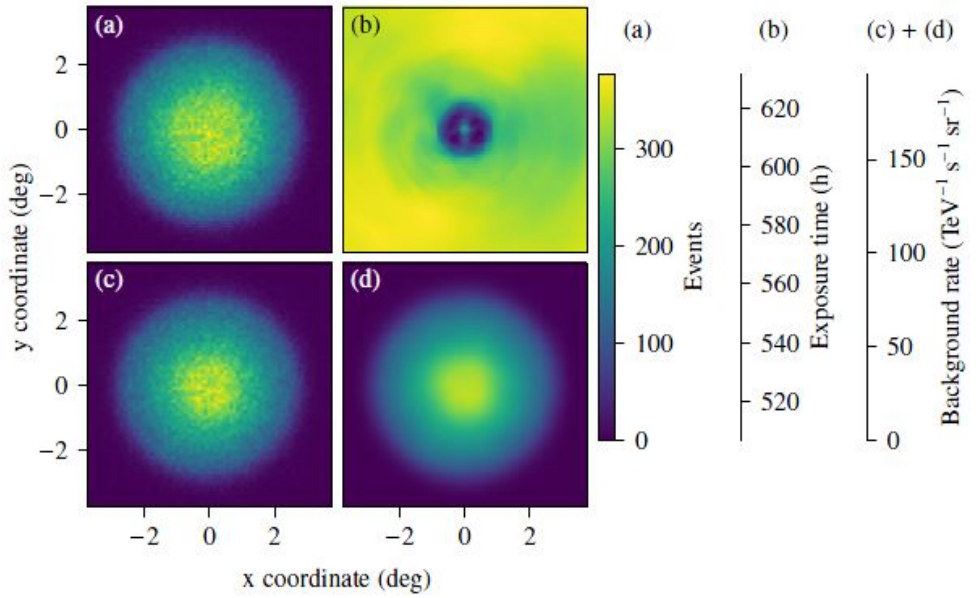

Figure 14: Implementation procedure of the 3D background model. Chosen binning: Azimuth angle $90° < \phi < 270°$, zenith angle $20° < \theta < 30°$, $0.8\,\text{TeV} < E < 1.1\,\text{TeV}$. a) Summed events per observation excluding known γ-ray sources, b) Exposure summed up over all observations, c) Averaged background rate, d) Smoothed average background rate. Note that the angle θ in this figure is defined as zenith angle (according to [50]) while it has been introduced as altitude angle in the text. Figure taken from [50].

Panel a) of this figure presents the sum over all events of an observation within the selected

region where known γ-ray sources as well as the region close to the GP have been masked. Panel b) shows the exposure time summed up over all observations. The pattern in figure 14 c) is the averaged background rate obtained by dividing the counts from panel a) by exposure from b), energy interval and solid angle. In a last step, the background rate is slightly smoothed to remove statistical fluctuations. This is shown in panel d).
In a next step, the normalisation for each observation is corrected by a Likelihood fit (see chapter 4.4 for details). Inspecting the fit results of the normalisation parameter plotted against the zenith angle θ, one realises that the resulting profile shows jumps at the boundaries of neighbouring zenith angle bins. Thus, a linear interpolation over all zenith angle bins is performed to eliminate the dependence on the zenith angle.
Nevertheless, there are further corrections of the model to be performed. One example therefore is that the fitted background normalisation depends on the optical transparency of the atmosphere. This issue can be solved by interpolation using a linear function. A further problem is the varying optical efficiency of the telescope itself leading to a slight bias in the background normalisation. It is also possible to correct the model regarding this aspect using an averaged fitted normalisation as correction factor for certain phases of different optical telescope efficiency. However, putting all the pieces together, the background rate R' can be estimated via

$$R' = R \cdot \left(\frac{E}{E_0}\right)^{-\delta}. \tag{14}$$

Here, R denotes the predicted background rate, E is the energy and E_0 the reference energy, usually fixed to $E_0 = 1\,\mathrm{TeV}$. The free parameters of the model are the normalisation and the tilt δ modifying the predicted background rate R at energy E. This kind of spectral model is referred to as *PowerLawNormSpectral* model, since the parameters are normalised and not absolute values.

4.3.2. SkyModels

To describe both the astrophysical sources within the ROI and regions with diffuse emission (for example the CMZ), the class `SkyModel` implemented in Gammapy can be used. The `SkyModels` used in the course of this thesis consist of one spatial and one spectral model each. The spatial model describes the morphology of the source or emission region, i.e. the flux $\Phi(\mathrm{lon}, \mathrm{lat})$ as function of its position in space and its extension. The spectral component calculates the flux $\Phi(E)$ of a source in dependence on the energy E and the spectral parameters. However, there exists a large amount of models that is already implemented in Gammapy. Additionally, specific models that are conform with the request of the user can be created. In the first part of this chapter, the spectral models and afterwards the spatial models are discussed. Note that the definitions of the models (including nomenclature of the various parameters) have been chosen in accordance to the Gammapy documentation [49].

4.3.2.1. Spectral models

Two kinds of spectral models are relevant in the analysis in this thesis. The first of these in-built models is the simple power law spectral model. Therefore, the returned flux is given by

$$\Phi(E) = \Phi_0 \cdot \left(\frac{E}{E_0}\right)^{-\Gamma}. \tag{15}$$

In above equation, Φ_0 is the amplitude given in flux units, namely TeV cm-2 s-1. Γ is the dimensionless, so called, spectral index. The third parameter E_0 is the reference energy.
The second spectral model is the power law spectral model with an exponential cutoff described by

$$\Phi(E) \;=\; \Phi_0 \cdot \left(\frac{E}{E_0}\right)^{-\Gamma} \; e^{-(\lambda\, E)^{\alpha}}. \tag{16}$$

The first mentioned simple power law spectral model is a special case of the more general power law model with an exponential cutoff. The two additional parameters in the latter model are λ and α. Former can be simply called cutoff, particularly, it is the inverse of the cutoff energy, thus, it is generally given in units of TeV-1. Latter one is the cutoff exponent that is dimensionless such as the the spectral index.

4.3.2.2. Spatial models

The first used spatial model describes point-like sources. In this case, the flux can be described by a δ-function centered around the coordinates $(\mathrm{lon}_0, \mathrm{lat}_0)$ of the source via

$$\Phi(\mathrm{lon}, \mathrm{lat}) \;=\; \delta(\mathrm{lon} - \mathrm{lon}_0, \mathrm{lat} - \mathrm{lat}_0). \tag{17}$$

If the point source is centered at one pixel, all its flux is assigned to this pixel. Otherwise, the flux is re-distributed across 4 neighbouring pixels to ensure conservation of the center of mass position.
A further model of interest is the Shell spatial model. Its flux is defined as follows:

$$\Phi(\mathrm{lon}, \mathrm{lat}) \;=\; \frac{3}{2\,\pi\,(r_{out}^3 \;-\; r_{in}^3)} \cdot \begin{cases} \sqrt{r_{out}^2 \;-\; \theta^2} \;-\; \sqrt{r_{in}^2 \;-\; \theta^2} & \text{for}\, \theta \;<\; r_{in} \\ \sqrt{r_{out}^2 \;-\; \theta^2} & \text{for}\, r_{in} \;\leq\; \theta \;\leq\; r_{out} \\ 0 & \text{for}\, \theta \;>\; r_{out}. \end{cases} \tag{18}$$

In above equation, θ is the sky separation to the model center, r_{in} is the inner radius of the radiating shell, r_{out} its outer radius. The distance between the inner and outer radius is called width and describes the width of the radiating shell. Both, the radii and the width of the shell are given in angular units. However, the flux of this model is brightest in between r_{in} and r_{out}. Outside the shell, the flux vanishes. For illustration, an exemplary Shell spatial model is shown in figure 15 a).
The last relevant - and the most important pre-defined one in the course of this work - spatial model is the Gaussian spatial model. This model is by default symmetric and assumes that the flux drops exponentially with increasing spatial distance to the center of the source. Formally, it can be parameterised by

$$\Phi(\mathrm{lon}, \mathrm{lat}) \;=\; N \cdot e^{-\frac{1}{2}\frac{1\,-\,cos(\theta)}{1\,-\,cos(\sigma)}} \tag{19}$$

where the normalization N is defined as

$$N \;=\; \frac{1}{4\,\pi\,a\left[1 - e^{-\frac{1}{a}}\right]},\; a \;=\; 1 \;-\; cos(\sigma). \tag{20}$$

Thereby, θ denotes the angular distance to the model center, and σ the extension of the Gaussian in angular units. In case of small values of the parameters θ and σ, the resulting flux can be reduced to the common Gaussian function, i.e. it reads

$$\Phi(\mathrm{lon}, \mathrm{lat}) \;=\; \frac{1}{2\pi\sigma^2}\, e^{-\frac{1\theta^2}{2\sigma^2}}. \tag{21}$$

It should be mentioned that up to this point, the definition only holds if the spatial morphology has circular shape, i.e. the eccentricity is chosen to be zero. This is the case for all the astrophysical sources sources within the ROI.

However, in the analysis that has been performed in the course of this thesis, not only astrophysical sources have been investigated, but also regions with large-scale diffuse γ-ray emission, e.g. in chapter 6. These sources cannot be simply described by circular Gaussian regions without an additional rotation angle ϕ and a vanishing eccentricity. In this case, an effective extension of the source has to be defined as

$$\sigma_{eff}(\text{lon}, \text{lat}) = \sqrt{(\sigma_M \cdot sin(\Delta\phi))^2 + (\sigma_m \cdot cos(\Delta\phi))^2}. \tag{22}$$

σ_M and σ_m are the major and minor semi-axis, respectively, of the Gaussian, $\Delta\phi$ is the difference between the rotation angle ϕ and the position angle of the evaluation point. Such a general Gaussian spatial model is shown in figure 15 b).

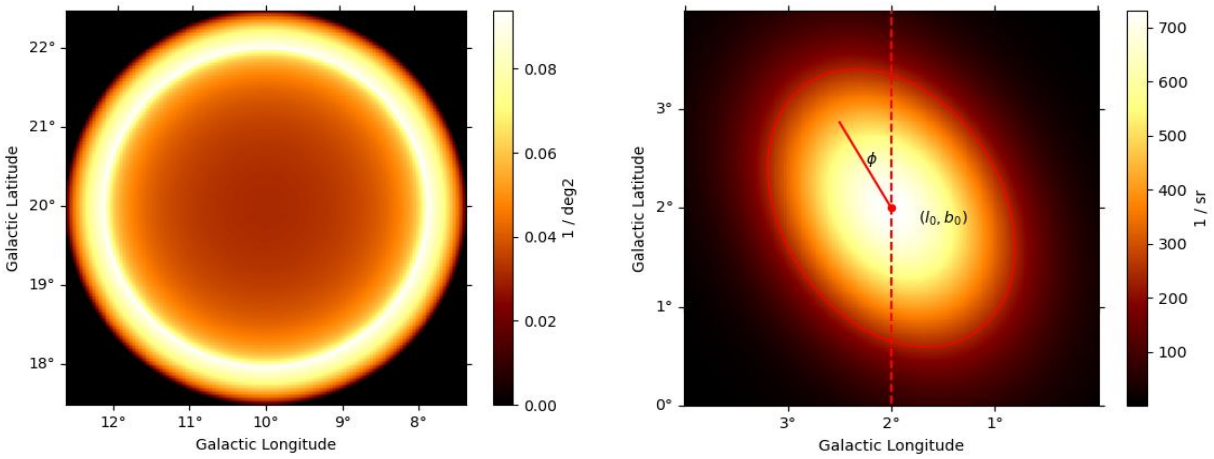

(a) Shell spatial model, from [52]

(b) Gaussian spatial model, from [53]

Figure 15: Illustration of Shell spatial and Gaussian spatial model. a) Shell spatial model: Between the inner and outer part of the shell, the model is brightest. b) Gaussian spatial model: The length of the major semi-axis is set to 1°. The vertical dashed red line indicates the orientation of the model. It is rotated $\phi = 30°$ with respect to this axis and has an eccentricity of 0.7. The additional solid red line represents the 1σ contour of the Gaussian distribution.

Furthermore, it is also possible to define own spatial templates provided by the class `TemplateSpatialModel`. These templates are fixed and can be for example based on hydrogen column density maps. In this thesis, various `TemplateSpatialModels` have been used when describing regions with diffuse emission within the ROI. The derivation and use of these templates is described in the chapters 5.4.2 (CMZ model) and 7.3 (hydrogen templates).

4.4. Fitting and binned Maximum Likelihood method

The various models introduced in the former section can be fitted to the data via adjusting their free parameters. Therefore, a fitting routine is implemented in Gammapy, namely the class `Fit` using the technique of a maximised Likelihood function which will be explained in the following lines. This class allows the use of different fitting back-ends. By default, the `minuit` [12] back-end is chosen.

Moreover, it is possible to fit models to single datasets, to `stacked` datasets (stacked fit) or to distinct datasets in one fitting procedure (joint fit). If in latter case one model is assigned to more than one of the inspected datasets, the final Likelihood for the model is the product of

[12] `https://iminuit.readthedocs.io/en/stable/index.html`

the single Likelihoods of the different datasets. In contrast to this, a stacked fit just returns one single Likelihood value. As mentioned in chapter 4.2.2, during the stacking, IRFs of the datasets are averaged. Thus, stacked fitting is less accurate, but faster than a joint fit.
However, the detected counts for an IACT follow Poisson statistics. Using this, the binned Likelihood can be written down ([54], following the notation in [55]) as

$$\mathcal{L}(\xi) = \prod_{i=1}^{N} \frac{\nu_i^{n_i}(\xi)}{n_i!} \cdot e^{-\nu_i(\xi)} \tag{23}$$

where the Poisson probability to observe n_i events in bin i has been used. $\nu_i(\xi)$ is the combined prediction of counts and background in the same bin and ξ a set of parameters, i.e. the Likelihood for the whole set ξ is a product of the Likelihoods of the single bins. The bins i are thereby the pixels of the dataset's maps the models are fitted to [55].
In addition, it is desirable to introduce a measure that allows for a quantification how well the data are described by the fit. Therefore, the *test statistics* (TS) can be defined as

$$TS = -2\,ln\left(\mathcal{L}(\xi)\right) = -2\sum_{i=1}^{N} ln\left(\frac{\nu_i^{n_i}(\xi)}{n_i!} \cdot e^{-\nu_i(\xi)}\right) \tag{24}$$

where it has been used that the logarithm of products can be re-written as sum of logarithms. As $-ln\left(\mathcal{L}(\xi)\right)$ is minimised, $\mathcal{L}(\xi)$ is maximised. The negative sign is just a convention to facilitate the calculations. This formula can be further simplified to

$$C = -2\sum_{i=1}^{N}\left[-\nu_i^{n_i}(\xi) + n_i\,ln(\nu_i)\right] = 2\sum_{i=1}^{N}\left[\nu_i^{n_i}(\xi) - n_i\,ln(\nu_i)\right]. \tag{25}$$

In equation (25), it was used that, since the expression $\frac{1}{n_i!}$ does not depend on the model, it can be dropped here. The definition given in this equation is furthermore known as Cash statistic, introduced by and named after Webster Cash [56].
Note that the above methodology only works if a model that predicts the background exists. Since this is the case in this thesis, Cash statistic can be used as a tool. If no predicted background counts are known, therefore a so called *nuisance* parameter can be introduced. If some prior knowledge on this *nuisance* parameter is know, the original Likelihood can be expanded in a way that strong deviations from the expected value are penalised [55].

4.4.1. Significance estimation

When performing an analysis on a set of data, it is important to know whether an emission is observed at a significant level. In astrophysics, observations at a significance level of $5\,\sigma$ or higher are usually defined as discovery. Additionally, when fitting different models to a certain set of data, it is useful to figure out which of the models works better and at which level of significance one model may be preferred over another one.
However, it is not possible to find exactly one solution to reliably solve these issues since the actual significance depends on statistical and systematical properties, but not all descriptions can properly account for both. In this thesis, two approaches to estimate the significance of γ-ray emission are used. The first one is the Likelihood ratio test. Another possibility is to inspect the fractional residuals in a certain region. Afterwards, the dataset can be `faked`, the fractional residuals can be computed for the `faked` dataset and compared to before, i.e. the case of the non-`faked` dataset.

4.4.1.1. Likelihood ratio test

The Likelihood ratio test is based on the comparison of two models that are fitted to the data. The two competing models, a null model (null hypothesis H_0) and an alternative model (general case H_1), can be compared regarding their ability to properly describe common data via the Likelihood ratio test. The difference of Test statistics is defined as

$$\Delta TS = TS_{\text{null model}} - TS_{\text{alternative model}} = -2\,ln\left(\frac{\mathcal{L}_{\text{null model}}}{\mathcal{L}_{\text{alternative model}}}\right). \tag{26}$$

Note that the null model's absolute TS value should be smaller than the one of the alternative model [57]. However, mathematically this only holds if the compared models are nested (the parameter space of the null model has to be a subset of the one of the alternative model). Applying Wilks' theorem [58], ΔTS is χ^2 distributed. Using this property and the difference of degrees of freedom (i.e. the fitted parameters per model) between the two models, a p-value can be computed via the cumulative distribution function for χ^2 statistics. The p-value describes the probability that ΔTS is larger than its observed value when H_0 is true [57].
This p-value can the be further used to calculate a significance value under assumption of a certain distribution, usually a Gaussian. Two possibilities of hypothesis testing are shown in figure 16, i.e. the right-tailed test in a) and the two-sided test in b). In this case, the right-tailed test is of interest. Therefore, a p-value of approximately $2.9 \cdot 10^{-7}$ which corresponds to a significance of $5\,\sigma$ is required to discard H_0.
Comparable results can be also achieved by the calculation of $\sqrt{\Delta TS}$. This result can be directly used to estimate the significance level at which the alternative model is preferred over the null model [55].

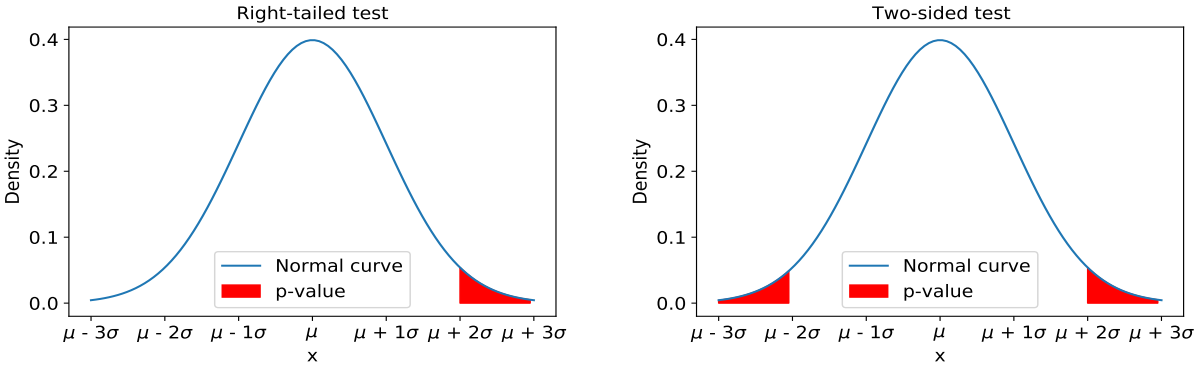

(a) Right-tailed hypothesis test

(b) Two-sided hypothesis test

Figure 16: Definition of the p-value under assumption of a Gaussian distribution. The red-shaded area under the normal curve corresponds to the p-value. It is sketched at some arbitrary position for visualisation. A p-value as sketched in a) means that the alternative model is preferred over the null model at a significance level of 2σ.

In practice, the Likelihood ratio test can be used to determine the significance of emission in a certain region. A standard procedure for significance estimation can be described as follows: The null model can consist of all models that are not used to describe the emission region of interest directly. The alternative model then contains an additional model that aims to cover the emission of interest. Since the null model is a special case of the alternative model (e.g. via restricting the spectral amplitude of the additional component of the alternative model to zero), the two models are nested and Wilks' theorem can be applied [57]. The significance level at which the alternative model is preferred over the null model, i.e. the significance of the radiation,

can the be determined as described above.
It should be noted that the Likelihood ratio test is a statistical measure of how well various models are suited to describe the emission. It doesn't contain information on systematics. Hence, it is useful to look at an approach that also takes into account systematics.

4.4.1.2. Fractional residuals

For the purpose of investigating systematic and not only statistical uncertainties, the fractional residuals are introduced. They are defined as

$$FR_i = \frac{\text{counts}_{\text{data,i}} - \text{counts}_{\text{model,i}}}{\text{counts}_{\text{background,i}}} \tag{27}$$

where $\text{counts}_{\text{data,i}}$ and $\text{counts}_{\text{model,i}}$ are the measured an model-predicted γ-ray counts and $\text{counts}_{\text{background,i}}$ are the background counts. Index i labels the spatial pixels inside the selected region. When using fractional residuals for significance estimation, the data are summed over all energies, i.e. the problem reduces to the two-dimensional case. All the required information are stored in a `MapDataset` and can be easily accessed.
In a certain region around γ-ray emission, the fractional residuals can now be calculated for all single pixels and the resulting values can be represented as histograms. The distribution of fractional residuals in a region is nearly Gaussian. Hence, a Gaussian fit on the histogram can be performed to determine mean value and standard deviation of the distribution. To estimate the significance in a given region, one can compare the fractional residuals that have been calculated for the desired dataset to the distribution of fractional residuals that have been determined for the same, but `faked` dataset (see chapter 4.2.2). A Gaussian distribution can be also fitted to the results achieved using the `faked` dataset. The significance of the difference of the distributions' mean values is then defined as

$$\sigma_{\text{emission}} = \frac{\mu_{\text{real}} - \mu_{\text{fake}}}{\sqrt{\sigma^2_{\text{real, pix}} + \sigma^2_{\text{fake, pix}}}} \tag{28}$$

where

$$\sigma_{\text{real, pix}} = \frac{\sigma_{\text{real}}}{\sqrt{\text{n}_{\text{pixels,ROI}}}} \quad \text{and} \quad \sigma_{\text{fake, pix}} = \frac{\sigma_{\text{fake}}}{\sqrt{\text{n}_{\text{pixels,ROI}}}}. \tag{29}$$

μ_{real} and μ_{fake} are the mean values and σ_{real} and σ_{fake} the standard deviations of the fractional residuals distributions for the actual and faked dataset, respectively. $\text{n}_{\text{pixels,ROI}}$ is the number of pixels within the region around the emission of interest.
Note that `faking` a dataset is a statistical process. Thus, it is not sufficient to compare the actual dataset to only one faked dataset. However, the significance level can be assessed via determining significance of the fractional residuals for multiple `faked` datasets ($\propto 1000$). The distribution of significance values follows a Gaussian if enough significance values are calculated. The mean of the resulting distribution then is a measure for the lower boundary for the significance of the emission.

4.4.2. Gammapy features

In addition, Gammapy contains some handy features to treat statistics. Cash statistic is implemented in the class `CashCountsStatistic` as well as the function `cash`. Latter one performs a calculation similar to equation (25). A class that is built on `CashCountsStatistic` is the `ExcessMapEstimator`. It allows to read in a dataset with assigned models. It is then possible to calculate the Cash statistic of each spatial pixel within an energy range that is manually set. A

correlation radius can be additionally chosen [49]. Within this thesis, the `ExcessMapEstimator` has been used to determine the $\sqrt{TS}$ value in each pixel. A $\sqrt{TS}$ map covering the desired FoV can then be created. The advantage of the `ExcessMapEstimator` is that regions that show γ-ray emission can be quickly found by eye. It can be also investigated whether a model is capable of describing a source or region. Significance estimations and modelling of these emission regions are then performed via the tools introduced in the previous chapters.
Moreover, The `FluxPointsEstimator` provides the function to calculate flux points for selected `SkyModels` of `MapDatasets`. Therefore, the amplitude of the best-fit spectral model is normalised to a reference spectral model. Via bin-by-bin Likelihood approach, this is done for all energy bins separately [49], [59].

5. Analysis of the full ROI (HESS I data)

In this section, the analysis of HESS I data in the ROI spanning $\pm 10°$ in galactic longitude and $\pm 5°$ in galactic latitude is presented. The motivation is to describe all the known sources in the ROI, e.g. astrophysical sources and the CMZ. If all these sources are properly described, it may be possible to see a signal from the *Fermi* Bubbles. The following chapter describes the basic setup as well as quality criteria. Afterwards, the background refitting procedure is described to obtain a full dataset. Finally, the models assigned to the dataset are introduced and the results of the fitting procedure are shown and discussed.

5.1. Data selection

The most important information on the analysis can be summarised as follows:

- H.E.S.S. era: HESS I
- ROI: $\pm 10°$ in gal. longitude, $\pm 5°$ in gal. latitude
- Analysis chain: HAP, version hap-18-pl05, tables version Prod05
- std ImPACT
- Background model version (std ImPACT): hess_bkg_3d_v07c_fov_radec
- Analysis software: Gammapy v0.18.2

In the first step, all available observations with pointing directions inside the ROI are selected. In addition, the following quality cuts are applied [60]:

- Zenith angle (pointing direction) $< 60°$
- Maximum offset $< 2.2°$
- All four 12 m telescopes have to be active during one observation
- On-time > 1500 s
- Number of detected counts during one observation > 1500

Note that only data from the the small telescopes CT1 to CT4 have been taken into account. The reason therefore is that there is no reliable background model for the hybrid mode (i.e. including CT5) yet. The maximum offset condition means that all data outside a circular region with radius of $2.2°$ away from the pointing direction are masked, since large systematic uncertainties are expected outside. Lower limits on the number of detected counts and on-time per observation are set to avoid problems in the background refitting procedure per observation, i.e. negative background normalisation. A total amount of 884 observations is available after application of these quality cuts.

5.2. Datasets

The geometry of the datasets is chosen as

- Pixel (spatial bin) size: $0.1° \times 0.1°$
- Energy range: 0.1 TeV - 100 TeV
- 16 energy bins per decade
- Size of dataset of a single observation: $5° \times 5°$

To reduce the effect of systematic uncertainties, energy bins close to the instrument energy threshold have been masked. Two thresholds are defined for this purpose. First to name is the bias threshold $E_{\mathrm{thr}}^{\mathrm{bias}}$, i.e. the bias of the energy reconstruction should not exceed 10 % within the maximum offset angle. Furthermore, a background threshold $E_{\mathrm{thr}}^{\mathrm{bkg}}$ is applied. It is based on the background prediction for each energy bin and is defined as the upper boundary of the energy bin with the highest predicted background rate [50]. For each observation, $\max(E_{\mathrm{thr}}^{\mathrm{bias}}, E_{\mathrm{thr}}^{\mathrm{bkg}})$ is chosen as energy threshold. The mean energy threshold is determined to be (0.40 ± 0.16) TeV for the selected HESS I observations. The lowest energy threshold for a single observation was found to be 0.27 TeV.

5.3. Background refitting per observation

In a next step, the remaining observations are stacked to a single dataset covering the full ROI. The exposure map of this stacked dataset is shown in figure G1 a) in appendix G. Before stacking, the normalisation and tilt of the *FoVBackgroundModel* model of each single observation are refitted. During this process, regions known for emission of γ-rays (i.e. astrophysical sources and the CMZ) are masked such that they are not taken into account when refitting the background. The *Fermi* Bubbles ROI defined in chapter 2.3 figure 4 has been masked to avoid a possible contamination with the *Fermi* Bubbles. Note that *Fermi* Bubbles ROI denotes the region inside the *Fermi* Bubbles template while ROI without the prefix *Fermi* Bubbles refers to the full analysed ROI in the course of this thesis, i.e. $\pm 10°$ in galactic longitude and $\pm 5°$ in galactic latitude. The resulting mask is presented in figure 17.

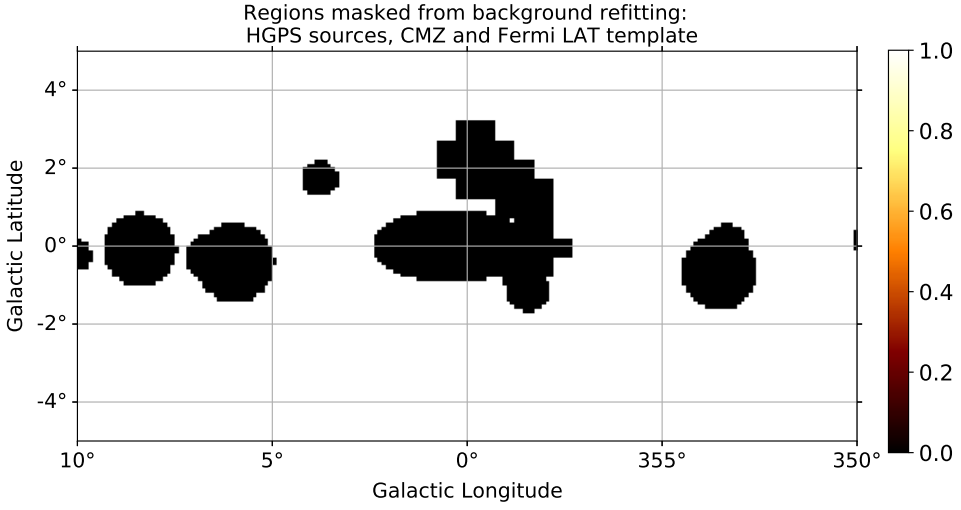

Figure 17: Exclusion mask around all regions that are known for γ-ray emission beforehand.

The distributions of the best-fit parameters for normalisation and tilt are presented in appendix A.1 in figure A1. Both distributions are Gaussian-shaped as expected. The mean normalisation is found to be 0.94 ± 0.11, the mean tilt to be 0.07 ± 0.13. Furthermore, observations where the best-fit normalisation parameter turned out to be negative were not stacked to the full dataset, but discarded. In this analysis, this issue appeared only in one observation.

5.4. Applied models

In this analysis, the ROI is described by three different kinds of models. The first applied model is the 3D background model already discussed in chapter 4.3.1. The two parameters normalisation and tilt have been left as free parameters. Additionally, the models of the 12 astrophysical sources that were significantly detected by H.E.S.S. in the ROI are added. These `SkyModels` are composed from in-built Gammapy models as presented in chapter 4.3.2. Furthermore, a model to describe the emission in the CMZ has been added.

5.4.1. Astrophysical sources

The initial models and parameters for the different astrophysical sources have been taken from the HGPS catalog available in Gammapy and containing data from the H.E.S.S. Galactic plane suvey (HGPS) [61]. During the HGPS campaign, sources in a region from $\pm 3°$ in galactic latitude and $250° - 65°$ in galactic longitude have been investigated. Note that not all of the known H.E.S.S. sources could be re-detected during the HGPS. In these cases, the catalog contains the best published fit results. For sources that have been re-analysed in the course of HGPS, the parameters values may differ from the best fit values found in single-source observations. Nevertheless, the models from the HGPS catalog can be used as starting point for the analysis. An overview on the HGPS sources, their positions and types of models are presented in table 1. A few things should be noted:

- Kind of models and initial parameters are taken from HGPS catalog [61].
- HGPS catalog also contains errors on the given parameters for most of the spectral and spatial parameters. If no errors on the literature values are given in the following, the catalog does not contain information on these errors.
- All the HGPS sources described by Gaussian spatial models are symmetric Gaussians, i.e. eccentricity e and rotation ϕ are fixed to zero.
- The source *HESS J1804-216* [62] consists of two Gaussian-shaped components, namely *HGPSC 054* and *HGPSC 055*.

No errors on the positions of the sources are given in table 1, since its purpose is to only give a summary of the analysed sources. The spatial parameters of the HGPS sources taken from the catalog can be found in table C1 in appendix C.1 and the spectral ones in table C2 in appendix C.2.
The free and fixed parameters of the spatial models are shown in table 2 and the ones of the spectral models in table 3. Note that independent of the individual source, all models of a certain class have been assigned the same set of free and fixed parameters.

5.4.2. Diffuse emission within the *Central molecular zone*

In the vicinity of the GC, a dense matter distribution containing mainly molecular gas, namely the CMZ, has been found to extend from $\approx 250\,\mathrm{pc}$ at positive longitudes up to $\approx 150\,\mathrm{pc}$ at

Table 1: HGPS sources in the ROI. Data taken from HGPS catalog [61].

HGPS source	Position (lon, lat) in °	Spectral model	Spatial model
HESS J1729-345	(353.39, -0.02)	Power law	Gaussian
HESS J1731-347	(353.54, -0.67)	Power law	Shell
HESS J1741-302	(358.28, 0.05)	Power law	Point-like
HESS J1745-290	(359.95, -0.04)	Power law with exponential cutoff	Point-like
HESS J1745-303	(358.65, -0.56)	Power law	Gaussian
HESS J1746-285	(0.14, -0.11)	Power law	Point-like
HESS J1746-308	(358.45, -1.11)	Power law	Gaussian
HESS J1747-248	(3.78, 1.72)	Power law	Gaussian
HESS J1747-281	(0.87, 0.08)	Power law	Point-like
HESS J1800-240	(5.96, -0.42)	Power law	Gaussian
HESS J1801-233	(6.66, -0.27)	Power law	Gaussian
HGPSC 054	(8.45, 0.00)	Power law	Gaussian
HGPSC 055	(8.25, -0.29)	Power law	Gaussian

Table 2: HESS I analysis of the full ROI: Free and fixed parameters of the spatial components of the HGPS sources models.

model	Free parameters	Fixed parameters
Gaussian	lon, lat, σ	e, ϕ (fixed to 0)
Shell	lon, lat	r, width (fixed to HGPS catalog values)
Point-like	lon, lat	-

Table 3: HESS I analysis of the full ROI: Free and fixed parameters of the spectral components of the HGPS sources models.

model	Free parameters	Fixed parameters
Power law	Φ, Γ	E_0
Power law with exponential cutoff	Φ, Γ, λ	α, E_0

negative longitudes [63]. One of its most interesting features is the very high energetic γ-ray emission that can be observed within this region. Figure 18 shows the residual significance map of the region close to the GC. The image shows the significance for this region after the two known point-like γ-ray sources (*G0.9+0.1* and *HESS J1745-290*) have already been subtracted from the signal, i.e. the strong remaining emission seems to be of diffuse origin [64]. Additionally, cyan contour lines are contained in figure 18.

These are a measure of the molecular gas density in form of CS brightness. It can be clearly seen that the contour lines resemble the shape of the large-scale γ-ray emission suggesting a hadronic origin of the observed emission [63]. CRs can reach energies up to 10^{15} eV, accelerators of such high energetic CRs have consequently been named *PeVatrons*. It is proposed that Sgr A* is also linked to such a *PeVatron*, i.e. extremely high energetic protons can be created in (or very close to) the GC [63].

However, since these protons are charged, they can be deflected by the strong magnetic fields in this region making it impossible to determine their exact origin. The protons then travel through the CMZ via diffusive propagation and interact with the dense matter cloud of the CMZ. For details on the hadronic origin of γ-ray see chapter 2.1.2. Since the radial distribution

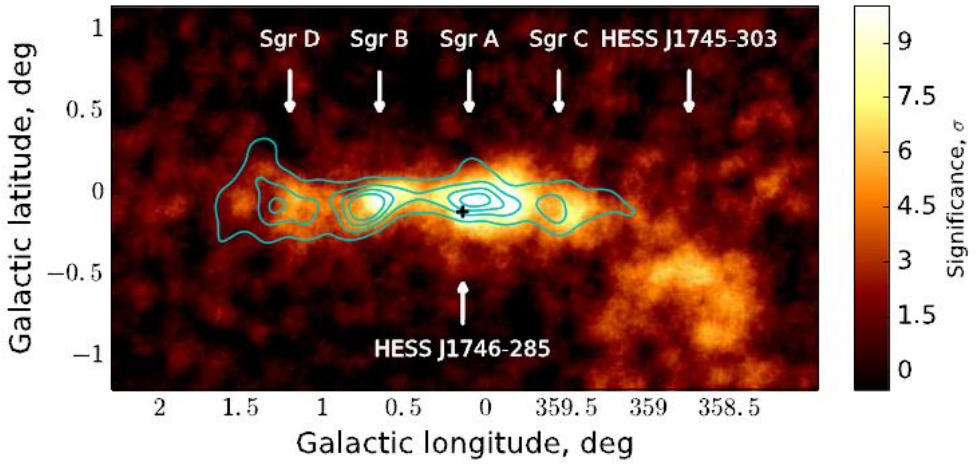

Figure 18: Residual significance map of the CMZ. The additional cyan contours represent the molecular gas density. Figure taken from [64].

of CRs in the CMZ behaves $\propto \frac{1}{r}$, with r the projected distance to the center, a quasi-continuous injection of protons into the CMZ from a centrally located accelerator is favoured. It can be furthermore shown that the spectrum of this γ-ray emitting region can be nicely fitted using a power law model [63].
This allows for an implementation of a physics-based model aiming to describe this region. The model used in this analysis was developed and provided by Yu Wun Wong [65]. It is based on the assumption that the protons in an energy range from 100 GeV to 100 PeV are injected in the GC which can be justified by the observations discussed before. These protons are additionally assumed to spread isotropically. Taking into account the diffuse movement of the protons as well as the molecular gas density and $p-\gamma$ conversion, a spatial template has been created. The template has been refined by fitting it to combined data from HESS I, Iu and II. In this way, best fit values for the diffusion parameters (diffusion time and diffusion coefficient) of the protons could be determined [66]. The resulting `TemplateSpatialModel` (summed over all energies) is shown in figure 19 and is given in units of cm-2 s-1 sr-1 TeV-1. This spatial model is fixed and combined together with a *PowerLawNormSpectral* model (as in case of the 3D background model) to build a `SkyModel`. Note that the normalisation has been left as the only free parameter of this model.

5.5. Fit results

The process of fitting the models to the data has been divided into multiple steps. In a first step, the spatial models of the HGPS sources have been fitted together with the free parameters of the background model and the CMZ diffuse emission model. Afterwards, the spectral parameters of the HGPS sources models have been adjusted (while spatial parameters were fixed), again together with the free parameters of the CMZ and background model.
The results for the fitted parameters of background and CMZ diffuse model are shown in table 4. The detailed fit results of the spatial models of the HGPS sources are added to the literature values in table C1 in appendix C.1 and the spectral parameters to table C2 in appendix C.2.
Moreover, the plotted spectra of the fitted HGPS sources can be checked and compared to the ones given in the catalog. The fitted spectrum of *HESS J1731-347* fits the spectrum from the

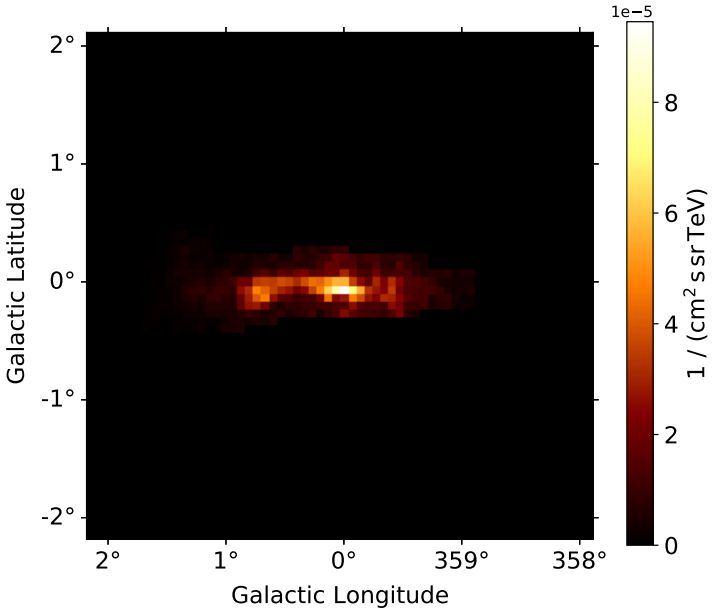

Figure 19: Spatial template for the CMZ developed by Yu Wun Wong summed over all energies [65].

Table 4: HESS I analysis of the full ROI: Fit results for background and CMZ model

Model	normalisation	tilt δ
`FoVBackgroundModel`	1.0098 ± 0.0011	-0.0081 ± 0.0013
CMZ model	1.58 ± 0.04	0.0 (fixed)

catalog accurately, while the results for *HESS J1729-345* show a larger deviation from literature. Both spectra are plotted in figure 20 a) and b), respectively. For these two sources, the ratios of literature values and the best-fit results for the parameters amplitude Φ and spectral index Γ, i.e.

$$\text{ratio}_{\Phi} = \frac{\Phi_{\text{best fit value}}}{\Phi_{\text{literature value}}} \quad \text{and} \quad \text{ratio}_{\Gamma} = \frac{\Gamma_{\text{best fit value}}}{\Gamma_{\text{literature value}}}$$

are shown in table 5. Especially the amplitude of the fitted spectral model of *HESS J1729-345* deviates by almost a factor of two from the literature. The other fitted parameters are consistent with the catalog. For the majority of the HGPS sources, the best-fit parameters of the spectral parameters are within ± 10 % of the literature values. Deviations from the catalog's results are expected, since the data used for the analysis may vary as well as a different background treatment has been made in the HGPS paper [61]. The fitted spectra of the further HGPS sources are printed in appendix A.2 in figure A2.

Table 5: HESS I analysis of the full ROI: Ratio of literature values and best-fit results for the fitted spectral parameters of two exemplary chosen HGPS sources, namely *HESS J1731-347* and *HESS J1729-345*.

Source	ratio_{Φ}	ratio_{Γ}
HESS J1731-347	1.04	1.00
HESS J1729-345	1.67	1.06

A first inspection of the residuals in the ROI after the fit is performed. For this purpose, the

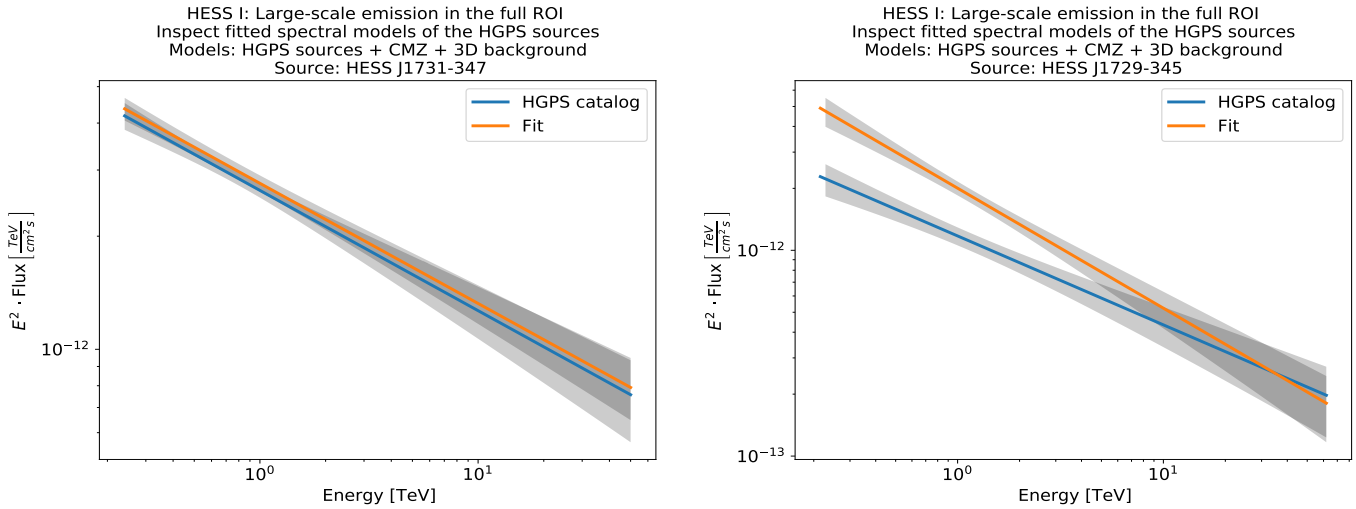

(a) Spectrum of *HESS J1731-347*

(b) Spectrum of *HESS J1729-345*

Figure 20: HESS I analysis of the full ROI: Spectra of the exemplary chosen HGPS sources *HESS J1731-347* and *HESS J1729-345* after having applied models for overall background, CMZ and the HGPS sources.

`ExcessMapEstimator` (introduced in chapter 4.4.2) with a correlation radius of 0.25° has been used. The resulting map is shown in figure 21 a). For visualisation, different contours have been added to the plot. The solid blue contour marks the spatial model that has been used to describe the CMZ. Solid black contours represent the spatial morphology of the HGPS sources using the initial parameters from the HGPS catalog. The contours of the fitted spatial parameters of the HGPS sources are plotted as dashed blue lines. To visualise point-like astrophysical sources, a small circle with a radius of 0.1° has been chosen. The Gaussian-extended sources are show as circles with a radius corresponding to the $1\,\sigma$ containment region. For *HESS J1731-347*, representing the only shell-like spatial model, the value of the radius has been selected as extension to plot the contour.
Three large-scale residuals are striking. In the following chapters 6 and 7, the focus will be on a proper description of these regions using additional models. As a first attempt, Gaussian spatial models are fitted to the three regions, afterwards a physically motivated description via hydrogen templates is applied.
The definition of the three regions is shown in figure 21 b). The same residual significance maps are shown in figure A3 in appendix A.3. Panel a) of this figure additionally contains the *Fermi*-LAT *Fermi* Bubbles template as defined in figure 4 using the black dashed contour. Figure A3 b) is equipped with labels for all of the modelled HGPS sources in the ROI.

5.6. Diffuse emission regions

Before applying additional models to the data, the extended emission areas are discussed in the following sub-chapters. Afterwards, an estimation of the significance of the observed emission regions is given. For visualisation of the results of the different large-scale emission regions, rectangular cutouts of the whole ROI are defined.

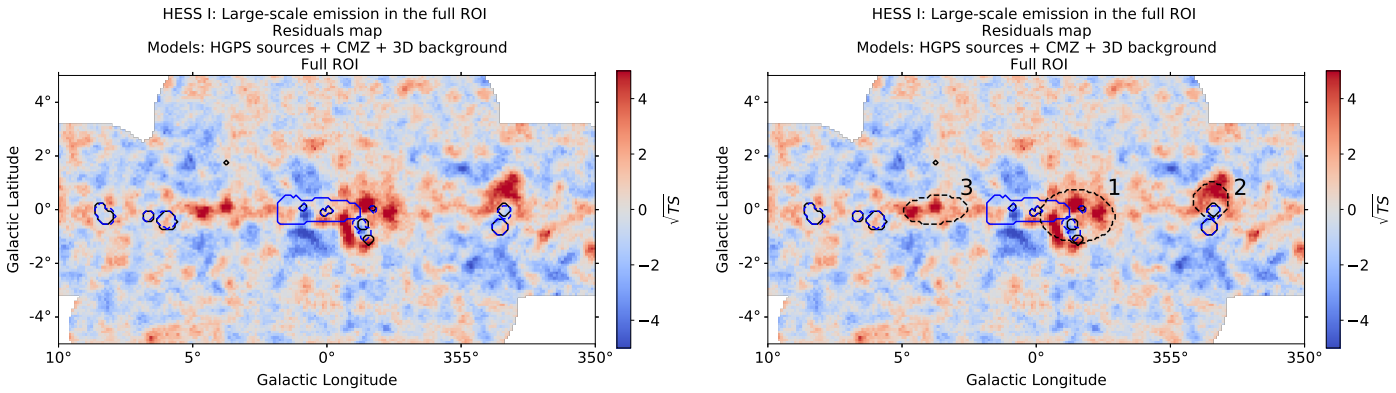

(a) Contours of CMZ and HGPS sources

(b) Definition of large-scale emission regions

Figure 21: HESS I analysis of the full ROI: Residual significance maps for the ROI used in this thesis. The maps are produced using the `ExcessMapEstimator` provided by Gammapy with a correlation radius of 0.25°. Models for the HGPS sources as well as an overall 3D background model and a CMZ model have been fitted. The solid blue contour shows the extension of the spatial template of the CMZ model, the solid black contours the extend of HGPS sources (catalog values) and the dashed blue contours the extend of the HGPS sources after fitting. Radius of point-like sources: 0.1°. Radius of Gaussian-extended sources: $1\,\sigma$. Radius of shell-like sources: outer radius of the spatial model. Additional dashed black contours around the three regions with large-scale residuals are drawn in b). The numbers next to these contours label these regions. The contours mark the $1\,\sigma$ regions of the Gaussian-shaped spatial models that have been fitted to the data in chapter 6.

Region 1

Region 1 is placed at negative longitudes next to the GC and marks the largest of the three diffuse emission regions in the ROI. Furthermore, the emission is observed around different astrophysical HGPS sources. The residual significance map cutout around this region is presented in figure 22 a) while the distribution of residual significance values per spatial pixel shown in this map is plotted in figure 22 b).

Taking a look at figure 22 a) strong reddish residuals ($\sqrt{TS}$-values up to five and even higher) are observed. On the other hand, the left part of the cutout tends to be overfitted, particularly it shows blueish pixels. Another observation is that the contours of two of the HGPS sources, namely *HESS J1745-303* and *HESS J1746-308*, are displaced from the catalog expectations. This may occur, since the large-scale emission is overlaid with the sources, possibly leading to uncertainties in the fit result.

As a first indication of the significance of the emission, the residual significance distribution in figure 22 b) can be taken into account. By eye, it is directly visible that the distribution for the fitted dataset containing the real data is much broader than in case of the `faked` dataset, i.e. σ is roughly by a factor two larger for the fitted dataset. Its mean is furthermore displaced from zero to positive values underlining the strong emission that can be seen in figure 22 a).

A first idea of the origin of the diffuse emission is that CRs, that have been accelerated by the *SNR G359.1-0.5*, interact with surrounding hydrogen and thus lead to emission of γ-rays. *SNR G359.1-0.5* has been observed in X-rays in close vicinity to *HESS J1745-303* and is supposed to be approximately 4 kpc away from the GC and in its front [67].

Inspecting the residuals map shown in figure A3 a), the observed emission is coincident with

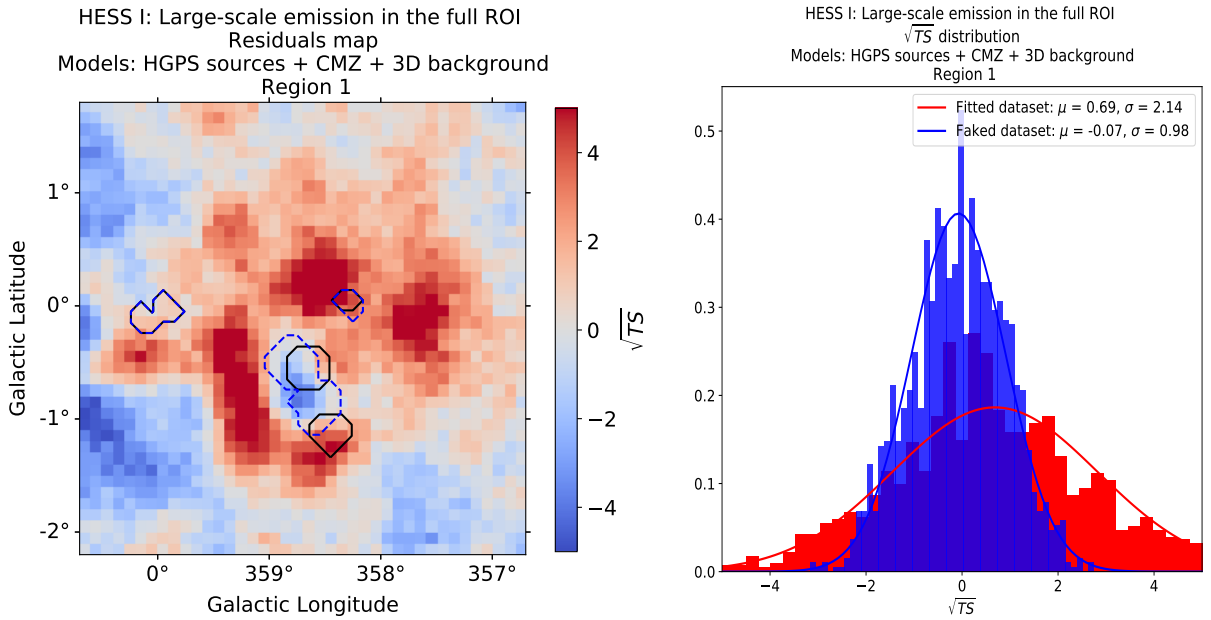

(a) Residual significance map for region 1

(b) Distribution of res. significance for region 1

Figure 22: HESS I analysis of the full ROI: Results for region 1. a) The contours of the HGPS sources are sketched via solid black (morphology as given in the source catalog) and dashed blue (fitted morphology of the HGPS sources) lines. b) Distribution of the residual significance values per spatial pixel. The blue distribution is for the `faked` dataset, the red distribution represents the results as shown in a). For a quantitative evaluation, to each of the both curves, a Gaussian distribution with mean μ and width σ is fitted.

the base of the *Fermi* Bubbles at very low latitudes, i.e. at $|b| < 1°$. However, at latitudes $> 1°$ (where brightness in the *Fermi*-LAT map (see figure 4 b)) is comparable to the one at zero latitude), there are no remarkable residuals. Additionally, one has to keep in mind that the exposure of the HESS I observations drops at increasing latitudes which can be seen in figure G1 a) in appendix G, i.e. the HESS I observations focus on the GC region itself. This makes it hard to decide whether *Fermi* Bubbles emission is observed in region 1 or not.

Region 2

The second region is positioned directly above (in means of the galactic latitude) the two HGPS sources *HESS J1729-345* and *HESS J1731-347*, particularly at galactic longitudes of approximately 353°. Residual significance map as well as distribution of the residual significance values per spatial pixel are shown in figure 23.
By taking a look at figure 23 a), large-scale emission is extending above the two HGPS sources. It is very likely that diffuse emission overlaps with the emission that is observed from the astrophysical source *HESS J1729-345*. This may explain why the fitted spectrum for this source showed large deviations from the literature values (see figure 20 and table 5). It is supposed that *HESS J1731-347* is a SNR. The emission observed from *HESS J1729-345* may be possibly explained by CRs escaping from the SNR and illuminating the nearby molecular clouds since the morphology of *HESS J1729-345* strongly resembles the morphology of observed molecular clouds [68], [61], [69]. However, no explicit assumptions on the origin of the observed diffuse emission above the HGPS sources are made in these papers. Since molecular clouds have been

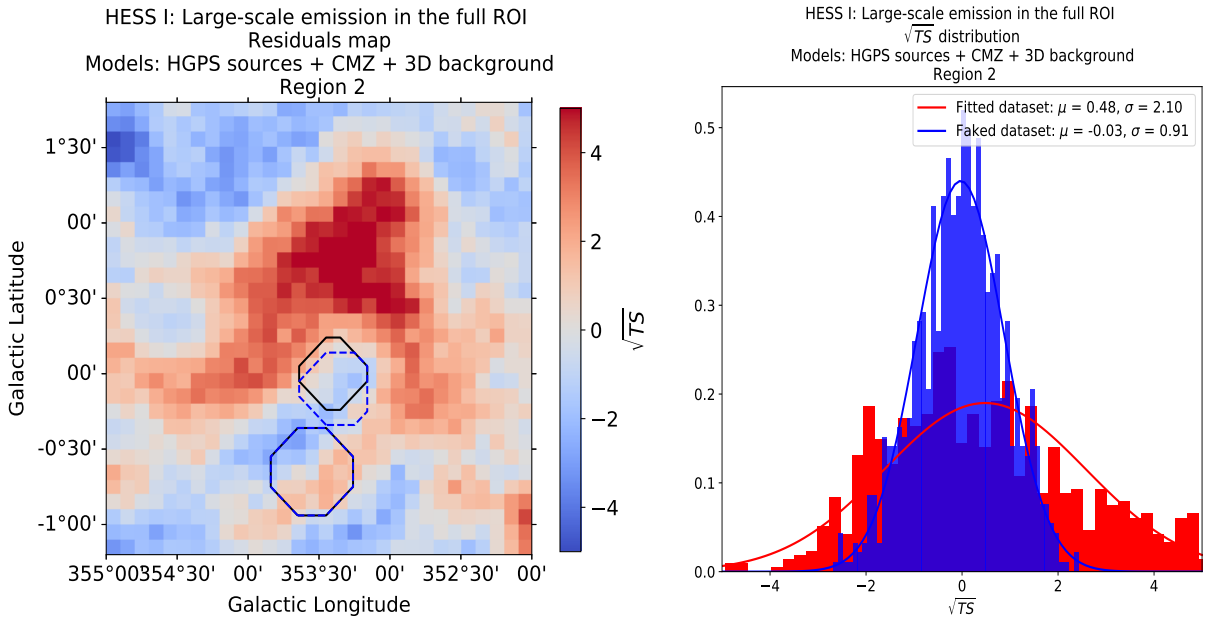

(a) Residual significance map for region 2

(b) Distribution of res. significance for region 2

Figure 23: HESS I analysis of the full ROI: Results for region 2. a) The contours of the HGPS sources are sketched via solid black (morphology as given in the source catalog) and dashed blue (fitted morphology of the HGPS sources) lines. b) Distribution of the residual significance values per spatial pixel.

observed in this region, it is likely that the large-scale emission is a result of molecular clouds illuminated by CRs. Nevertheless, it is not clear whether the HGPS sources *HESS J1729-345* and *HESS J1731-347* are directly connected to this emission or whether a hidden CR accelerator may be responsible.
Regarding the distribution of residual significance presented in 23 b), a similar behaviour as for region 1 is observed.

Region 3

The last region lies inside the GP at a galactic longitude of approximately 4°. No HGPS sources that may be responsible for this emission are in its direct neighbourhood. The results for the residual significance map and the corresponding histogram are plotted in figure 24.
Figure 24 reveals a bi-lobular structure of the emission. For this region, a scenario where a hidden CR accelerator illuminated molecular clouds is a reasonable approach, too.

5.7. Estimation of the significance of the diffuse emission regions

The significance of the emission in the different regions has been estimated via a Likelihood ratio test and an analysis of the fractional residuals as described in chapter 4.4.1. Both approaches are presented in the following.

5.7.1. Estimation via Likelihood ratio test using Gaussian spatial models

As first significance estimation, a Likelihood ratio test has been performed. Referring to chapter 4.4.1.1 for each large-scale emission region an additional `SkyModel` has been added separately to the models introduced before. A Gaussian spatial model has been chosen to describe the

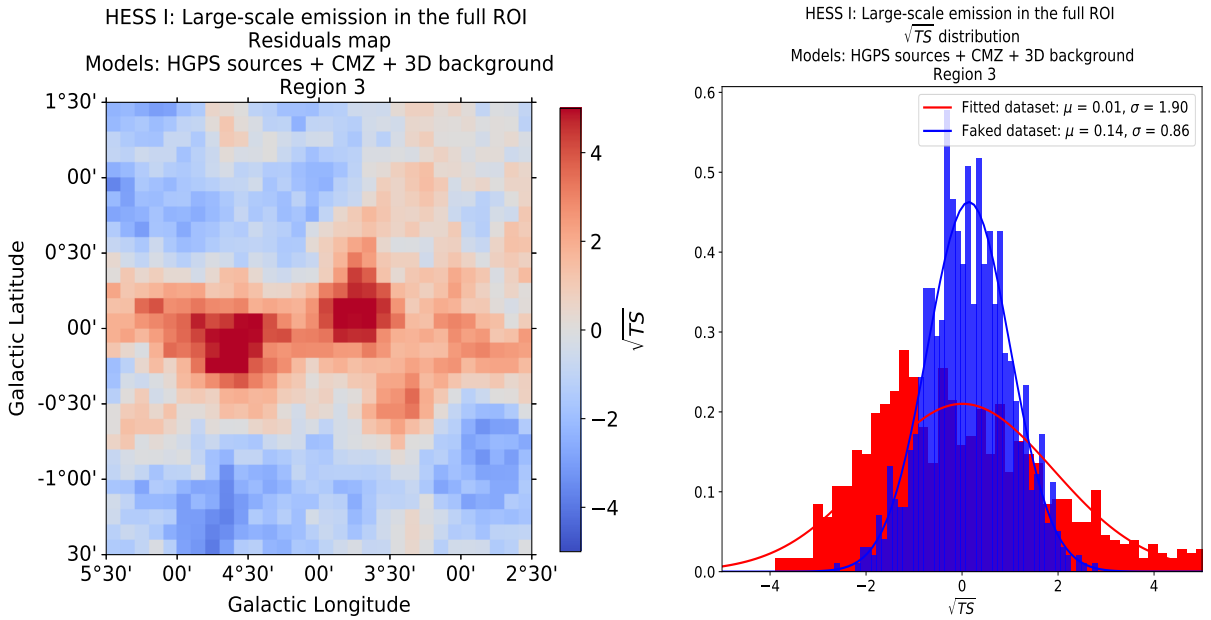

(a) Residual significance map for region 3

(b) Distribution of res. significance for region 3

Figure 24: HESS I analysis of the full ROI: Results for region 3. a) The contours of the HGPS sources are sketched via solid black (morphology as given in the source catalog) and dashed blue (fitted morphology of the HGPS sources) lines. b) Distribution of the residual significance values per spatial pixel.

spatial extension of the large-scale emissions, for the spectral component a power law approach has been used for regions 1 and 3. For region 2, a power law with an exponential cutoff has been added to the spatial model, since it turned out to work better for this region. An overview of the free parameters of the additional models is given in table 6.

Table 6: HESS I analysis of the full ROI: Free and fixed parameters of the additionally added Gaussians.

	model	Free parameters	Fixed parameters
Regions: 1, 3	Gaussian spatial	lon, lat, σ, ϕ	e
	Power law spectral	Φ, Γ	E_0
Region: 2	Gaussian spatial	lon, lat, σ	ϕ, e
	Power law spectral with exp. cutoff	Φ, Γ, λ	E_0, α

Compared to the basic model without any description of the large-scale emission regions, these new models provide 6 additional degrees of freedom. Since for all regions the fit failed when treating the eccentricity of the spatial model as a free parameter, it has been fixed beforehand. Therefore, an eccentricity value according to the morphology of the respective emission region has been set based on the residual significance maps shown in figure 21. Furthermore, for region 2, the best results were achieved when setting the eccentricity to 0. Thus, region 2 is modelled by a symmetric Gaussian spatial model and the rotation angle ϕ is a also fixed as it is redundant for a symmetric Gaussian. The starting values of the fitted parameters of the Gaussian spatial models have been set by taking a look at the residuals in figure 21, too. For the Power law spectral model, no starting values have been set explicitly, i.e. the standard model parameters set by Gammapy have been initially taken.

The fitting procedure has been again divided into multiple steps. Initially, spatial parameters of HGPS sources and added Gaussian models are fitted and afterwards their spectral parameters. Subsequently, the spectral parameters of the HGPS sources and the spatial parameters of the added Gaussians are refitted to achieve a proper result.
The results of the significance estimation via the Likelihood ratio test are contained in table 7. Therefore, the significance is estimated via $\sqrt{\Delta TS}$ and using the p-value from the χ^2 distribution to determine a significance value σ_{χ^2}.
The resulting $\sqrt{TS}$ maps for the whole ROI after having added one additional model for each region are shown in appendix A.4 in figure A4. The $1\,\sigma$ contours of the Gaussian spatial models are indicated via black dashed lines. Having a look at these plots, the additional models lead to clearly reduced emission in the regions they are applied to. The fitted parameters of the added Gaussians are printed in the tables A1 and A2 in appendix A.5. The best-fit models describing the full ROI for each of the separately added Gaussians are available as supplementary material in a folder [13] of the publicly accessible GitHub repository *HESS_HAP_extended_emission_and_FB* [14]. Since not all of the data achieved in the course of this thesis can be presented here, this repository has been set up.

5.7.2. Estimation via fractional residuals

The fractional residuals maps have been calculated according to equation (27) in chapter 4.4.1.2 for all three regions without having applied the additional Gaussian spatial models. The resulting map with a slight smoothing (Gaussian smoothing with a width of 0.075°) for region 1 is shown in figure 25 a). Since the finally determined significance estimation depends on the size of the area around the emission as seen in equation (28), a consistent definition of the region inside which the fractional residuals are determined is desirable. For this purpose, the fit results for the Gaussian spatial models describing the regions are used. To make sure that all the emission of interest is contained within the this Gaussian contour, its spatial extension σ has been multiplied by a factor of 1.5 for all three regions. This is indicated by the dashed black contour in figure 25 a). Part b) of the same figure shows the distribution of the non-smoothed fractional residuals for pixel-wise calculation inside this $1.5\,\sigma$ contour. The blue distribution is for the dataset with the real data to which the background, HGPS sources and CMZ models, but not the Gaussian spatial model have been added, the red distribution exemplary represents the results for the `faked` dataset.
From the data in 25 b) a significance estimation of the mean values of the two distributions following equation (28) is performed. The dataset has been `faked` 5000 times to take into account the statistics when a dataset is `faked`. The resulting significance values for each faking process are then plotted as histogram in figure 26 for all three regions.
A lower boundary for the significance of the three large-scale emissions is then obtained by taking the mean σ_{FR} of the significance distributions. The values are also printed in table 7.
Having a look at this table, all the three large-scale emission regions are accounted for as significant, i.e. the estimation via Likelihood ratio tests reveals a significance of at least $8\,\sigma$ for each region. This achievement is emphasised by estimating a lower significance boundary using fractional residuals resulting in significance values of at least $5\,\sigma$ for all regions. Hence, it is of interest to further describe the full ROI using refined models in the following chapters.

[13] `https://github.com/fabian-richter/HESS_HAP_extended_emission_and_FB/tree/main/Modelling_of_the_full_ROI/HESS_I/add_single_Gaussians`
[14] `https://github.com/fabian-richter/HESS_HAP_extended_emission_and_FB`

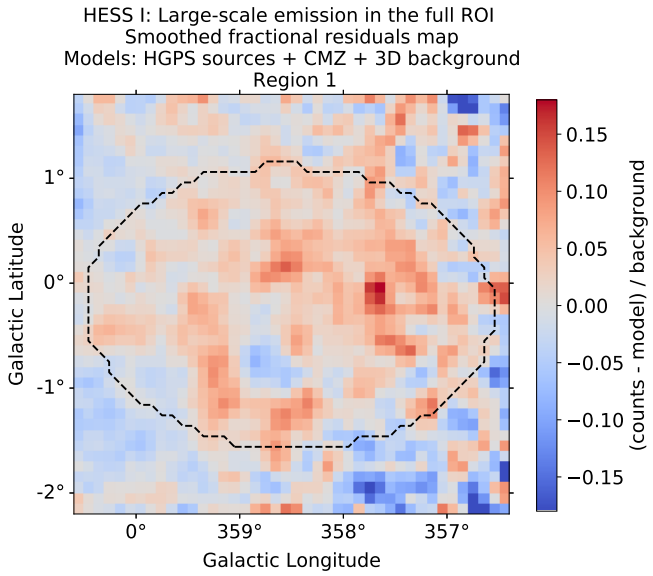

(a) Smoothed fractional residuals map around region 1

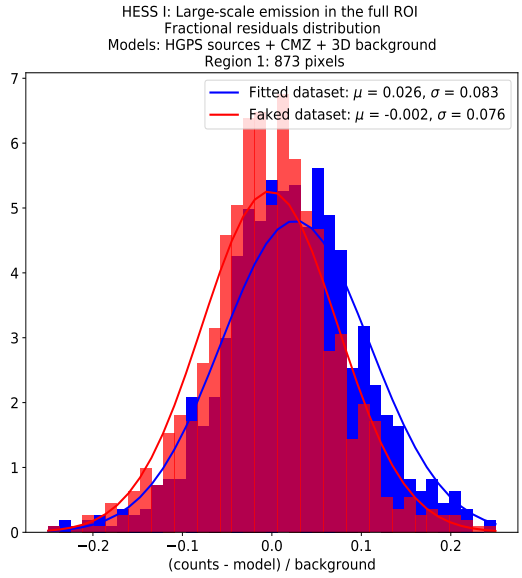

(b) Non-smoothed distribution of fractional residuals inside the Gaussian contour indicated on the left

Figure 25: HESS I analysis of the full ROI: Fractional residuals for region 1. a) The data in the map are smoothed using a width of 0.075°. The dashed black line indicates the $1.5\,\sigma$ contour of the best-fit Gaussian spatial model. b) The data shown are not smoothed and calculated inside the contour shown in a).

Table 7: HESS I analysis of the full ROI: Significance estimations for all three regions achieved by the different approaches. The number of additional degrees of freedom (dof) due to the Gaussian-shaped large-scale residuals models are also added to the table.

region	n_{pixels}	ΔTS	σ_{FR}	$\sqrt{\Delta TS}$	σ_{χ^2}	Additional dof
1	873	336.04	6.84	18.33	17.63	6
2	182	122.15	5.67	11.05	10.10	6
3	200	97.46	5.29	9.87	8.85	6

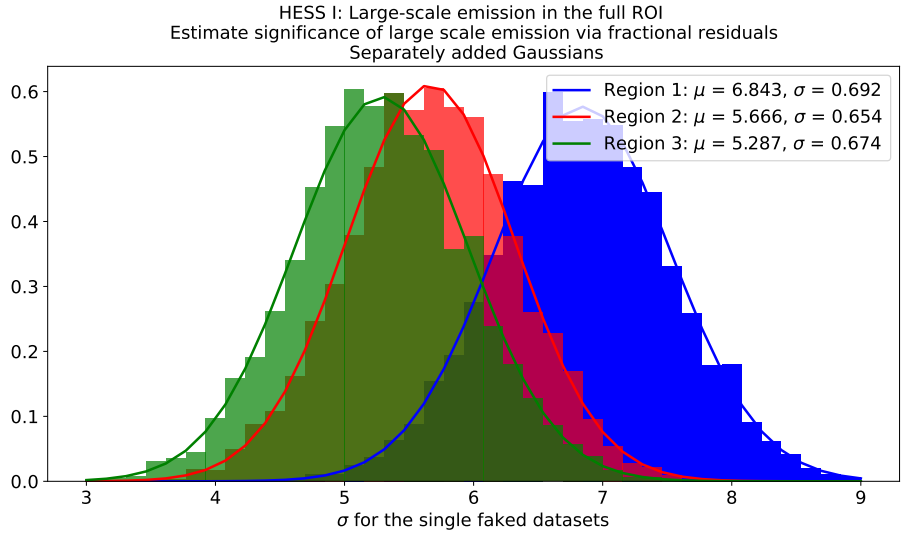

Figure 26: HESS I analysis of the full ROI: Significance distributions for the three large-scale emission regions in the ROI. The significance values have been determined by comparing the non-smoothed distribution of fractional residuals of the dataset to the distribution in case of the dataset after `faking`. Results are shown for 5000 `faking` processes.

6. Description of the diffuse emission regions in the ROI via Gaussian spatial models (HESS I data)

In this chapter, the three residual regions found in the previous chapter are described by the same types of `SkyModels` as introduced at the end of the previous chapter 5.7.1 where the significance of the single large-scale emissions has been estimated. In contrast to before where all residuals regions have been treated separately, models for all three regions are added to the ROI at the same time. This is necessary for an accurate description of the ROI since the models of the large-scale emissions act back on each other.

6.1. Data selection and datasets

The same configuration and data selection as well as quality criteria as presented in chapter 5.1 are used. Furthermore, the same geometry for the datasets is used (chapter 5.2).

6.2. Background refitting per observation

The first difference to former analysis is that before the Gaussian spatial models are added, the background refitting per observation has been repeated. The three large-scale emission regions are also masked from the run-wise background refitting. In combination with the mask shown in figure 17, the full exclusion mask used in this analysis is presented in figure 27.

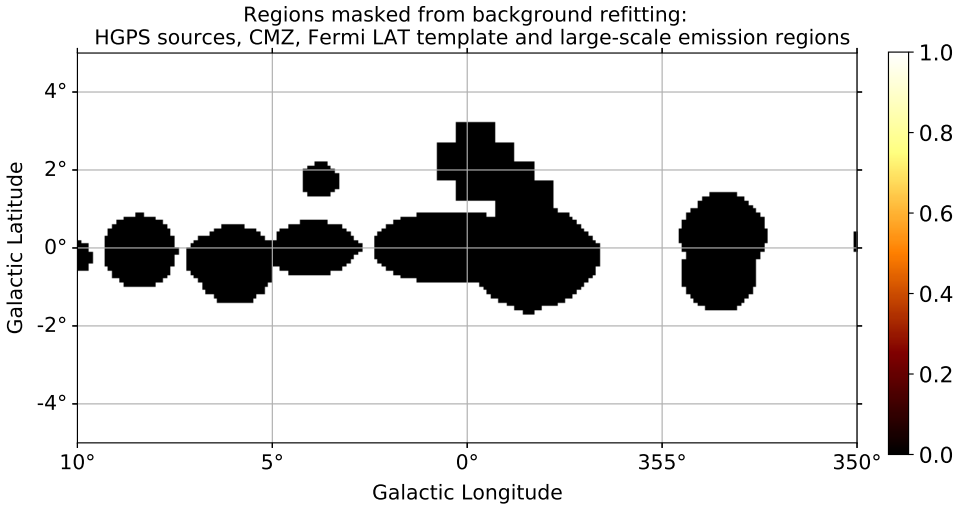

Figure 27: Exclusion mask around all regions that are known for γ-ray emission. The three large-scale emission regions that have been found in the analysis in the previous chapter are masked in addition to the beforehand known sources (figure 17).

The mean normalisation is found to be 0.94 ± 0.11, the mean tilt to be 0.08 ± 0.14. The distributions look very similar as the ones from the previous chapter presented in figure A1.

6.3. Applied models and fit results

The same models as introduced in chapter 5.4 are applied. `SkyModels` consisting of a Gaussian spatial model and a Power law spectral model with (region 2) and without (regions 1 and 3) an exponential cutoff are added. All of these three models have the same combination of fitted and fixed parameters as presented in table 6 in chapter 5.7.1, for the HGPS models the same configuration as shown in the tables 2 and 3 is used. The same set of free parameters as described

in chapter 5.4 is chosen for background and CMZ model. Furthermore, the initial parameters of all models are set to identical values as before and the same fitting procedure as described in chapter 5.7.1 is applied.
The detailed fit results of the spatial models of the HGPS sources are added to the literature values (and best-fit values without adding the Gaussians) in table C1 in appendix C.1 and the spectral parameters to table C2 in appendix C.2. The results for background and CMZ model are given in table B3 in appendix B.3. Moreover, the fit parameters of the 3 Gaussians are printed in appendix B.2 in table B1 (spatial components) and B2 (spectral components). Note that the fit results for the majority of the HGPS sources are not remarkably changed by adding the three models for the description of the residual regions. In particular, the fitted spatial parameters are almost unchanged. The spectral parameters on the other hand may have changed depending on the source. In most of the cases, the spectral parameters are only slightly changed (i.e. in a range of ± 10 % compared to before). However, for three HGPS sources, namely *HESS J1729-345*, *HESS J1741-302* and *HESS J1745-303*, the fitted spectral parameters show deviations of 20 % or even more from the previous results, e.g. the fitted amplitude Φ of *HESS J1729-345* is changed by $\approx$ 40 % and is now within ± 10 % of the results from the HGPS [61]. Its updated spectrum is shown in figure 28. For comparison, the spectrum of *HESS 1729-345* has already been shown in figure 20 b), before any additional Gaussian models have been applied. It is clearly visible that the result has improved.

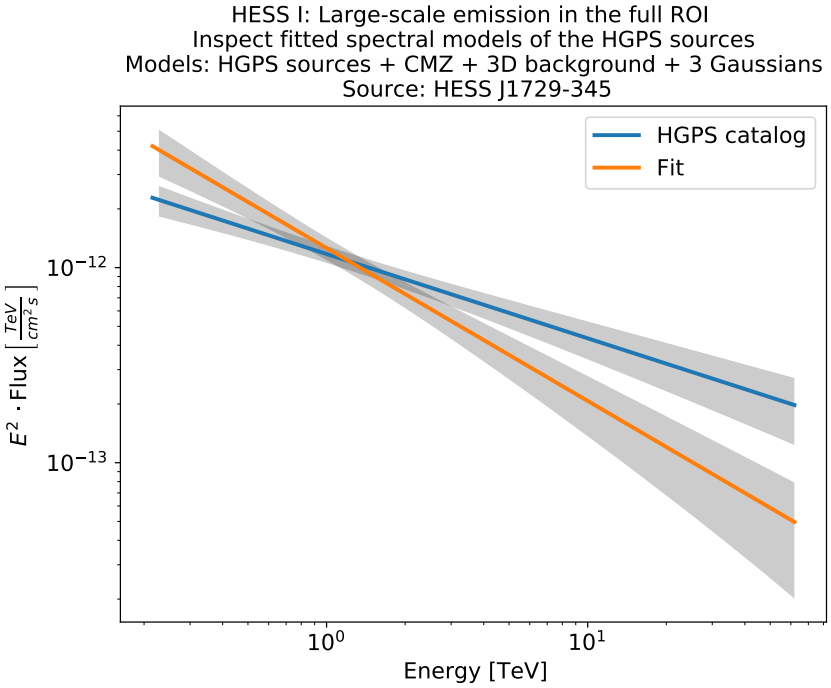

Figure 28: HESS I analysis of the full ROI: Fitted spectrum of *HESS J1729-345* after having added additional Gaussian spatial models.

The same holds for the other two HGPS sources where the spectral parameters have changed remarkably. The corresponding spectra are presented in figure B1 in appendix B.1.
Furthermore, the $\sqrt{TS}$ map for the whole ROI can be inspected. It is plotted in figure 29. It is directly visible that the map is smoother than without the added Gaussian spatial models as shown in figure 21, i.e. there seem to be no areas with remaining strong emission anymore. The fitted spectra of the three Gaussians are shown in figure 30. The best-fit values of the spectral parameters are additionally presented in these plots.

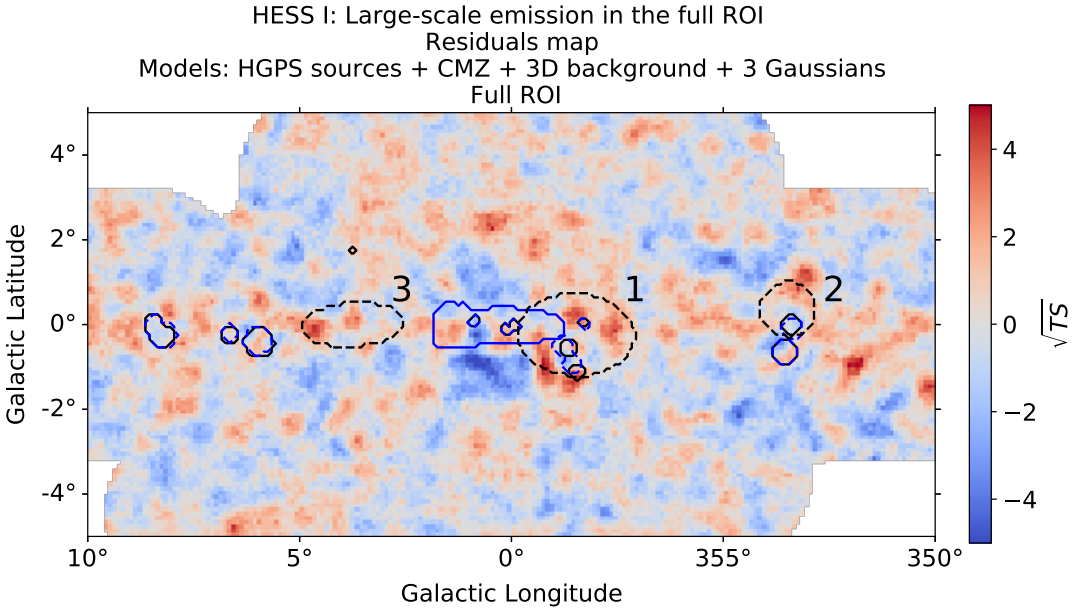

Figure 29: HESS I analysis of the full ROI: Residual significance map for the ROI used in this thesis with added Gaussian spatial models. The black dashed contours mark the $1\,\sigma$ regions of the Gaussian-shaped models that have been fitted to the data. Note that the remaining emission observed in regions 1 - 3 has clearly decreased compared to figure 21, the colour code is the same as in panel b) of the figure just referenced.

Figure 29 already indicates that the three additional models work well and are capable of describing the large-scale emissions properly. However, the fit quality can be analysed in a more quantitative way. One possibility to inspect how well the model describes the data is to calculate the squared residuals defined as

$$SR = \sum_i \frac{(\text{counts}_{\text{data,i}} - \text{counts}_{\text{model,i}})^2}{\text{counts}_{\text{model,i}}} \tag{30}$$

where i labels the spatial pixels of the data which have been summed over a certain energy range before. In general, the full energy range is taken into account when computing this quantity. The smaller the resulting value is, the better the data are described by the applied model. Similarly to chapter 5.7.2, the $1.5\,\sigma$ contours of the three different added Gaussian spatial models are used to calculate the SR value inside these areas. Note that for this purpose the best fit parameters for the Gaussian spatial models when all three regions were described at the same time have been used. The SR values calculated within the $1.5\,\sigma$ contour of the Gaussians and inside the whole ROI are shown in table 8 for the analysis where HGPS sources, CMZ and 3D background have been modelled and the case where the additional Gaussian spatial models are introduced. The SR values in presence of the added Gaussians are clearly below the ones without Gaussians, i.e. the additional models provide a good description of the large-scale emission regions.

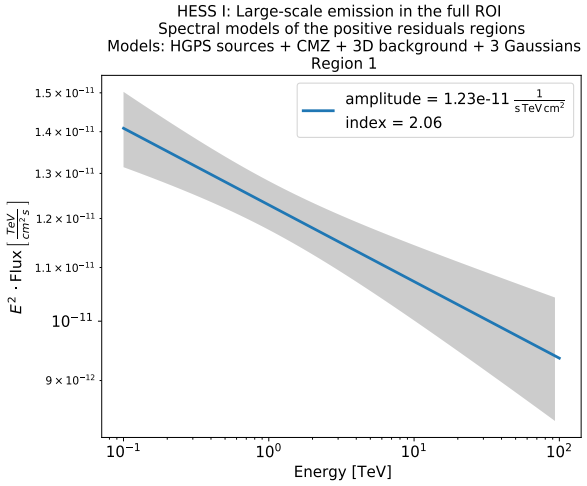

(a) Region 1

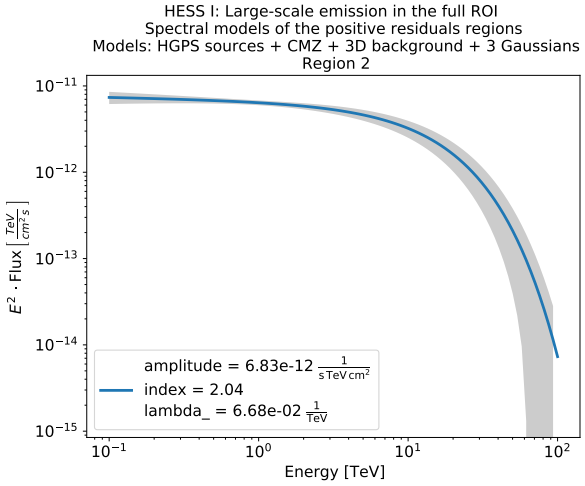

(b) Region 2

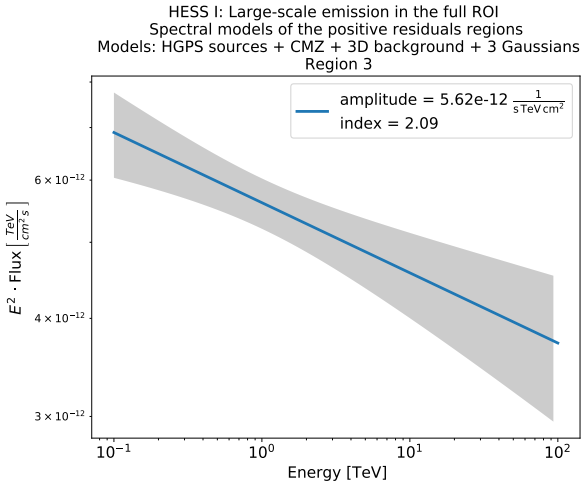

(c) Region 3

Figure 30: HESS I analysis of the full ROI: Best-fit spectra of the additional Gaussian models for the large-scale emission regions. The best-fit values without errors are printed in the legend.

7. Description of the diffuse emission regions via hydrogen templates (HESS I data)

7.1. Scientific motivation

The mechanisms leading to γ-ray emission have been already discussed in the previous chapters. In particular, the two leading processes are the decay of neutral pions π^0 that have been created by the collision of CRs with the ISM (hadronic model, chapter 2.1.2) and the IC scattering of low-energetic photons of the ISRF with CR electrons (leptonic model, chapter 2.1.1). Additionally, emission due to Bremsstrahlung of electrons in the electric field of ISM charged particles should be named here [70].
Since diffuse emission at GeV or even higher energies mostly arises from inelastic hadronic collisions followed by π^0 decay, for the analysis of diffuse emission in the course of this thesis, a π^0 template has been built [71], [14], [70]. Basically, the spatial distribution of diffuse emission via π^0 decay is closely related to the target material, i.e. hydrogen, distribution in the galaxy. The total amount of hydrogen within our galaxy consists of atomic (HI), molecular (H_2) and ionized (HII) hydrogen gas. The quantity of ionized hydrogen is negligible in comparison to atomic and molecular hydrogen [70].
The atomic hydrogen can be traced by the 21 cm emission line and the molecular hydrogen via the 2.6 mm CO emission line [70]. Hydrogen maps have been determined using public *GALPROP* [15] data [72]. *GALPROP* is a CR propagation code based on diffusion and convection processes [72]. More precisely, *GALPROP* v54 has been used (for more details on this specific version, see the manual [73]). The used *GALPROP* data are binned in various galactocentric rings; in particular, distances between 0 kpc and 50 kpc to the GC are separated into 17 distinct bins. Since the most inner part of the galaxy is already well described by the CMZ model and the *GALPROP* maps showed artefacts at galactocentric distances of more than 8 kpc (i.e. the distance to the sun), only eleven rings between 1.5 and 8 kpc are taken into acccount. An overview on the different rings can be found in table D1 in appendix D.1.
For this purpose, the *GALPROP* code has been fed by data from the *Leiden/Argentine/Bonn* (LAB) survey to calculate the map for atomic hydrogen [74]. This map represents the column density of HI, i.e. N_{HI} in cm-2. The molecular hydrogen map is built using data of the CO survey by *Dame, Hartmann & Thaddeus* (DHT) [75] and contains the integrated line intensity W_{CO} of CO in K km s-1. Additionally, a map containing the column density of both atomic and molecular hydrogen can be created via

$$N_H = N_{HI} + 2\,N_{H_2} = N_{HI} + 2\,X_{CO}\,W_{CO} \tag{31}$$

where the column density of molecular hydrogen N_{H_2} can be determined from its integrated line intensity W_{CO} and the conversion factor X_{CO} [70]. The conversion factor has been found to change with the galactocentric distance, i.e. it increases at growing distances to the GC due to the Galactic metallicity gradient [76]. Following the results shown in Fig. 25 of [77], the conversion factor has been chosen as a constant between 1.5 and 8 kpc galactocentric distance, in particular as $1.5 \cdot 10^{20}$ s / (cm^2 K km). Note that this approach assumes that the origin of the emission is hadronic. The purpose is now to figure out whether a hadronic scenario is likely for the large-scale emission regions or not.

[15] `https://galprop.stanford.edu/`

7.2. Data selection, datasets and background refitting per observation

Again, the same configuration as introduced in chapters 5.1 and 5.2 is used. The analysed stacked dataset is the same as achieved in chapter 6.2 after run-wise background refitting.

7.3. Applied models and fit results

HGPS sources, CMZ and 3D background are modelled as before. In contrast to the previous chapter 6 where three Gaussian spatial models have been fitted at the same time, for each region the Gaussian spatial model is replaced by a hydrogen `TemplateSpatialModel`. The remaining two regions are further described via Gaussians. Note that the spatial paramaters of the two remaining Gaussians are fixed, but the spectral ones are fitted. The same types of spectral models as before are assigned to the different regions, i.e. a power law spectral model for regions 1 and 3 and a power law with an exponential cutoff for region 2.
To produce the hydrogen templates for all regions, the best-fit Gaussian spatial models determined in chapter 6.3 and shown in table B1 are multiplied by the *GALPROP* hydrogen maps. After multiplication by the Gaussian spatial model, the hydrogen `TemplateSpatialModel` is normalised to units of sr-1. This is exemplary shown in figure 31. The same procedure has been repeated for all three regions, the molecular, atomic and full hydrogen maps as well as for all galactocentric rings. Finally,

$$n_{\text{total}} = n_{\text{regions}} \cdot n_{\text{rings}} \cdot n_{\text{hydrogen templates}} = 3 \cdot 11 \cdot 3 = 99 \tag{32}$$

hydrogen templates are created that are then fitted to the data.

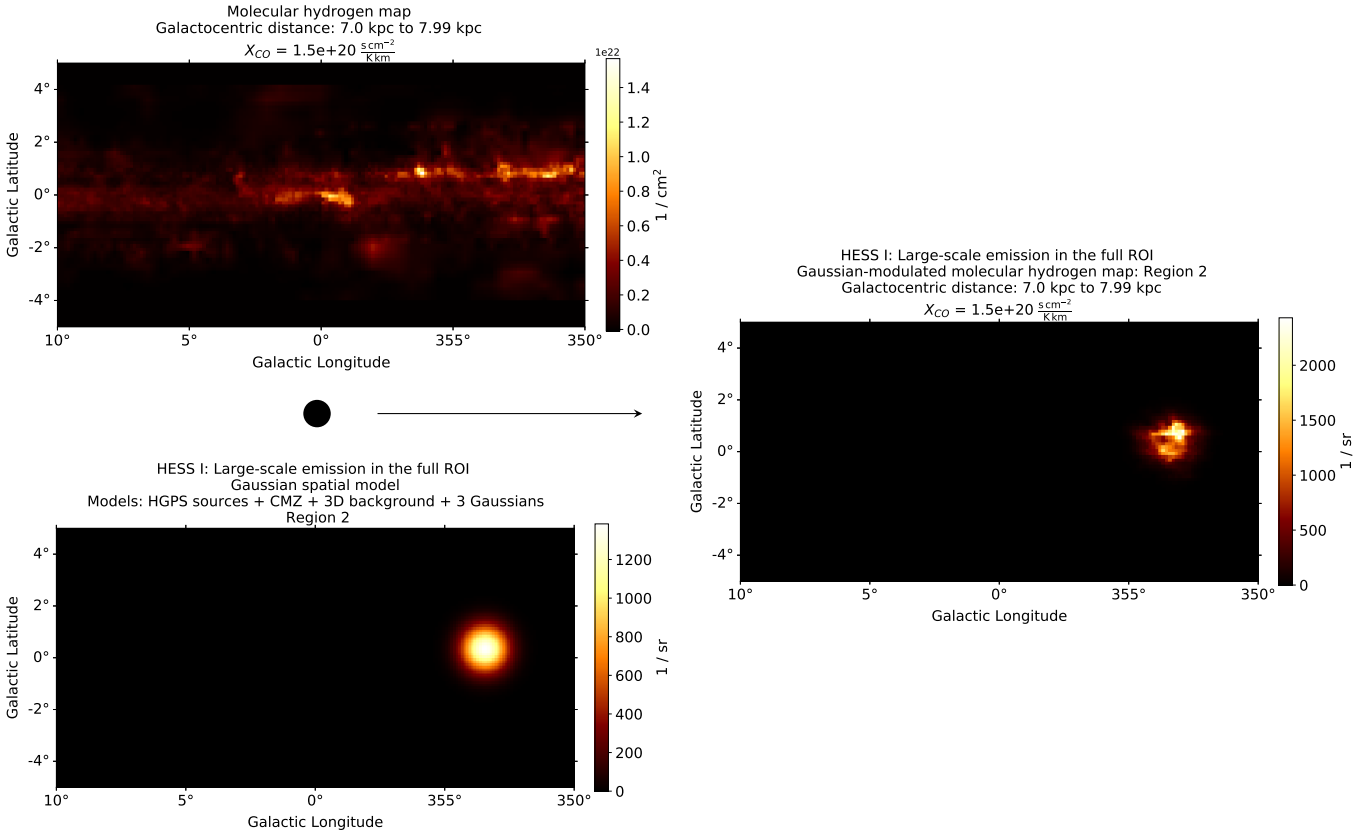

Figure 31: Derivation of the used hydrogen `TemplateSpatialModel` for region 2. In this example, the molecular hydrogen map between 7.00 and 7.99 kpc is multiplied by the best-fit Gaussian spatial model that has been found in chapter 6.3.

The procedure is briefly discussed using as an example the molecular hydrogen template for region 2 as derived in figure 31: For region 2, the Gaussian spatial template is replaced by the hydrogen template. The spectral model assigned to the hydrogen template is a power law with exponential cutoff as before. The regions 1 and 3 are further modelled by Gaussian templates (fixed spatial, but free spectral parameters) to check whether the applied hydrogen template describes the data better or worse than the Gaussian spatial model.
The objective is to find out which hydrogen template at which galactocentric distance describes the emission best for each region. As an indicator for the quality of the fit, the squared residuals introduced in equation (30) are taken into account. These are again calculated within the $1.5\,\sigma$ regions of the Gaussians as well as in the whole ROI. Afterwards, the best combination of hydrogen template and ring for each region is determined based on the lowest squared residuals value in the corresponding replaced region. The squared residuals of the best-working hydrogen templates for each region are added to table 8. Interestingly, the full hydrogen template for region 3 seems to perform best overall and for region 1. As additional material, the tables containing the squared residuals for each combination of regions, hydrogen templates and rings are available in a folder [16] of the GitHub repository. Furthermore, for each of the three emission regions, the full models, consisting of the HGPS sources, CMZ and 3D background models as well as the combination of Gaussians and hydrogen template as given in the left column of table 8 for the added hydrogen templates, describing the ROI are added to this folder.
Compared to the spectra in figure 30 where only Gaussians have been added to the models the spectra are only slightly changed, i.e. $\approx \pm 5\,\%$ for regions 1 and 3. For region 2, the best-fit values for index and cutoff are as well consistent, even though the amplitude shows larger deviations. The fitted spectra of the best performing hydrogen template for each region are shown in figure 32.
Three things should be noted here: The best description of the region that has been described by a hydrogen template does not necessarily result in the best description of the whole ROI. This underlines the coupling between the different models describing the large-scale emission regions at the same time. Furthermore, in case of region 3, multiple rings of the atomic and full hydrogen map showed a very similar performance (i.e. SR ≈ 475) providing a better description than the Gaussian for this region. The last remark is that for region 1, the atomic hydrogen for the ninth galactocentric ring performed slightly better than the tenth one (i.e. squared residuals of ≈ 1063 inside region 1), but the fitting revealed non-accurate fit statistics. Hence, it has not been chosen as the best description by a hydrogen template for region 1. A similar case occurred with region 3, too.
A visual comparison between the analysis with 3 Gaussian spatial templates (chapter 6) to the hydrogen template analysis is presented in the figures 34, 35 and 37 for the three regions separately. For each region, the workflow is demonstrated. In particular, on the left hand side, the residuals map for each region is shown after the analysis of the full ROI performed in chapter 5, i.e. the case where HGPS sources, the CMZ and 3D background have been fitted. In this step, the three large-scale emission regions have been found. Using this as a starting point, the large-scale emission regions were first modelled by Gaussian spatial models and proper spectral models. This is indicated via the lower branch on the right. The best-fit Gaussian spatial model and the resulting residuals map are presented. As a last step, molecular, atomic and combined hydrogen maps, that were modulated by the best-fit Gaussians, are chosen to model the different regions. The corresponding analysis chain is shown in the upper branch for the best working template for each region. The different regions are discussed in the following.

[16] https://github.com/fabian-richter/HESS_HAP_extended_emission_and_FB/tree/main/Modelling_of_the_full_ROI/HESS_I/hydrogen_analysis

Table 8: HESS I analysis of the full ROI: Squared residuals in the three large-scale emission regions and overall for the different analyses. The areas of the three regions are determined from the 1.5 σ containment regions of the fitted Gaussian spatial models from chapter 6. HGPS sources, CMZ and 3D background are modelled in all analyses and are not written in every row, but only the additional models are given. For the hydrogen templates, the best working type of hydrogen for each region as well as the galactocentric ring are given. Lowest squared residuals values are marked blue.

Added models	Ring	Region 1	Region 2	Region 3	Overall
-	-	1294.44	446.87	555.53	19329.5
3 Gaussians	-	1066.84	323.55	479.6	18925.3
2 Gaussians + at. hydro. reg. 1	10	1068.10	328.92	475.38	18912.20
2 Gaussians + mol. hydro. reg. 2	11	1060.19	312.28	474.80	18913.03
2 Gaussians + full hydro. reg. 3	6	1058.93	328.80	467.73	18910.84

Region 1

For region 1, the atomic hydrogen template in the tenth galactocentric ring performed best based on the squared residuals. In figure 34, the analysis chain is shown. At negative latitudes, i.e. right next to the GC in the shown map, there is only a faint excess (compared to other spots along the GP) visible in the atomic hydrogen template (figure 33) covering the full ROI at the corresponding distance.
Moreover, the spot's extension is smaller than the observed emission. Comparing the Gaussian template and the hydrogen template, the same is observed, in particular, the bright core of the hydrogen template is smaller than for the Gaussian. Together with the vanishing atomic hydrogen column density close to the GC this might be the reason why the Gaussian template describes this region better than the hydrogen map, even though the difference is very small and both final residuals maps on the right are non-distinguishable by eye. Finally, it is rather unlikely that the emission observed in the first region is connected to the atomic hydrogen population in this region, since the spacial morphology of hydrogen column density and emission reveal no clear coincidence. A similar conclusion was made in [67]. In addition, *SNR G359.1-0.5* is estimated to be located at a galactocentric distance of $\approx$ 4 kpc. Based on the results presented here, i.e. the best working hydrogen ring has a distance of $\approx$ 6.5 kpc - 7.0 kpc to the GC, makes it appear implausible that *SNR G359.1-0.5* is correlated to the observed emission when assuming hadronic origin of the observed γ-ray excess.
Neither the Gaussian models nor the hydrogen templates achieved a clear insight to the connection of this region to the *Fermi* Bubbles. Even after having modelled the three large-scale emission regions, the residual significance map presented in figure 29 does not show a clear excess in the vicinity of the *Fermi* Bubbles. It is remarkable that the region is better described with a power law spectral model without a cutoff than for a model with cutoff. This result is in tension with previous *Fermi*-LAT observations as presented in chapter 2.

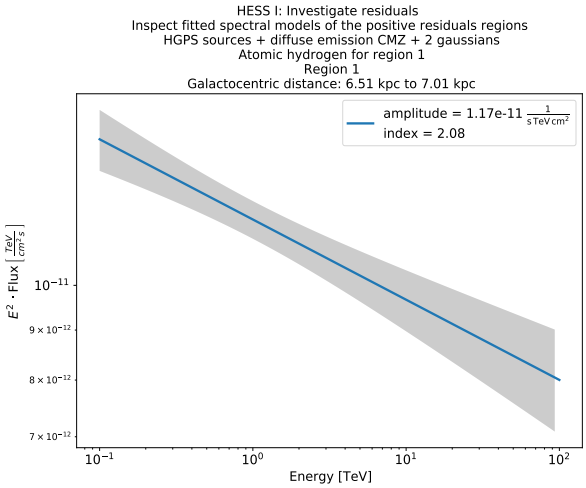

(a) Region 1

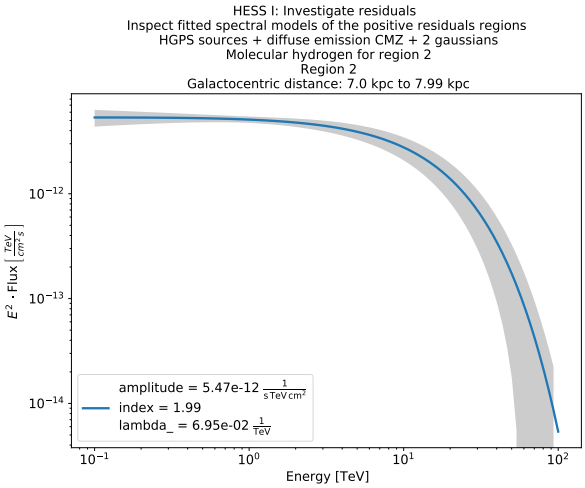

(b) Region 2

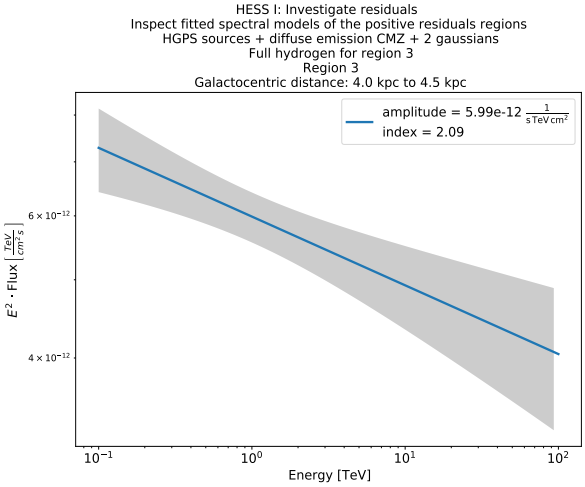

(c) Region 3

Figure 32: HESS I analysis of the full ROI: Best-fit spectra of the additional hydrogen spatial models for the large-scale emission regions. The best-fit values without errors are printed in the legend.

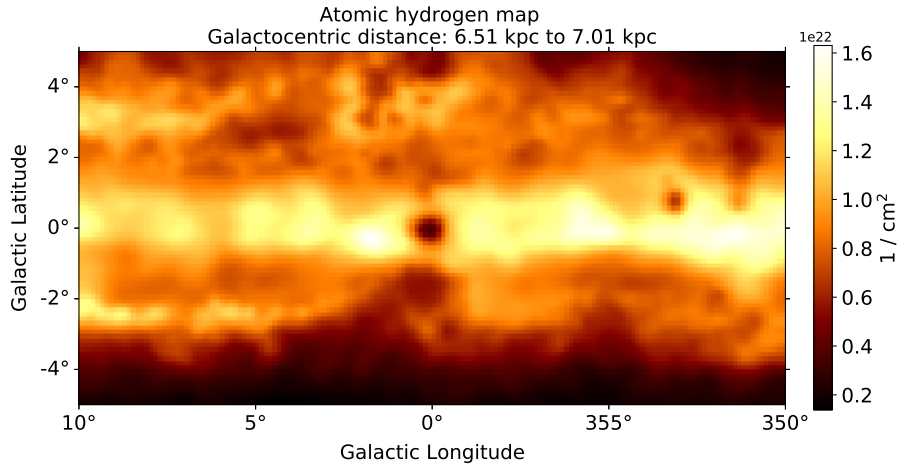

Figure 33: Atomic hydrogen map in the full ROI for a galactocentric distance of ≈ 6.5 kpc - 7.0 kpc.

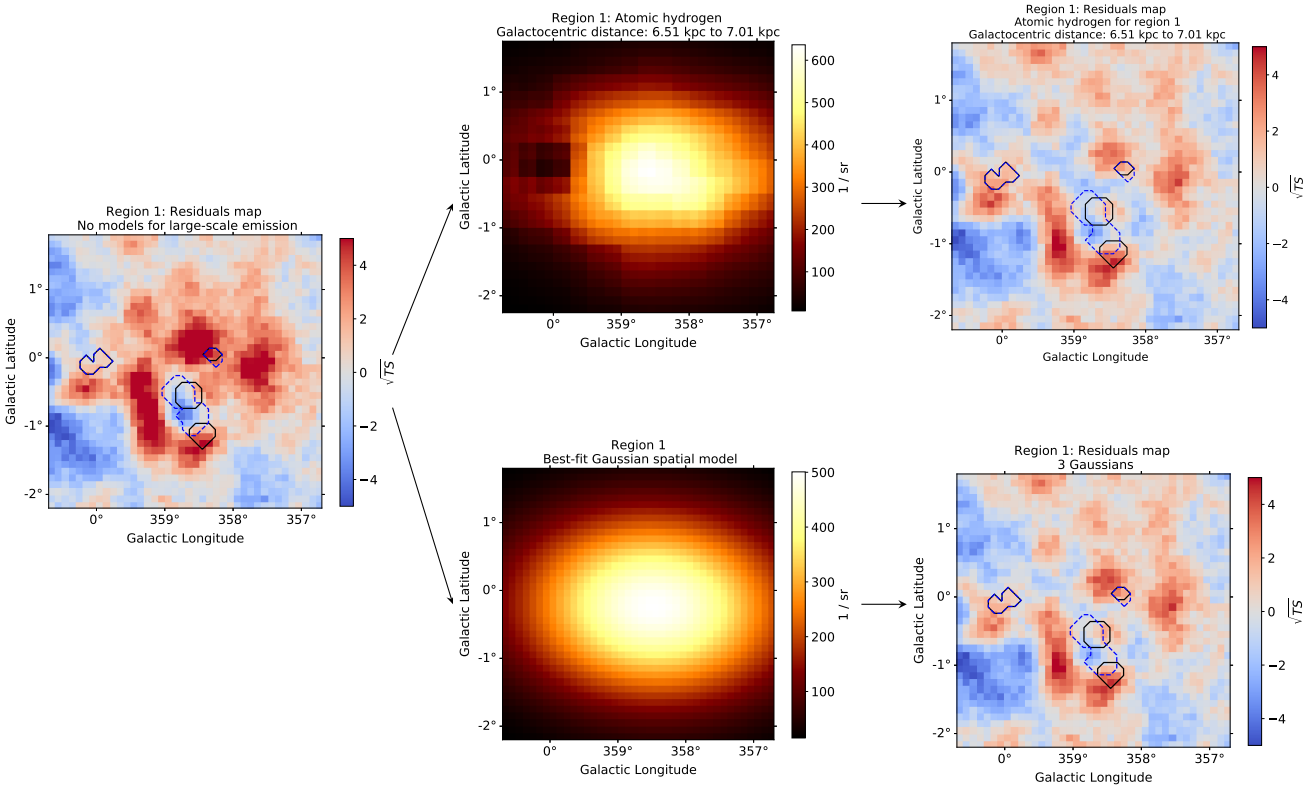

Figure 34: HESS I analysis of the full ROI: Region 1: Comparison of the description of the large-scale residuals using Gaussian spatial models to the analysis performed with hydrogen templates.

Region 2

Molecular hydrogen at a galactocentric distance of ≈ 7.0 kpc - 8.0 kpc achieved the best result for region 2 in the performed analysis. Having a look at figure 35, the modulated molecular hydrogen map reveals a bright spot on the top right that coincides with the high reddish residuals visible in the residuals map on the left. This spot can be also directly seen in the molecular hydrogen map covering the full ROI at the corresponding distance in figure 31 in the top left part. This may also be the reason why the region above the two HGPS sources *HESS J1729-345* and *HESS J1731-347* is less reddish in the map after description with the hydrogen template than with the Gaussian. The spatial coincidence of the hydrogen template and the observed emission makes an hadronic origin of the emission plausible.
However, it is difficult to figure out possible CR accelerators that can illuminate the molecular hydrogen in this region. The best-fit distance has been found to be ≈ 7.0 kpc - 8.0 kpc in this thesis while in [69] a lower boundary of 3.2 kpc on the galactocentric distance of *HESS J1731-347* is given. Additionally, it is mentioned that the actual distance is expected not to be far above this limit. Thus, *HESS J1731-347* can be excluded as a candidate that illuminates the nearby molecular clouds and leads to the observed emission. No further possible candidates in the vicinity of the second region are known.

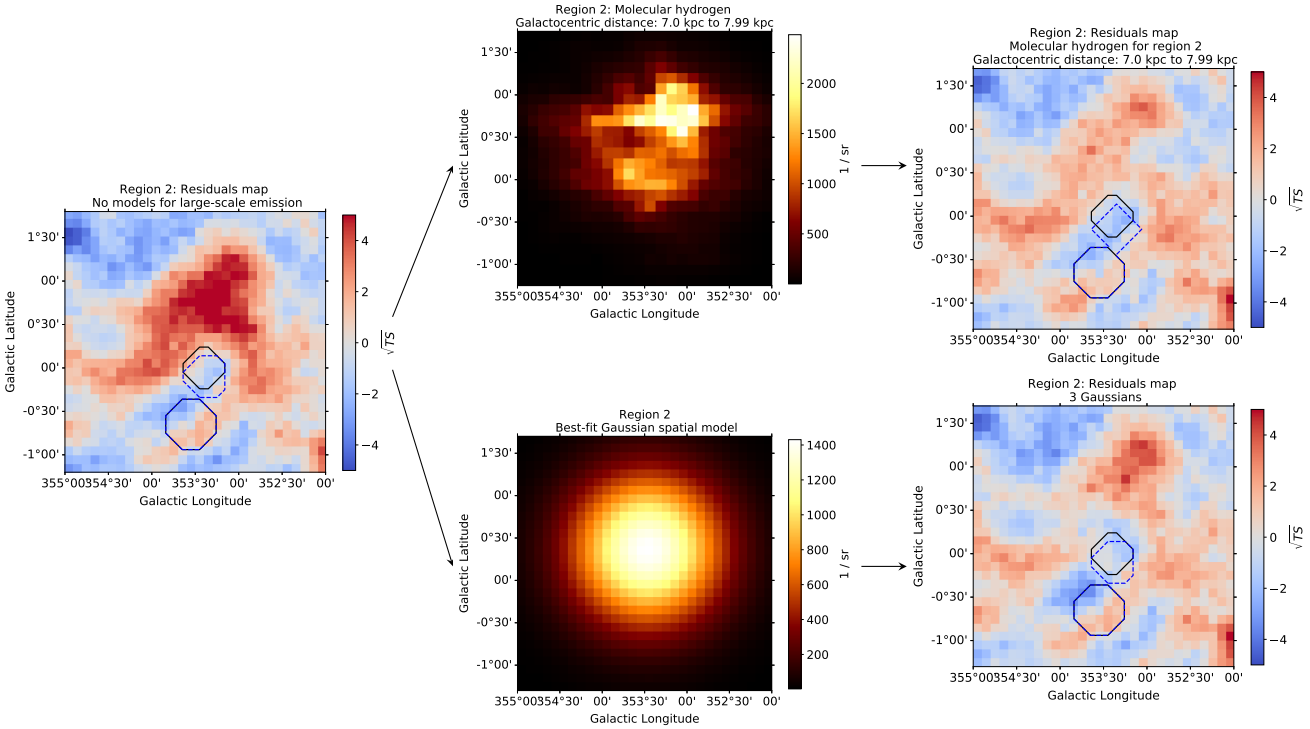

Figure 35: HESS I analysis of the full ROI: Region 2: Comparison of the description of the large-scale residuals using Gaussian spatial models to the analysis performed with hydrogen templates.

Region 3

In case of the third region, the full hydrogen map at a distance of ≈ 4.0 kpc - 4.5 kpc showed best performance based on the squared residuals. The map covering the full ROI is shown in figure 36. It does not reveal any enormous column density in the GP at the position of the observed residuals.

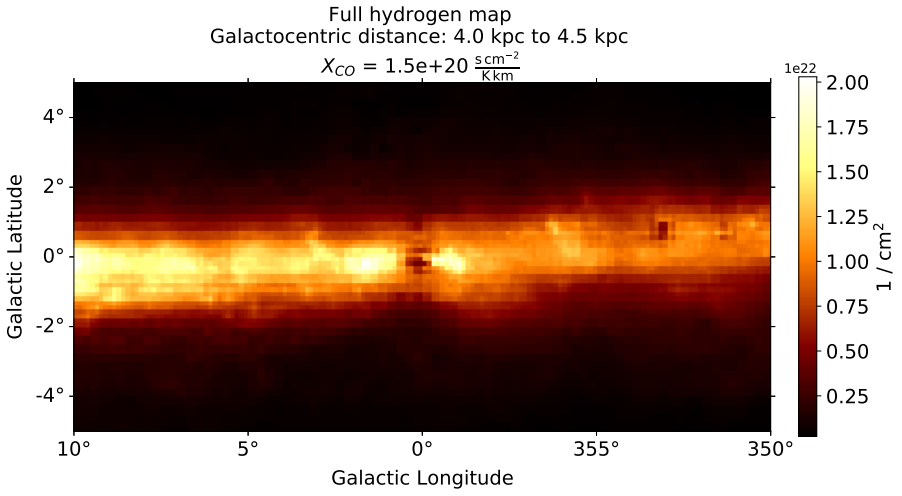

Figure 36: Full hydrogen map in the full ROI for a galactocentric distance of ≈ 4. kpc - 4.5 kpc.

By taking a look at figure 37, the morphology of the Gaussian modulated full hydrogen map furthermore clearly resembles the Gaussian best-fit template indicating that there is no remarkable structure in the hydrogen map itself. As mentioned above there were various (full and atomic)

hydrogen templates at different galactocentric rings showing a similar performance. However, all of them show a relatively low hydrogen density in the vicinity of region 3, i.e. there was no full hydrogen template with a spatial structure coincident with the observed emission. This makes it very unlikely that the detected large-scale residuals of region 3 are correlated to hadronic emission. In addition, in this region no promising CR accelerators, that could possibly illuminate surrounding molecular clouds, are known.
Interestingly, when having a look at the atomic hydrogen map in figure 33 one observes a bilobular-shaped increased hydrogen density that may be coincident with the emission in region 3. However, fitting this template ended up in comparable, but slightly worse results than the modulated full hydrogen map.

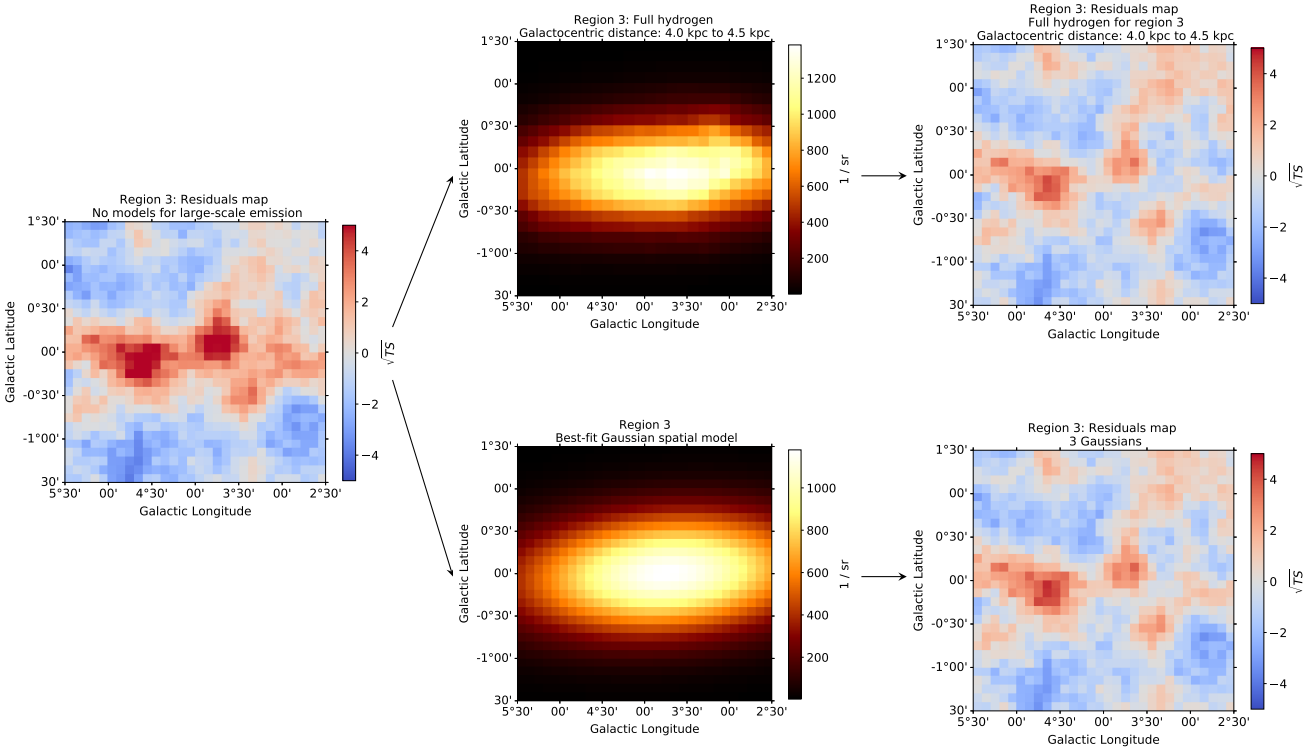

Figure 37: HESS I analysis of the full ROI: Region 3: Comparison of the description of the large-scale residuals using Gaussian spatial models to the analysis performed with hydrogen templates.

8. *Fermi* Bubbles template analysis with HAP 3D background model

In this section, the template analysis of the *Fermi* Bubbles using only the HAP 3D background model is presented. Briefly summarised, in contrast to the previous analyses HGPS sources, CMZ and a $\pm 0.3°$ stripe along the GP are completely masked during the whole analysis. Only the signal inside the *Fermi* Bubbles ROI (defined as in figure 4) is evaluated in the beginning. The exact procedure will be explained in more detail later.
The main part of the *Fermi* Bubbles analysis is performed using HESS Iu data. This era of data taking has been chosen since the HESS Iu IGS runs are mostly pointing to regions in close vicinity of the *Fermi* Bubbles (as expected from *Fermi*-LAT data). Most of the available HESS I and II runs are pointing directly to the GC. In addition, HESS I observations cover areas along the GP. The exposure maps of the stacked datasets in the full ROI are shown in the appendix in figure G1 for the different H.E.S.S. eras. For HESS II, the total exposure in the full ROI is furthermore rather low, i.e. there are only ≈ 250 HESS II runs compared to ≈ 900 and ≈ 700 runs for HESS I and HESS Iu, respectively. A further reason for choosing HESS Iu for the main analysis is that the connection between the *Fermi* Bubbles and the large-scale emission detected in region 1 with HESS I data remains unclear (see e.g. chapter 5).
Thus, HESS I and II data are used separately to check the results achieved from HESS Iu data. In a last analysis, HESS I, II and Iu data are evaluated at the same time performing a stacked fit of these three eras. Note that additional plots and the spectral data achieved in the *Fermi* Bubbles template analysis can be found in the folder [17] of the GitHub repository.

8.1. Data selection

Data in the same ROI as before are analysed. The analyses have been performed for both, std ImPACT and std zeta algorithm. Furthermore, the analysis is performed with Gammapy v0.19. This results in the following summary:

- H.E.S.S. eras: HESS I, II and Iu
- ROI: $\pm 10°$ in gal. longitude, $\pm 5°$ in gal. latitude
- Analysis chain: HAP, version hap-18-pl05, tables version Prod05
- std ImPACT and std zeta
- Background model version (std ImPACT): hess_bkg_3d_v07c_fov_radec
- Background model version (std zeta): hess_bkg_3d_v06c_fov_radec (HESS Iu)
- Background model version (std zeta): hess_bkg_3d_v05c_fov_radec (HESS I, II)
- Analysis software: Gammapy v0.19

The quality cuts on these data are the same as presented in chapter 5.1.

8.2. Datasets

The geometry of the datasets is chosen in the same way as in chapter 5.2. The same energy thresholds, i.e. $E_{\mathrm{thr}}^{\mathrm{bias}}$ and $E_{\mathrm{thr}}^{\mathrm{bkg}}$ are applied. The only difference is that additionally all energies below 0.3162 TeV (HESS Iu, II) and 0.3651 TeV (HESS I) have been cut away to avoid large

[17] `https://github.com/fabian-richter/HESS_HAP_extended_emission_and_FB/tree/main/FB_template_analysis`

systematic effects that have been observed at energies lower than that, but above the determined thresholds. An overview on the number of runs in the ROI as well as energy mean thresholds is given in table 9.

HESS era	std ImPACT		std zeta	
	# of runs	mean thresh. in TeV	# of runs	mean thresh. in TeV
HESS I	884	0.42 ± 0.11	915	0.55 ± 0.14
HESS II	251	0.40 ± 0.15	254	0.57 ± 0.13
HESS Iu	676	0.34 ± 0.08	675	0.43 ± 0.12

Table 9: *Fermi* Bubbles template analysis: Overview over the different available runs and energy thresholds for the different H.E.S.S. eras.

8.3. Background refitting per observation

HGPS sources, CMZ and a $\pm 0.3°$ stripe along the GP are completely masked in the course of this analysis, i.e. using the `mask_safe`. The *Fermi*-LAT *Fermi* Bubbles template is masked from background refitting, but not ignored (`mask_fit`). The corresponding mask is shown in figure 38. The results for the re-fitted 3D background models parameters are printed in table 10.

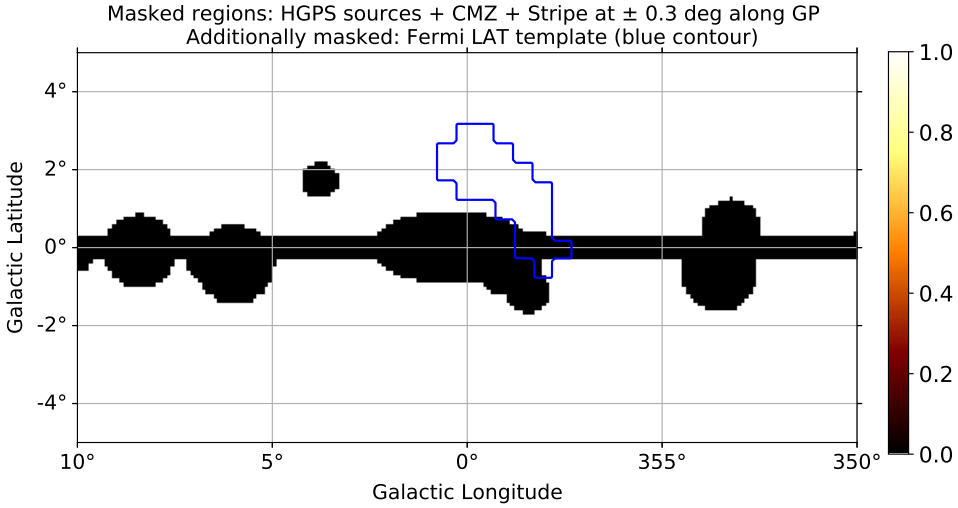

Figure 38: Exclusion mask used for the *Fermi* Bubbles template analysis. The black regions in this mask are completely ignored during the whole analysis (`mask_safe`). The *Fermi*-LAT *Fermi* Bubbles template is indicated via the blue contour. It is masked from background refitting, but not from the complete analysis (`mask_fit`).

8.4. Determination of the spectra

After the datasets of the single observations have been stacked together to one dataset, the overall background of this stacked dataset is again refitted under consideration of the same mask as in figure 38. For all stacked datasets, the refitted norm is close to 1 and the tilt close to 0. Afterwards, the intensity inside the *Fermi* Bubbles ROI is calculated for each energy bin α via

HESS era	std ImPACT		std zeta	
	bkg norm	bkg tilt	bkg norm	bkg tilt
HESS I	0.94 ± 0.10	0.06 ± 0.12	0.98 ± 0.11	0.02 ± 0.11
HESS II	0.97 ± 0.11	0.01 ± 0.11	0.96 ± 0.11	0.01 ± 0.11
HESS Iu	0.92 ± 0.11	0.03 ± 0.09	0.96 ± 0.11	0.02 ± 0.08

Table 10: *Fermi* Bubbles template analysis: Mean values and standard deviation of the distributions of the best-fit parameters achieved with the run-wise background refitting of the single observations. Results for the different HESS eras as well as std ImPACT and std zeta are shown.

$$I(E_\alpha) = \frac{1}{\Delta E_\alpha \cdot \Delta\Omega_{FB}} \sum_{i \in FB} \frac{\text{counts}_{\text{i},\alpha} - \text{bkg}_{\text{i},\alpha}}{\text{exposure}_{\text{i},\alpha}}. \tag{33}$$

ΔE_α is the width of the corresponding energy bin and $\Delta\Omega_{FB}$ is the area of the *Fermi* Bubbles ROI in units of sr. Note that $\Delta\Omega_{FB}$ is not the solid angle of the total *Fermi* Bubbles template, but just its part contributing in the analysis; since the masks around the GP and CMZ partially overlap with the *Fermi* Bubbles template, not all parts of the template contribute to the analysis. See table 24 for the solid angle of the effectively contributing *Fermi* Bubbles template. In each energy bin, the background predicted by the 3D background model is subtracted from the detected counts for each spatial pixel inside the *Fermi* Bubbles ROI. This difference is then divided by the exposure in the corresponding pixel and summed over all spatial pixels.
Note that the binning of the used datasets themselves is chosen to be 16 bins per decade, i.e. 48 bins in total. The full fitting procedure has been performed with this geometry. Before the evaluation of the intensity according to equation (33), counts, expected background counts and exposure are added for three neighbouring bins to increase statistics of the bins. ΔE_α is consequently defined as the difference of the upper and lower edge of the new energy bins. Since bins below the energy threshold are not taken into account for the spectra, the final spectra have 13 energy bins.

8.5. HESS Iu analysis results

The analysis of HESS Iu data marks the main part of this chapter. In a first step, the residuals maps are investigated and after that the spectra. Furthermore, an additional *Fermi* Bubbles template is defined based on the HESS Iu residuals achieved in the std ImPACT analysis and used for a cross-check. Different studies on background systematics are performed and presented in the end of this chapter. Furthermore, a comparison with PA data is done.

8.5.1. Residuals maps and first spectra

As the first step, the obtained residuals maps after background refitting of the stacked dataset are inspected. These maps are shown in table 11. The left column shows the results achieved using the std ImPACT, the right column using the std zeta analysis. The top row shows the residuals summed over all energies, the bottom row the residuals summed between 1 and 10 TeV. In the top row, the contour of the *Fermi*-LAT template is added.
The residual significance maps reveal that emission in this expected *Fermi* Bubbles ROI is observed. The structure of the emission is very similar for std ImPACT and std zeta, even though the region appears slightly more reddish and extended in std zeta analysis. Furthermore, within the *Fermi* Bubbles ROI, the morphology of the emission between 1 and 10 TeV looks

very similar to the one that has been found by summing over all energies. Note that it was not possible to directly fit a model to the excess that may be coincident with the *Fermi* Bubbles emission. A cross-check of the *Fermi* Bubbles template analysis of HESS Iu data, where HGPS sources, CMZ and the GP are not completely masked and the excess in vicinity of the *Fermi* Bubbles ROI has been modelled, is presented in chapter 9.

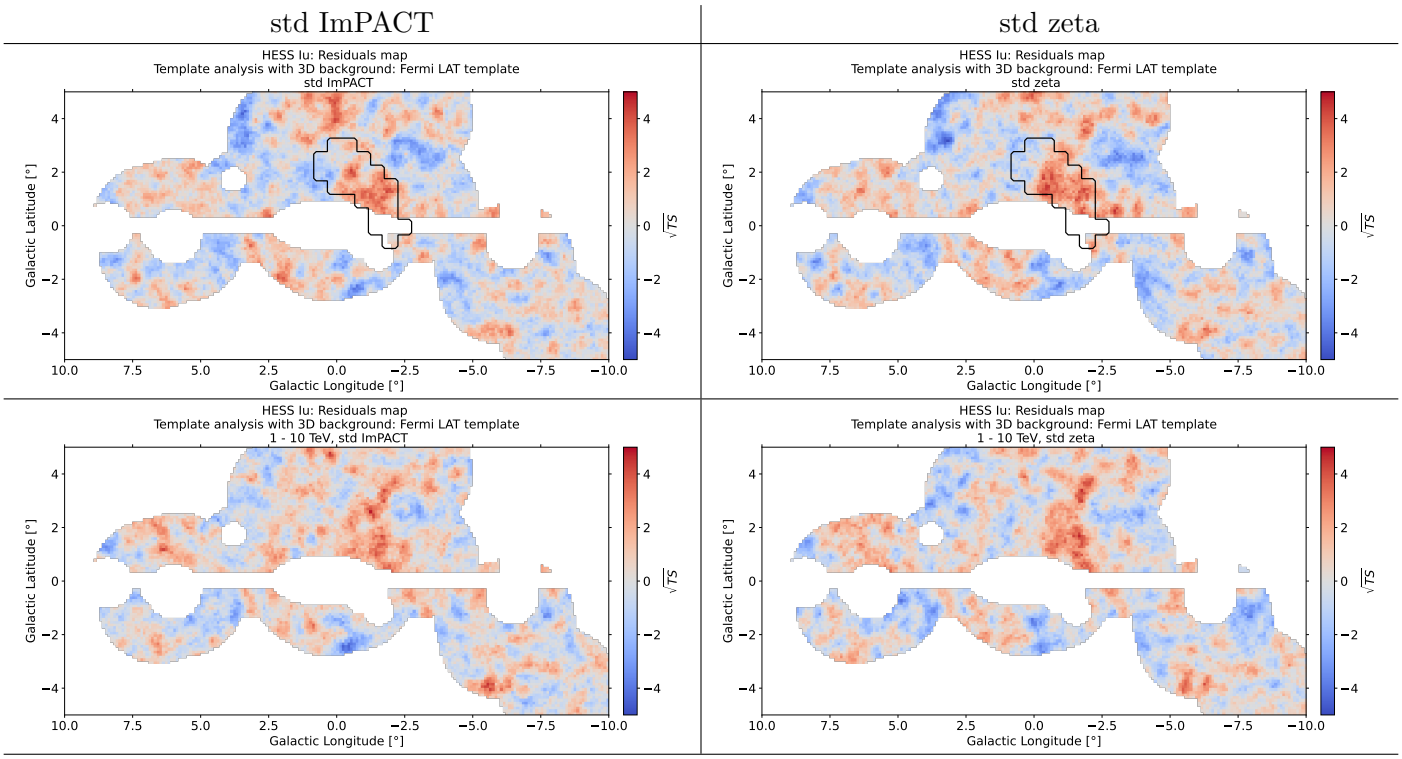

Table 11: *Fermi* Bubbles template analysis using HESS Iu data: Residual significance maps for the *Fermi* Bubbles template analysis performed with the *Fermi*-LAT template and both std ImPACT and std zeta. Top row: Maps summed over all energies. Bottom row: Maps summed over energies between 1 and 10 TeV.

In a next step, the differential flux in energy bin α inside the *Fermi* Bubbles ROI is computed according to

$$F(E_\alpha) = E_\alpha^2 \cdot I(E_\alpha) \tag{34}$$

where $I(E_\alpha)$ is the intensity per energy bin given in equation (33) and E_α is the mean logarithmic energy of bin α. The combined results for std ImPACT and std zeta are presented in figure 39. In all differential flux plots in this thesis, the shown errorbars and upper limits are with respect to statistical errors assuming a Poisson distribution of the detected counts. The following conventions are met to decide whether errorbars or upper limits are plotted:

- $F(E_\alpha) > 2\,\sigma_{stat}(E_\alpha)$: Errorbar around $F(E_\alpha)$ with length $\pm 1\,\sigma_{stat}(E_\alpha)$
- $F(E_\alpha) < 2\,\sigma_{stat}(E_\alpha)$ & $F(E_\alpha) > 0$ TeV cm $-$ 2 s $-$ 1 sr $-$ 1:
  Upper limit at $F(E_\alpha) + 2\,\sigma_{stat}(E_\alpha)$ with length $1\,\sigma_{stat}(E_\alpha)$
- $F(E_\alpha) < 2\,\sigma_{stat}(E_\alpha)$ & $F(E_\alpha) < 0$ TeV cm $-$ 2 s $-$ 1 sr $-$ 1:
  Upper limit at $2\,\sigma_{stat}(E_\alpha)$ with length $1\,\sigma_{stat}(E_\alpha)$

Coming back to the spectra shown in figure 39, one sees that std ImPACT and std zeta analysis are consistent for most of the energy bins. Especially, both spectra reveal significant points (i.e.

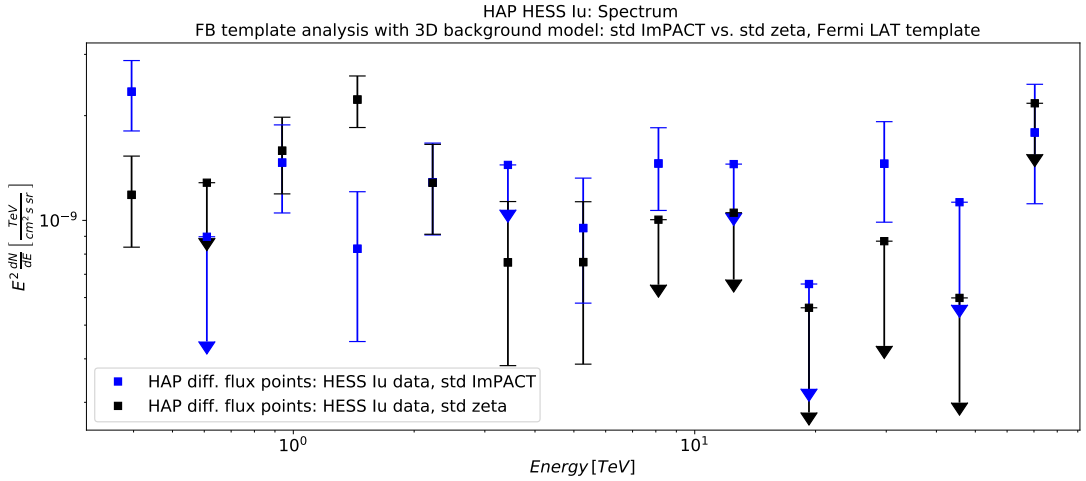

Figure 39: *Fermi* Bubbles template analysis using HESS Iu data: Spectra for std ImPACT and std zeta analysis using the *Fermi*-LAT FB template

$F(E_\alpha) > 2\,\sigma_{stat}(E_\alpha)$) at energies between 1 and 10 TeV. This is very interesting since a signal from the *Fermi* Bubbles may be detected well above the energy limit of *Fermi*-LAT.

8.5.2. Definition of a HESS Iu data based *Fermi* Bubbles template

The possible signal at energies between 1 and 10 TeV as well as the observed excess in the residual significance maps in this energy range shown in table 11 motivate to define an additional *Fermi* Bubbles template. The idea is to have a different template to cross-check the results assuming the *Fermi*-LAT template.
As a starting point to define an alternative template, the residual significance map in the bottom left panel, showing the results from std ImPACT analysis between 1 and 10 TeV, of table 11 is used. In a further step, this map is slightly smoothed with a Gaussian kernel of width 0.1° to achieve a template with smooth boundaries. Afterwards, a threshold of $\sqrt{TS} > 1.5$ in the vicinity of the *Fermi* Bubbles (as expected from *Fermi*-LAT observations) is applied to the data. Small holes inside the resulting region are filled to obtain a closed template. The template defined in this way is presented in figure 40. Its solid angle amounts to $\Delta\Omega_{FB,HESS\,Iu} = 1.2 \cdot 10^{-3}$ sr, i.e. ≈ 60 % of the *Fermi*-LAT *Fermi* Bubbles template. It will be referred to as HESS Iu template in the following.
As a cross-check of the analysis, the spectra achieved using the *Fermi*-LAT and HESS Iu templates are compared in figure 41. It is important to note that in the analyses performed with the HESS Iu template, in the whole analysis chain this template is applied, i.e. the HESS Iu *Fermi* Bubbles template is masked during the background refitting per run and of the stacked dataset instead of the *Fermi*-LAT template.
Comparing the blue and black differential flux points, one observes that they are consistent for both analysis chains. However, the plots reveal that flux points are a bit higher for the HESS Iu template at energies between 1 and 10 TeV. Since the HESS Iu template has been defined based on the residuals in this energy-range, this is reasonable. At low and high energies the results are consistent within the statistical uncertainties.

8.5.3. Uncertainty studies

In this chapter, different studies are performed to estimate systematic and statistic uncertainties of the analysis. In the following, only part of the results are shown, i.e. not all combinations

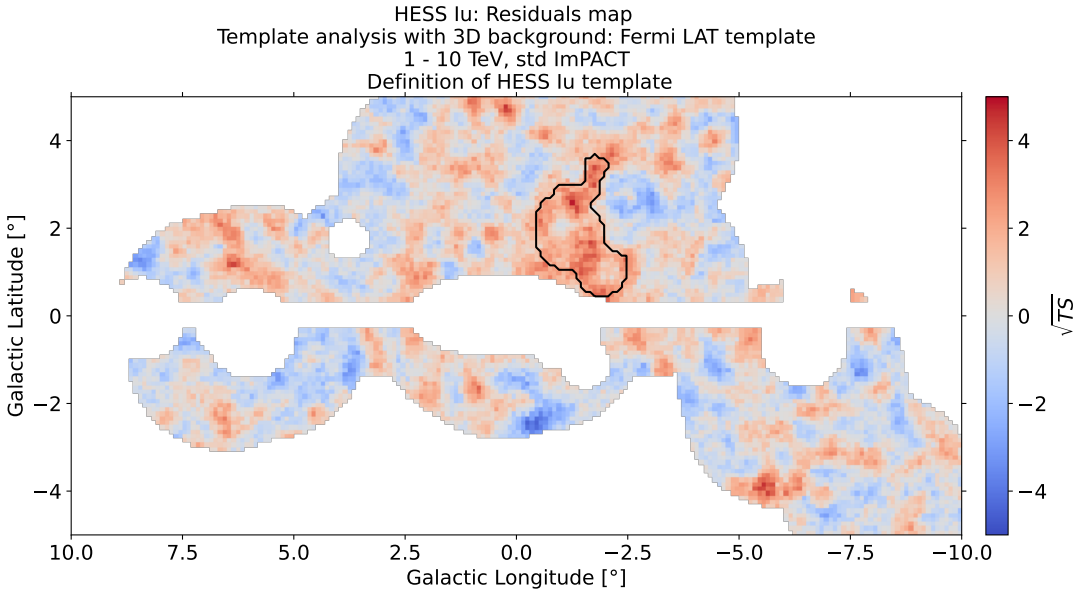

Figure 40: *Fermi* Bubbles template analysis using HESS Iu data: Definition of a HESS Iu residuals based template; residual significance map achieved using the *Fermi*-LAT *Fermi* Bubbles template with the contour of the HESS Iu template. The solid angle of this ROI is $\Delta\Omega_{FB,HESS\,Iu} = 1.2 \cdot 10^{-3}$ sr.

of reconstruction algorithms (std ImPACT and std zeta) and *Fermi* Bubbles templates. Thus, an additional folder [18] for the uncertainty studies using HESS Iu data is set up in the GitHub repository.

8.5.3.1. Fractional residuals between 1 and 10 TeV: *Fermi* Bubbles ROI vs. outside region

As a first step, fractional residuals inside and outside the *Fermi* Bubbles ROI are calculated for energies between 1 and 10 TeV. The idea is to compare a region where no *Fermi* Bubbles signal is expected to the region where it is. For consistency, a region with high exposure (i.e. a region with an exposure that is similar or larger than the exposure inside the *Fermi* Bubbles ROI) around the *Fermi* Bubbles ROI has been selected as outer region (see figure G1 c) in appendix G for the HESS Iu exposure map). The fractional residuals are then computed inside and outside the *Fermi* Bubbles ROI following equation (27) where $\text{counts}_{\text{model}}$ are the predicted background counts in this case. As a next step, the distributions of fractional residuals for all pixels in the region inside and outside of the *Fermi* Bubbles ROI are compared. The statistical significance of the difference of the mean values of the two distributions is estimated via equation (28). The results of this analysis for the std ImPACT analysis are shown in table 12.
Having a look at the smoothed maps, one observes a signal in the region of the expected *Fermi* Bubbles. The same feature is found more quantitatively in the fractional residuals distributions. The blue distributions are more narrow and shifted to positive values compared to the red ones. The statistical significance in case of the *Fermi*-LAT template is computed to be $\approx 3.6\,\sigma$ and $\approx 7.6\,\sigma$ for the HESS Iu template. This is again expected since the HESS Iu template is tuned with respect to the analysis. The corresponding plots achieved with the std zeta analysis chain are shown in appendix E.1 figure E1 a) and b). These distributions reveal a higher significance

[18] `https://github.com/fabian-richter/HESS_HAP_extended_emission_and_FB/tree/main/FB_template_analysis/HESS_Iu/uncertainty_estimation_plots`

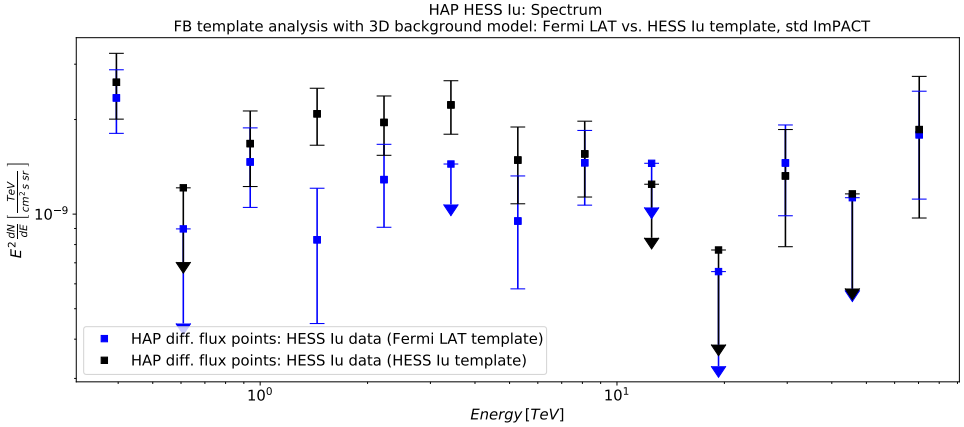

(a) std ImPACT analysis

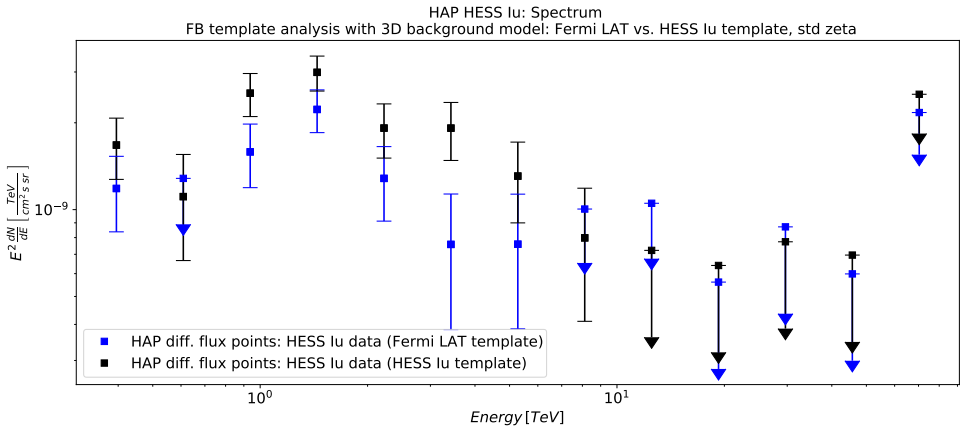

(b) std zeta analysis

Figure 41: *Fermi* Bubbles template analysis using HESS Iu data: Spectra for std ImPACT and std zeta analysis: Comparison of the results from *Fermi*-LAT to the ones from HESS Iu *Fermi* Bubbles template.

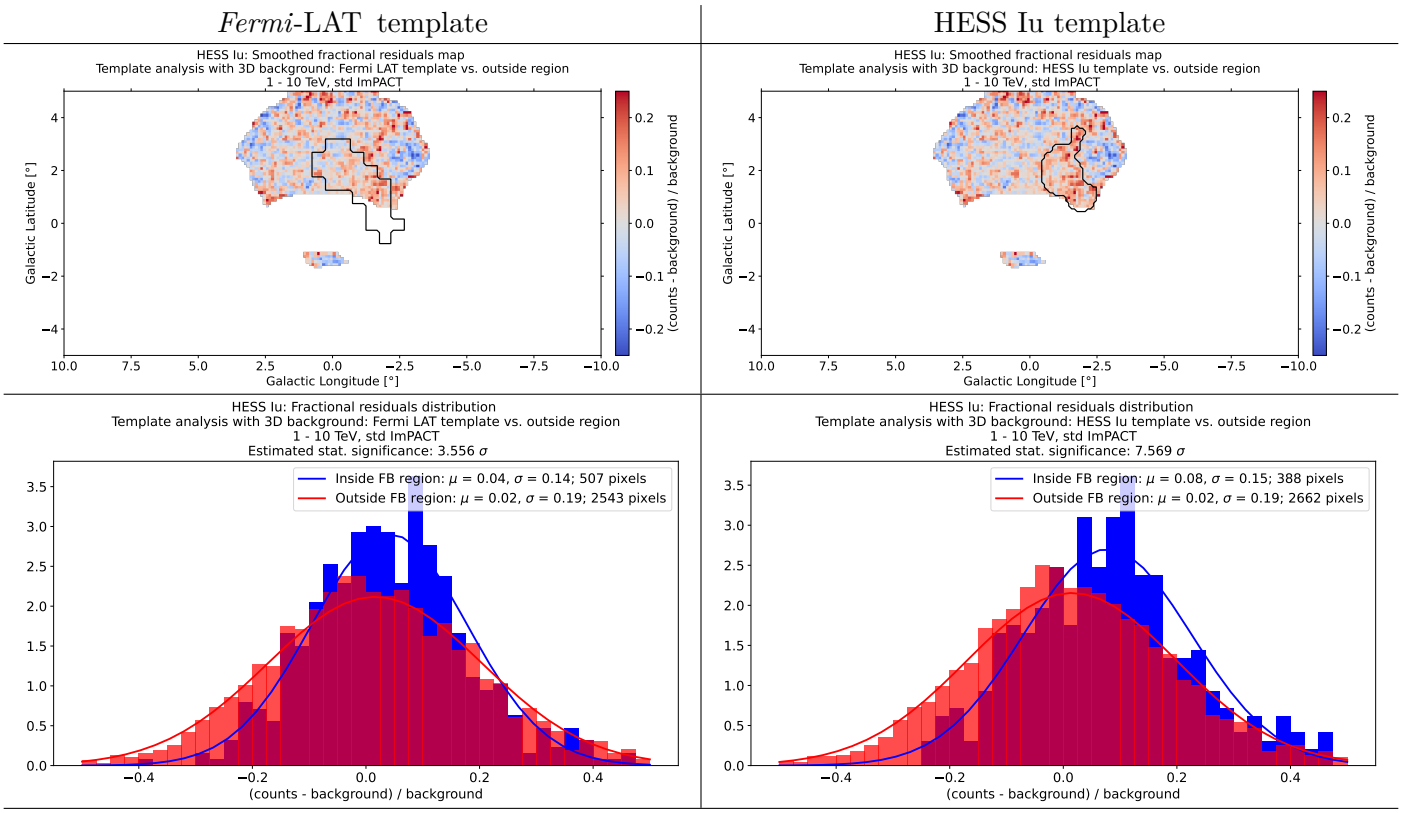

Table 12: *Fermi* Bubbles template analysis using HESS Iu data: Fractional residuals for std ImPACT between 1 and 10 TeV inside the *Fermi* Bubbles ROI and outside, i.e. in a region with exposure that is comparable to the one inside the *Fermi* Bubbles ROI. Upper panels show the smoothed fractional residuals maps. A Gaussian kernel with 0.06° width is chosen for smoothening. In the lower panels the distributions of the non smoothed fractional residuals are presented. The left panels are for the analysis performed with the *Fermi*-LAT template, the right ones for the HESS Iu template.

compared to std ImPACT analysis. This is consistent with the stronger reddish residuals in the *Fermi* Bubbles ROI observed in the right panels of table 11 compared to the left panels.

8.5.3.2. Fractional residuals between 1 and 10 TeV: *Fermi* Bubbles ROI vs. reflected *Fermi* Bubbles ROI

An alternative approach to the former analysis is to compare the fractional residuals inside the *Fermi* Bubbles ROI to the ones inside a reflected *Fermi* Bubbles ROI with an area similar to the original template. Therefore, reflected templates are defined. In case of the HESS Iu template, the initial template has been reflected along the $l = 0°$ axis. The *Fermi*-LAT template is additionally shifted in longitude and latitude to on the one hand avoid an overlap with the initial *Fermi*-LAT template and on the other hand keep it inside the high exposure region. The reflected templates are shown via black dashed contours in the top panel of table 13. Compared to the previous fractional residuals analysis, not only the *Fermi* Bubbles templates are masked during background refitting, but also the reflected ones.
The results in table 13 are consistent with the ones in table 12. In particular, a clear excess ($\approx 3.9\,\sigma$ for the *Fermi*-LAT template and $\approx 5.4\,\sigma$ for the HESS Iu template) is observed.

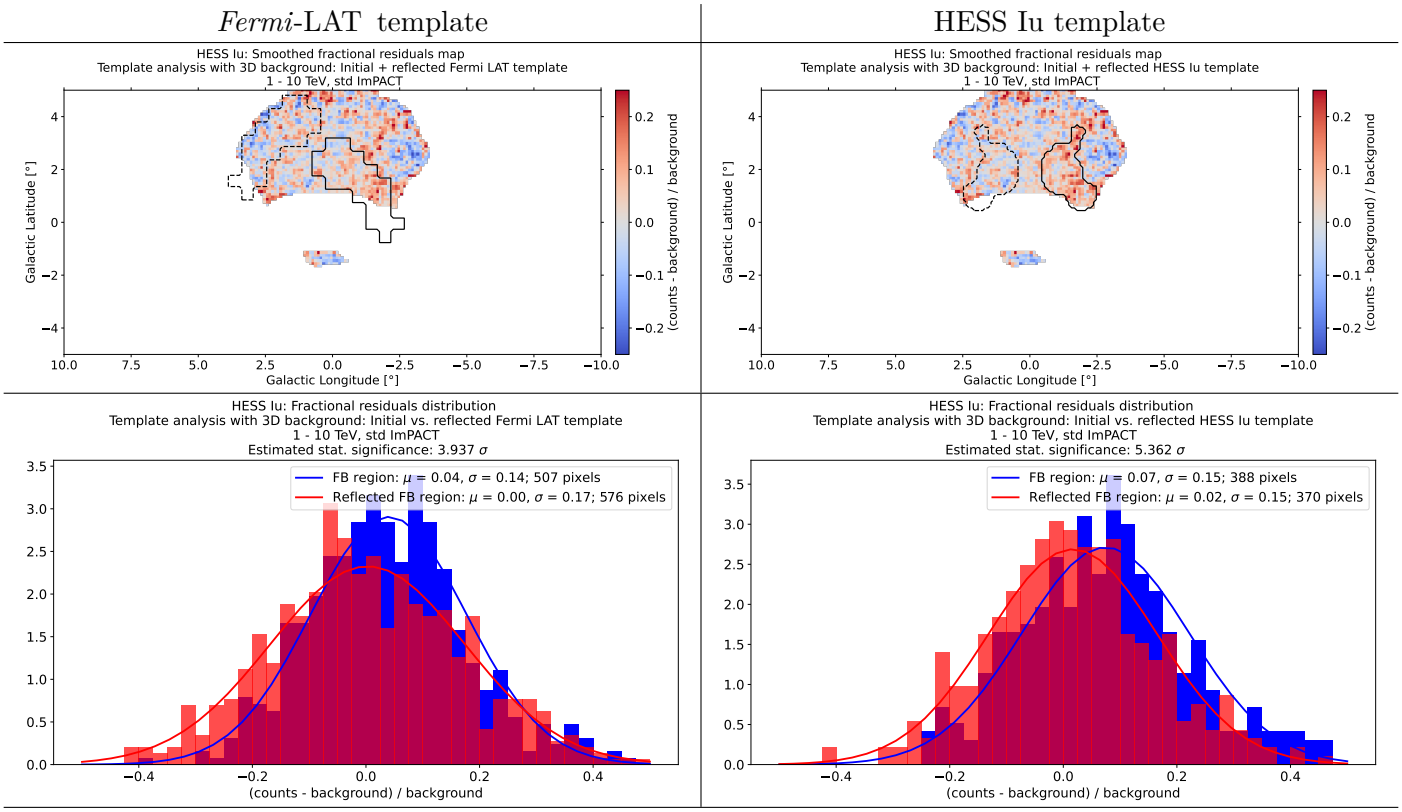

Table 13: *Fermi* Bubbles template analysis using HESS Iu data: Fractional residuals for std ImPACT between 1 and 10 TeV inside the initial and reflected *Fermi* Bubbles ROI. Upper panels show the smoothed fractional residuals maps. A Gaussian kernel with 0.06° width is chosen for smoothening. In the lower panels the distributions of the non smoothed fractional residuals are presented. The left panels are for the analysis performed with the *Fermi*-LAT template, the right ones for the HESS Iu template.

The results for std zeta analysis again reveal a behaviour similar to results of the analysis performed with std ImPACT. The observed excess is even larger ($\approx 5.0\,\sigma$ for the *Fermi*-LAT template and $\approx 7.2\,\sigma$ for the HESS Iu template) than for the std ImPACT analysis. The corresponding plots using the std zeta chain are printed in appendix E.1 in panels c) and d) of figure E1.

8.5.3.3. Division of the full dataset into 10 subsets (based on the fraction of total exposure in the *Fermi* Bubbles ROI)

A test that can be performed to check whether the signal between 1 and 10 TeV, is of physical origin and not induced by background issues of single runs is to divide the full dataset into different subsets. Therefore, the exposure from the stacked dataset that contains all available runs in the full ROI is summed up over all energies, i.e. the map shown in figure G1 c). Based on this, the exposure inside the *Fermi* Bubbles ROI is calculated.
In a next step, subsets of the full dataset are created. This works as follows: The first subset contains available runs covering 10 % of the total exposure inside the *Fermi* Bubbles ROI. The second subset contains runs covering 20 % of the total exposure. In particular, the second subset contains all the runs that are in the first subset and additional runs such that in total 20 % of the total exposure is covered. This procedure is repeated in 10 % steps. The last subset then contains runs covering 100 % of the total *Fermi* Bubbles ROI exposure, i.e. it is the full stacked dataset. As before, the background models of the observations in the different subsets

are refitted and stacked together. The overall background of these stacked datasets is again refitted.
For the resulting datasets,

- mean $\sqrt{TS}$ in the *Fermi* Bubbles ROI
- fractional residuals between 1 and 10 TeV: *Fermi* Bubbles ROI vs. outside region
- fractional residuals between 1 and 10 TeV: *Fermi* Bubbles ROI vs. reflected *Fermi* Bubbles ROI

can be determined. The mean $\sqrt{TS}$ in the *Fermi* Bubbles ROI is determined using the mean value of the $\sqrt{TS}$ distribution achieved by the residual significance map (`ExcessMapEstimator`). The fractional residuals calculations are performed as discussed before. Observing these quantities as function of fractional exposure, it is expected that they show the behaviour of a square root function. Furthermore, the tests listed above are performed for two cases:

- The single observations are temporally ordered.
- The single observations are randomly ordered.

First one means that the order of the single available observations corresponds to the time order in which the data have been taken. In the latter case, all available runs are randomly ordered. The randomised order is used as a cross check since temporally correlated runs may be biased by external influences (e.g. climatic circumstances during one night of data taking) and thus distort the result. However, the results of this analysis for the *Fermi*-LAT template are presented in table 14.
The x-axes of the shown plots indicate the fractional exposure. The plots in the top panel contain information on the evolution of the mean $\sqrt{TS}$ in the *Fermi* Bubbles ROI. The lower panels are dedicated to the statistical significance determined by comparing fractional residuals inside the *Fermi* Bubbles ROI to the outside and reflected region, respectively. A square root function with free amplitude has been fitted to the data points.
Having a closer look at the plots, statistical significance and mean $\sqrt{TS}$ are in general growing as fractional exposure increases. However, only the mean $\sqrt{TS}$ in case of random order is in good agreement with the fitted square root function. This is an indicator that the signal is caused by various and not only a few observations. The randomly ordered datasets in general provide a more square root like shape than the temporally ordered ones. In case of the statistical significance estimation via fractional residuals, the data curves show large fluctuations, especially for low fractional exposure. This effect my appear due to lower statistics contributing to the distributions that are used to calculate the significance.

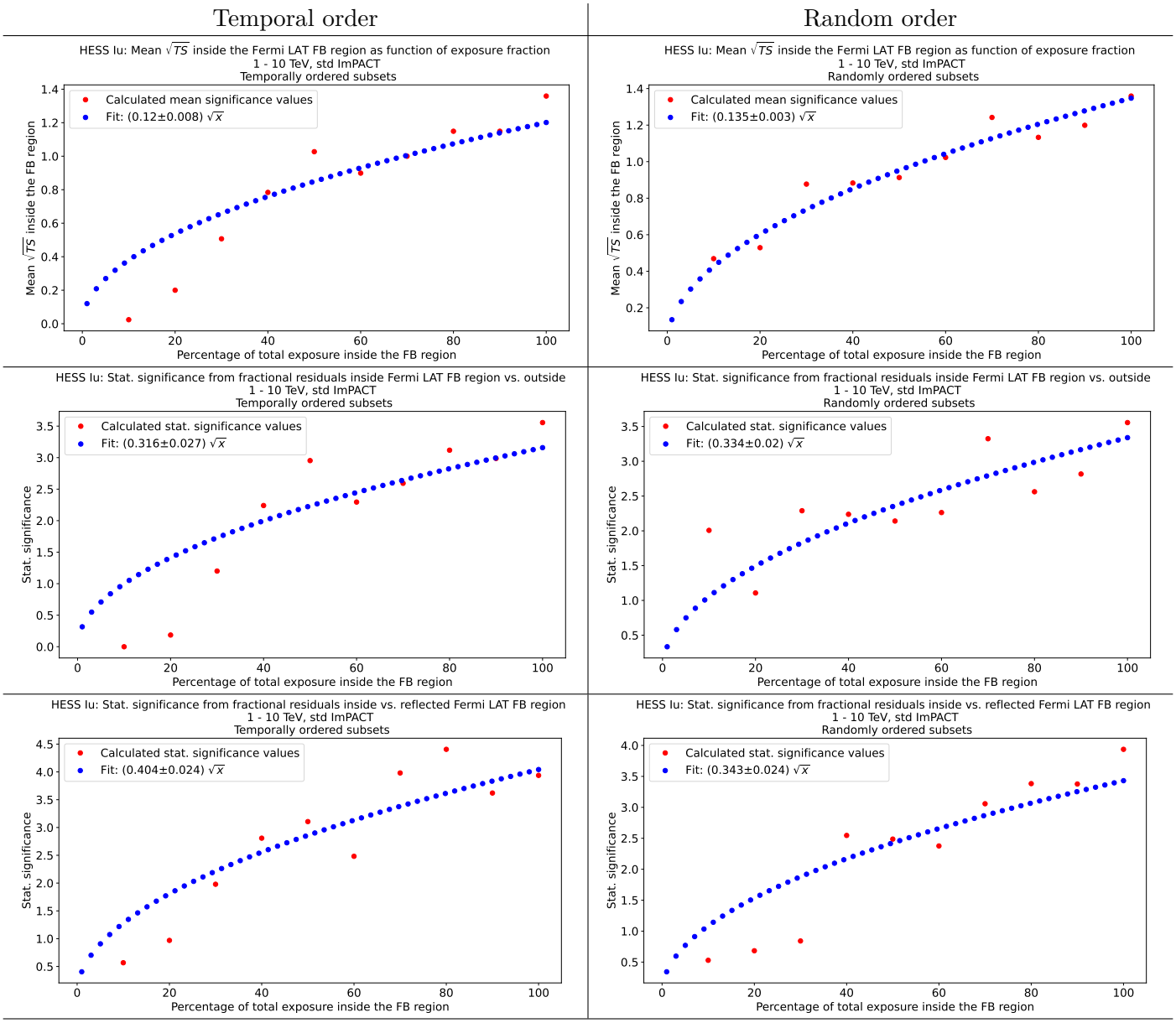

Table 14: *Fermi* Bubbles template analysis using HESS Iu data: Mean $\sqrt{TS}$ and statistical significance as function of fractional exposure for std ImPACT analysis and *Fermi*-LAT *Fermi* Bubbles template. The top row contains the results for the evolution of $\sqrt{TS}$ inside the *Fermi*-LAT *Fermi* Bubbles ROI, the panels below show the evolution of statistical significance using the comparison of the *Fermi* Bubbles ROI one the one hand to the high-exposure region outside (middle row) and on the other hand to the reflected *Fermi* Bubbles ROI. Left panels are for temporally ordered, right panels for randomly ordered datasets.

8.5.3.4. Introduction of an additional gradient to the background model

This test is performed to check the robustness of the fit results with respect to the background model. Therefore, the background data of the single observations are manipulated before the refitting procedure is applied. This is implemented via

$$\mathrm{bkg}'_{\mathrm{r\,i}} = \mathrm{bkg}_{\mathrm{r\,i}} \cdot [1 \pm \mathrm{k} \cdot (\mathrm{alt}_{\mathrm{r\,i}} - \mathrm{alt}_{\mathrm{r\,0}})]. \tag{35}$$

The indices r and i hereby label the different energy and spatial bins, respectively. $\mathrm{alt}_{\mathrm{r}\,0}$ is the altitude Pointing position, i.e. the altitude of the central pixel in energy bin r, $\mathrm{alt}_{\mathrm{r\,i}}$ corresponds to the altitude of pixel i. For each observation, the time centre of the run is used to determine the coordinates for each pixel in the alt-az frame. The factor k represents the estimated background uncertainty per degree in altitude direction. Three cases are considered:

- k = 0.005: Optimistic case
- k = 0.01: Realistic case
- k = 0.1: Pessimistic case

The objective is to investigate whether these background manipulations drastically change the results of the template analysis or in other words to figure out how stable the background model is. To get an idea of how the results for the stacked dataset with refitted background change with increasing k, the residuals maps summed over all energies are inspected in a first step. These maps are shown in table 15 for the *Fermi*-LAT template and std ImPACT.
Comparing the maps to the results without background manipulation in table 11, one does not see any obvious differences in the optimistic (k = 0.005) and realistic (k = 0.01) case. To check whether the background manipulation has an effect at all, the parameter k is changed to 0.1 (pessimistic case). In this case, the residual significance maps change drastically. Interestingly, the colour map is inverted for the plus and minus case, i.e. regions that are overfitted in the plus case reveal unfitted emission in the minus case and vice versa.
Two further quick checks are performed. In first place, the $\sqrt{TS}$ distribution inside the *Fermi* Bubbles ROI can be checked for different choices of k. The results are shown in figure 42 for the minus case. The corresponding plots for the plus case are presented in figure E6 in appendix E.6.
The figure reveals the interesting feature that the result between 1 and 10 TeV is stable independent of the choice of k, i.e. the results are consistent. For the optimistic and realistic case, the results are furthermore consistent with the non manipulated case over all energies. Only the extreme configuration with k = 0.1 shows a dramatic overfitting of the data in the *Fermi* Bubbles ROI. This has been already expected by looking at the bottom left panel of table 15. The result for the plus case (figure E6) is comparable to the minus case at energies between 1 and 10 TeV. In the case where the residuals are summed over all energies the distribution in the pessimistic case is drastically shifted to the right compared to the other cases. This is expected by having a look at the bottom right panel of table 15.
The second quick check that can be performed, is the calculation of the spectra using the manipulated datasets. The results are shown in figure 43.
The outcome of this analysis is that the spectra are consistent for both the plus and minus case as well as for all choices of k at energies above 1 TeV. This means that the background model works stable at higher energies, even though a large uncertainty has been assumed. In particular, the signal between 1 and 10 TeV may not be a result of background distortion. The background manipulation mainly affects the lowest energy bins. In figure 43 b), the plus case, the flux at the lowest energy in the pessimistic (k = 0.1) case is roughly twice as large as for the other cases. This corresponds to a large positive discrepancy between counts and predicted background counts as observed in the bottom right panel of table 15, i.e. the residuals map summed over all energies seems to be dominated by the lower energies. For the minus case in figure 43 a), the lowest flux point in the pessimistic case is an upper limit. Inspecting the data, it is found that the upper limit is set since the flux is negative, i.e. the data inside the *Fermi* Bubbles ROI are overfitted which is consistent with the bottom left panel of table 15.

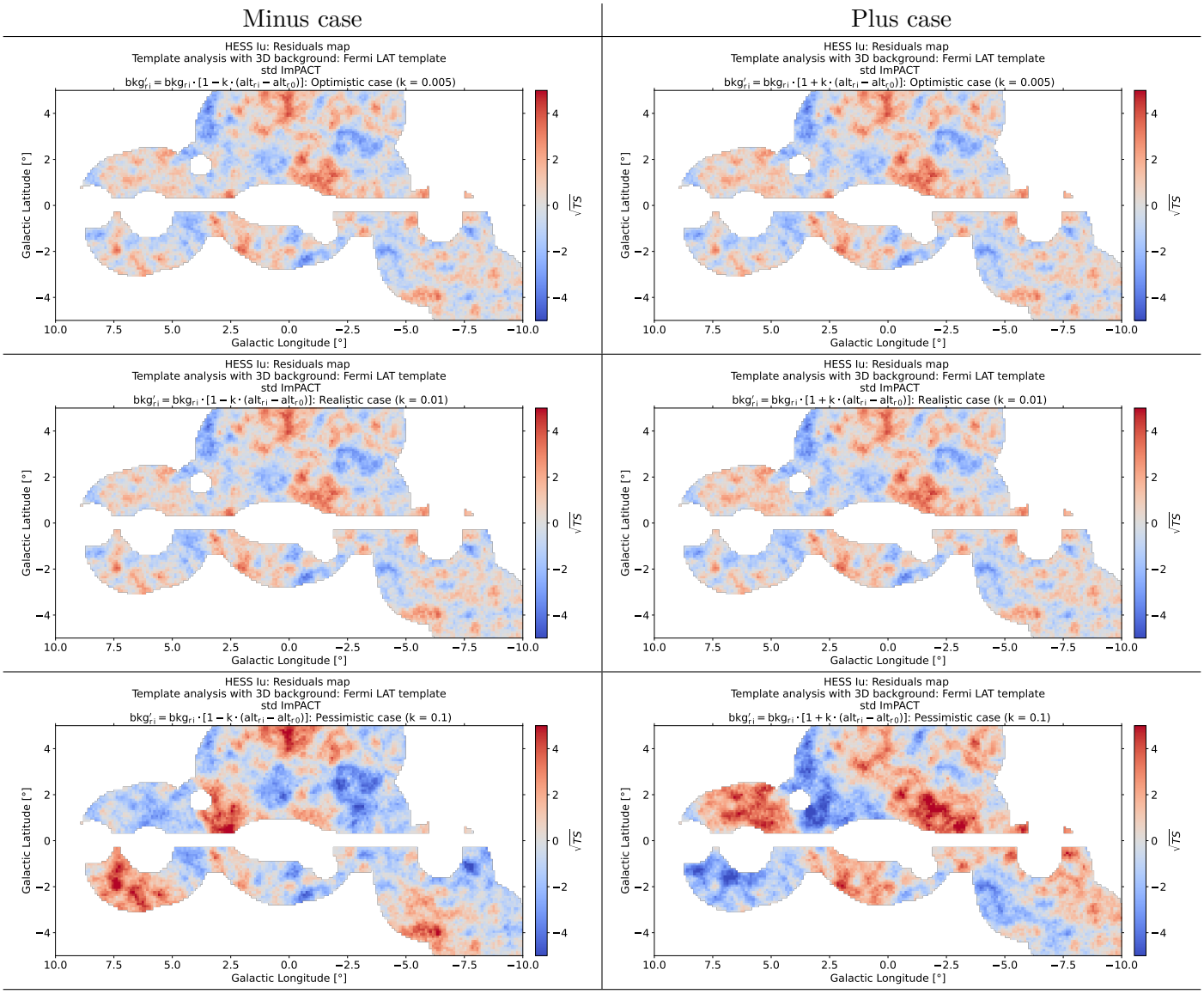

Table 15: *Fermi* Bubbles template analysis using HESS Iu data: Residual significance maps summed over all energies for the *Fermi*-LAT *Fermi* Bubbles template analysis and std ImPACT. The different rows contain different choices for values of k. Top row: Optimistic case; mid row: realistic case; bottom row: Pessimistic case

8.5.3.5. Addition of a spatial tilt in longitude and latitude direction to the background model

It is possible to choose a best-fit approach to determine a spatial tilt in both longitude and latitude direction. This has been implemented by Katrin Streil [78]. The 3D background model can for this purpose be updated by a spatial component. The resulting background rate is the product of the spectral (see equation (14)) and the spatial component, in particular

$$R' = R \cdot \left(\frac{E}{E_0}\right)^{-\delta} \cdot [1 + \mathrm{tilt_{lon}} \cdot (\mathrm{l_0} - \mathrm{l_i}) + \mathrm{tilt_{lat}} \cdot (\mathrm{b_0} - \mathrm{b_i})] \tag{36}$$

where $\mathrm{tilt_{lon}}$ and $\mathrm{tilt_{lat}}$ are the free parameters of the spatial model. $\mathrm{l_0}$ and $\mathrm{b_0}$ are the longitude and latitude coordinates of the center point of tilt. Based on these centre points, the angular offset in longitude and latitude direction with respects to the i-th spatial pixels is calculated.

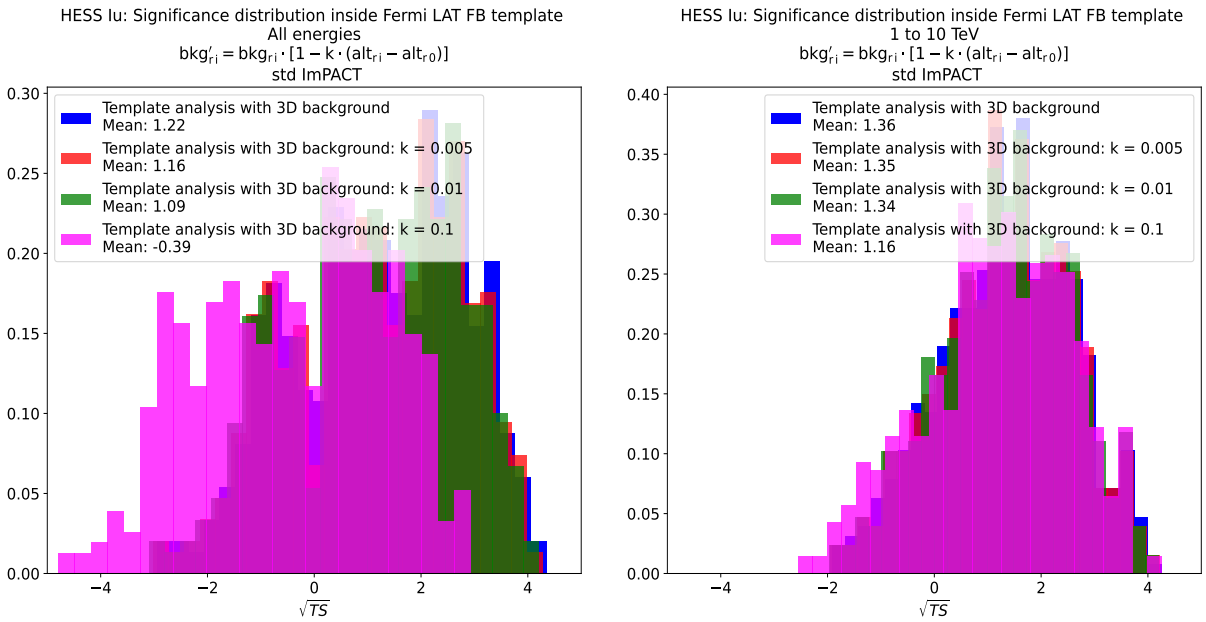

(a) Summed over all energies

(b) 1 - 10 TeV

Figure 42: *Fermi* Bubbles template analysis using HESS Iu data: $\sqrt{TS}$ distribution in the *Fermi*-LAT *Fermi* Bubbles ROI for the stacked dataset with and without manipulated background of single observations before refitting using the std ImPACT algorithm. The minus case is shown.

This updated model is then used for the run-wise background refitting applying the same exclusion mask than for the conventional *Fermi* Bubbles template analysis. l_0 and b_0 are set to the center coordinates of the single observations. The background of the resulting stacked dataset is then refitted with the conventional 3D background model. Note that the updated background model is not applicable in combination with Gammapy v.0.19; hence, this analysis has been performed with v.0.18.2.
The first performed inspection is comparing the fractional difference of the expected background for the stacked dataset where the tilted background model has been applied for run-wise background refitting to the one with the conventional 3D background model, i.e.

$$\frac{\mathrm{bkg}_{\mathrm{w/o\ tilt}} - \mathrm{bkg}_{\mathrm{with\ tilt}}}{\mathrm{bkg}_{\mathrm{with\ tilt}}}. \tag{37}$$

The results of this calculation are shown as 2D maps for different energy ranges in figure 43 for the *Fermi*-LAT template and std ImPACT analysis.
Having a look at figure 43 the morphology is the same for all maps. The fractional difference is in the order of $\pm$ 3 %, i.e. in the expected range. The results in the *Fermi*-LAT *Fermi* Bubbles ROI are contrary to the results outside. Additionally, the maps summed over all energies (panel a)) and below 1 TeV (panel c)) look very similar to each other whereas the map for energies between 1 and 10 TeV (panel b)) looks less flat. This leads to the conclusion that the spatial tilt may be dominated by low energies.
As a check, the background refitting per observation (using the updated background model with spatial tilt in longitude and latitude direction) is repeated on the one hand for energies below and on the other hand for energies above 1 TeV. The background refitting results of the spatial tilt parameters are then compared to the results where the fitting has been performed taking into account all energies. The achieved distributions in the different energy ranges are shown in

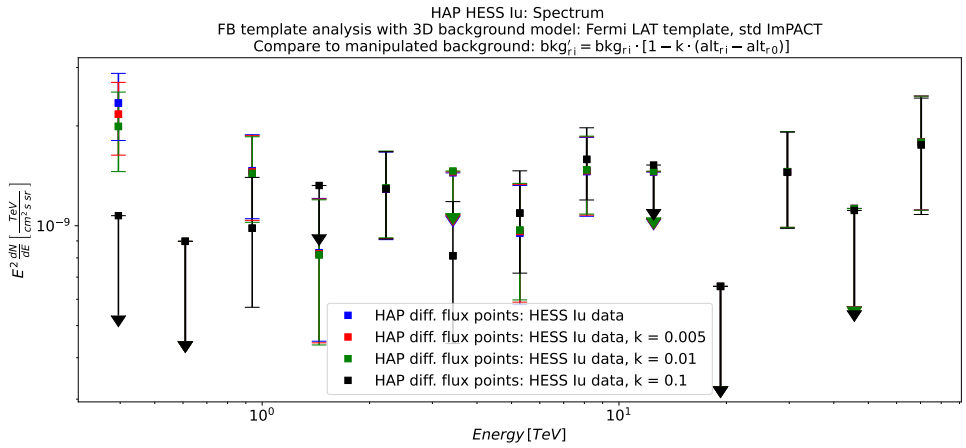

(a) Minus case

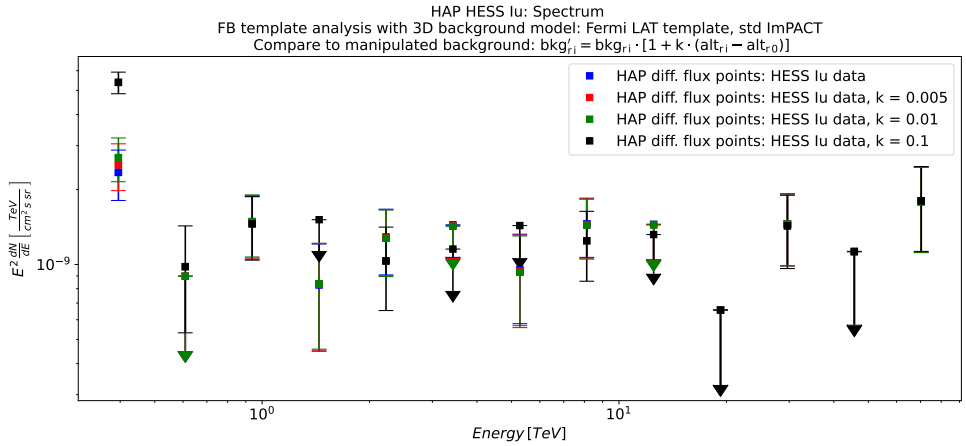

(b) Plus case

Figure 43: *Fermi* Bubbles template analysis using HESS Iu data: Comparison of the spectra achieved in the standard *Fermi* Bubbles template analysis to the spectra computed for different choices of the estimated background uncertainty k. The shown spectra are for the *Fermi*-LAT *Fermi* Bubbles template and std ImPACT.

table 16.
Having a look at the right column of table 16, one realises that the distributions when fitting has been performed over all energies and exclusively below 1 TeV are almost the same. In contrast, the achieved distributions for energies above 1 TeV reveal a more spread character than the one for all energies. This is a clear indication that the spatial tilt is dominated by low energies. This is consistent with the inspected residual significance maps in figure 44 that are achieved using the tilted bkg model for run-wise background refitting. The map summed over all energies is flat compared to the one in the top left panel of table 11 while the map for energies between 1 and 10 TeV is less influenced. In particular, the tilted background model improves the results, but does not have a strong effect on data at higher energies. This is in accordance with the results from the previous sub-chapter.
One last interesting remark is that the spatial background tilt is mostly affected by statistical effects. Therefore, distributions with the significance values of the best-fit values are plotted in figure 45. The plots are created dividing the best-fit values by the returned parameter errors for all single observations. The results for the background tilt in longitude direction as well as the one in latitude direction are nearly Gaussian distributed (with mean ≈ 0 and $\sigma \approx 1$) when fitting

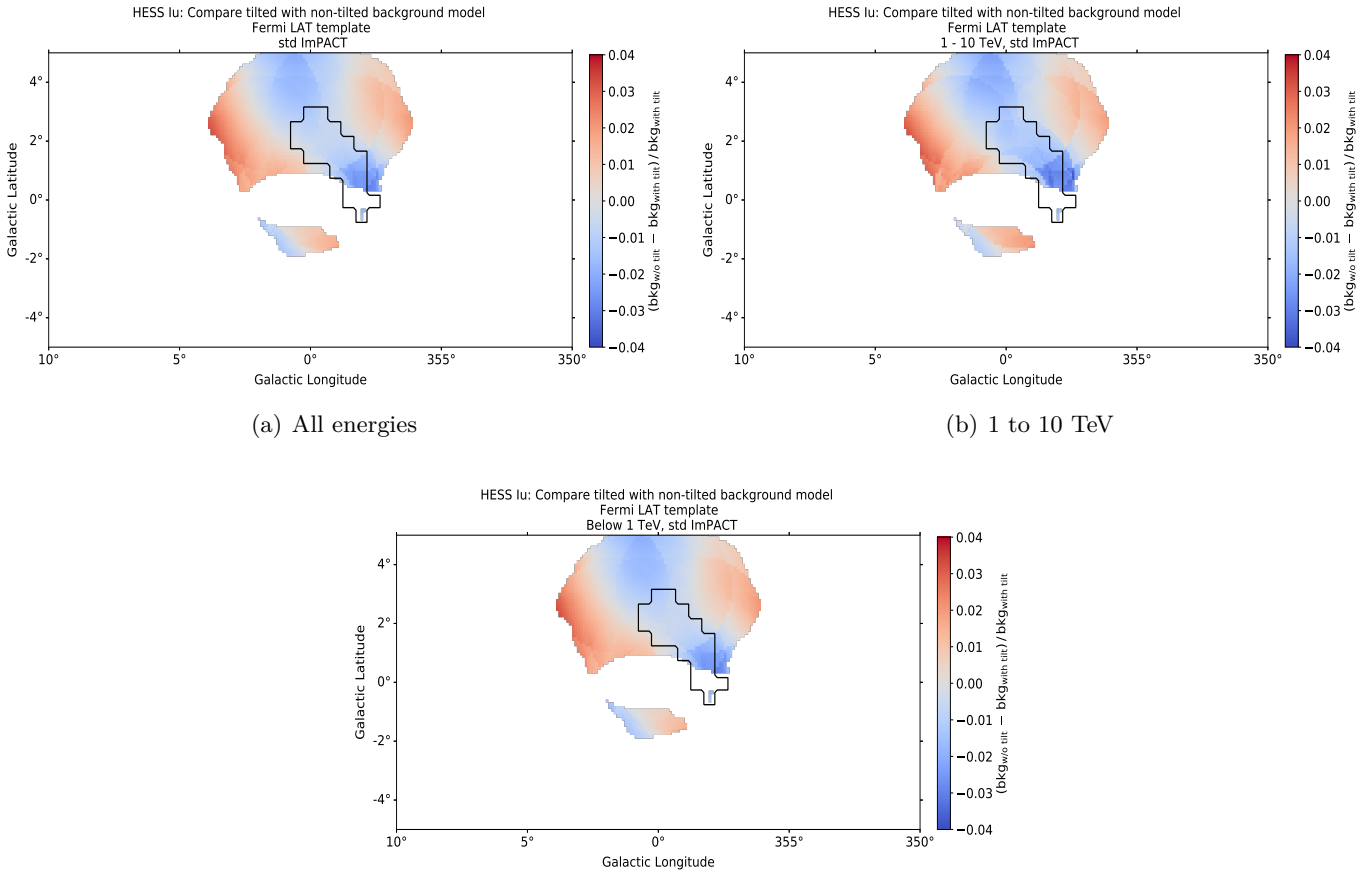

(a) All energies

(b) 1 to 10 TeV

(c) Below 1 TeV

Figure 43: *Fermi* Bubbles template analysis using HESS Iu data: Fractional difference of expected background calculated from the stacked datasets where the background model with and without spatial tilt has been used for run-wise background refitting. The maps show different energy ranges. The analysis is performed with std ImPACT and the *Fermi*-LAT *Fermi* Bubbles template.

has been performed using the full energy range. The same effect is observed when exclusively data above or below 1 TeV have been taken into account.

8.5.3.6. Estimation of systematic background uncertainty

In this part, the systematic background uncertainties are evaluated quantitatively. Therefore, two approaches are used:

- Estimation of systematic uncertainty from data in the reflected *Fermi* Bubbles ROI
- Estimation of systematic uncertainty from high latitude ($|b| > 5°$) runs

Both, high latitude runs and the reflected *Fermi* Bubbles ROI, are considered as off-regions, i.e. no signal from the *Fermi* Bubbles and further strong γ-ray emitting sources is expected. The basic idea is to determine the fractional uncertainty per energy bin for both approaches. Note that from now on, the conventional background model without spatial tilt is used again to the end of this thesis.

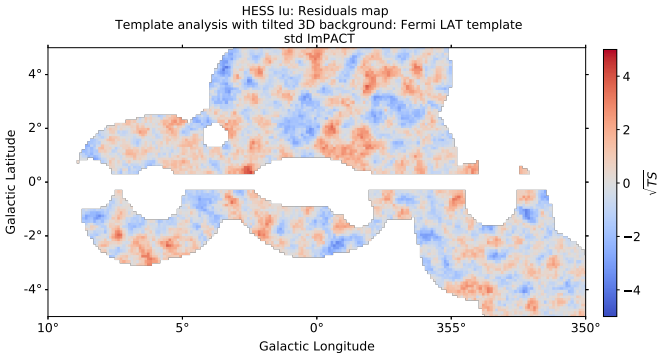

(d) All energies

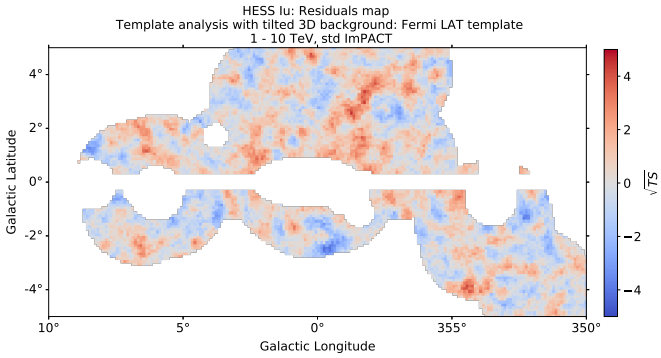

(e) 1 - 10 TeV

Figure 44: *Fermi* Bubbles template analysis using HESS Iu data: Residual significance maps summed over all energies for the *Fermi*-LAT *Fermi* Bubbles template analysis and std ImPACT. To create these maps, the tilted background model is used in the run-wise background refitting.

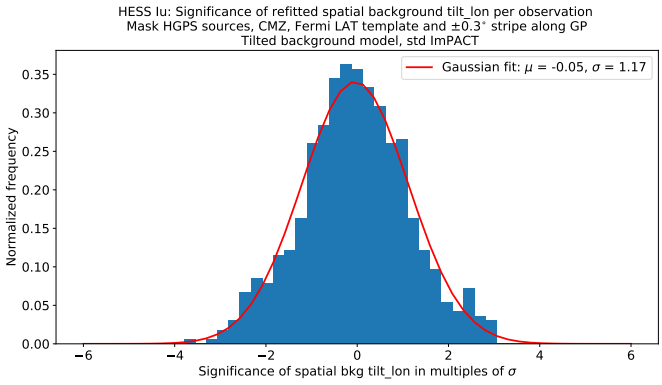

(a) Longitudinal tilt

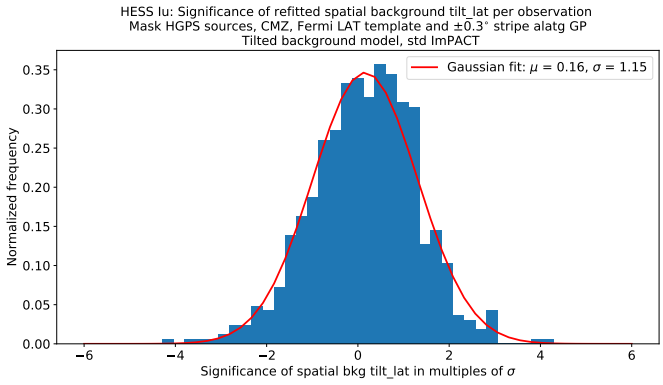

(b) Latitudinal tilt

Figure 45: *Fermi* Bubbles template analysis using HESS Iu data: Significance distributions of the spatial background tilt parameters achieved in the run-wise background refitting for std ImPACT and *Fermi*-LAT *Fermi* Bubbles template analysis.

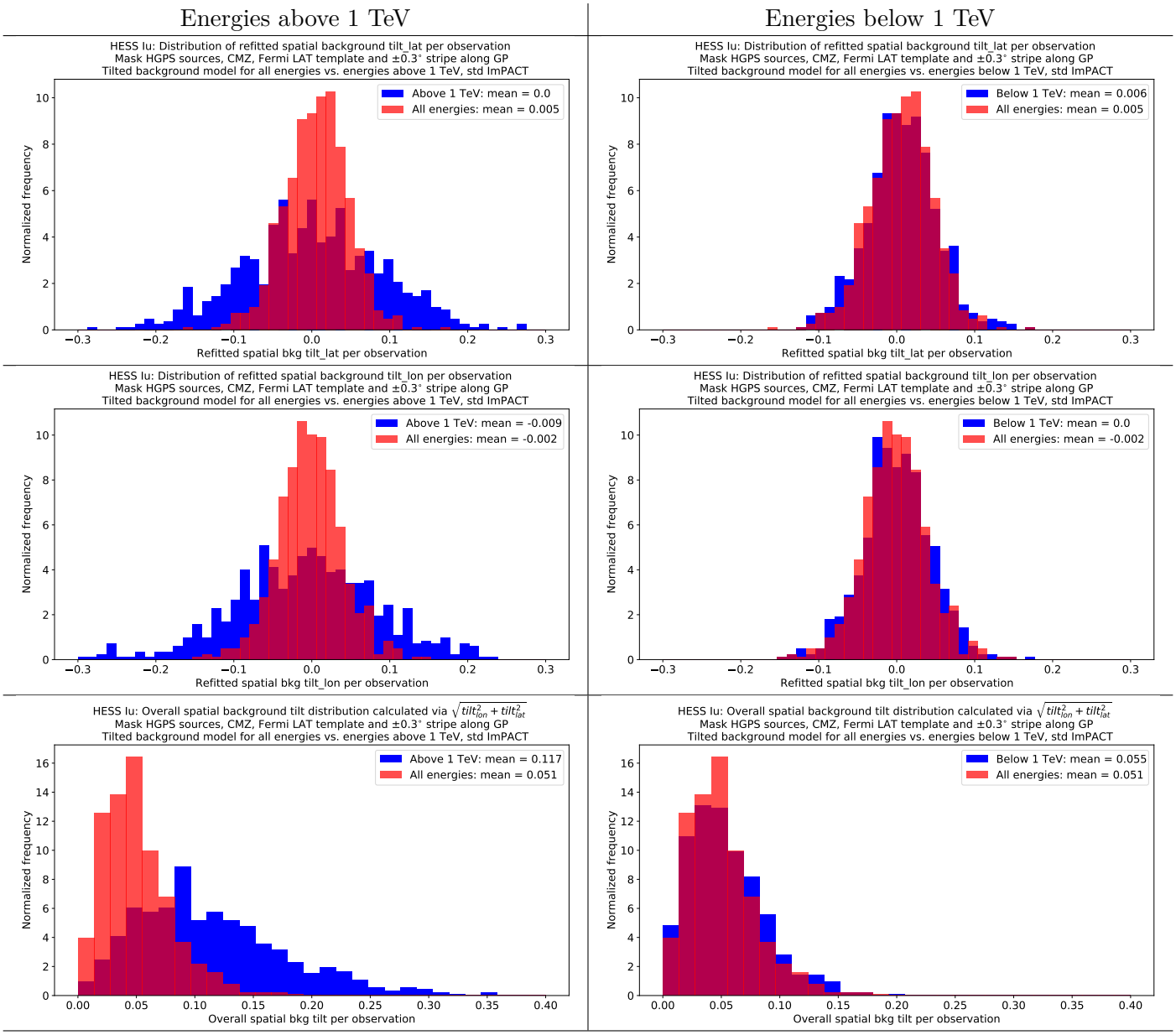

Table 16: *Fermi* Bubbles template analysis using HESS Iu data: Distributions of the best-fit values of the spatial tilt parameters from run-wise background refitting above 1 TeV (left column) and below 1 TeV (right column). The top and mid row show the results for the tilt in latitude and longitude direction, respectively, the bottom panel for the total tilt.

Estimation from reflected *Fermi* Bubbles ROI

For the uncertainty estimation using the reflected *Fermi* Bubbles ROI, the fitting procedure works in the same way as described before in chapter 8.5.3.2. However, this time, the fractional residuals are summed over all spatial pixels within a certain energy bin instead of summing over the spectral axis and keep the spatial properties as before. To achieve a proper uncertainty estimation in the end, the absolute values of the fractional residuals are then plotted as function of the mean logarithmic energy of the different energy bins. In a next step, a running mean approach is used to smooth the obtained data curve. For each energy bin, the running mean is determined by averaging over the bin itself and its two neighboured bins. As a final step, a

spline interpolation is performed to achieve a final systematic uncertainty curve. The results for a linear and cubic spline interpolation do not differ a lot. In the further course, data from the cubic spline interpolation are used. This procedure for the *Fermi*-LAT template and std ImPACT is illustrated in table 17 in the top left panel.

std ImPACT	std zeta
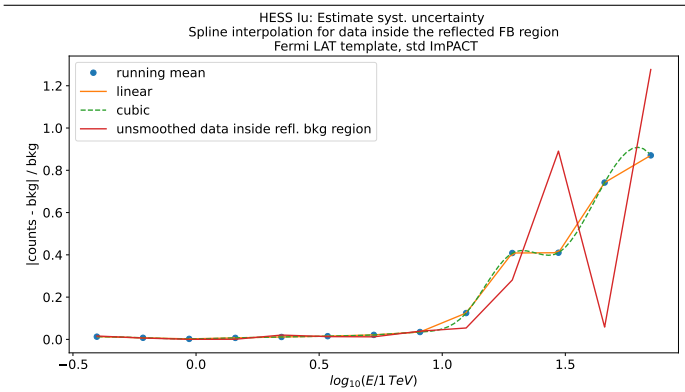	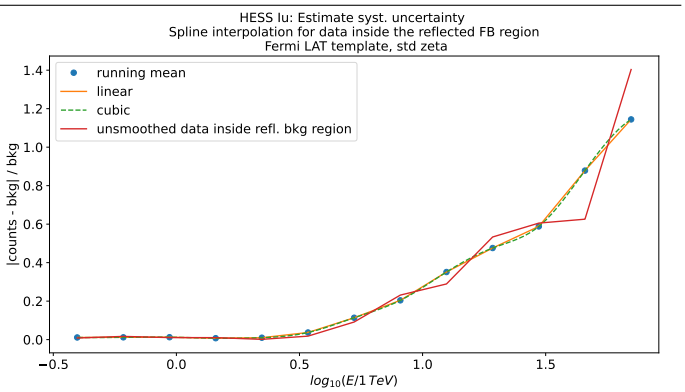
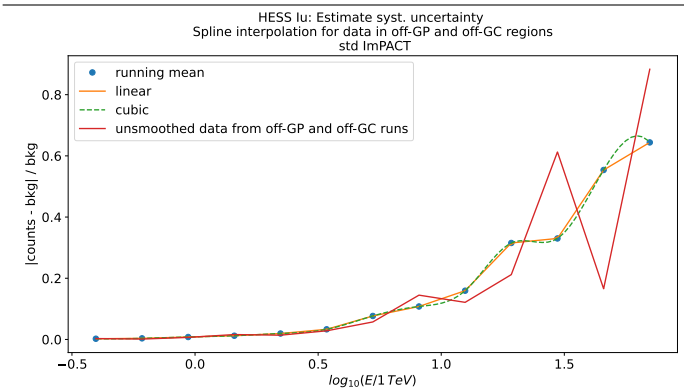	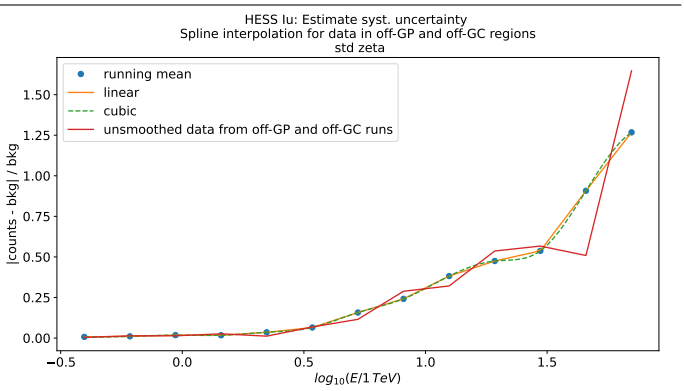

Table 17: *Fermi* Bubbles template analysis using HESS Iu data: Systematic uncertainty estimation for the *Fermi*-LAT template from the reflected *Fermi* Bubbles ROI (top row) and high latitude runs (bottom row). Results for the std ImPACT and std zeta analysis are compared.

Having a closer look at the top left panel of table 17, one observes that the fractional uncertainty is very low at low energies. Up to $\approx$ 10 TeV, it is in the range of a few percent. Above 10 TeV, the fractional uncertainty increases drastically. An interesting feature seen in the std ImPACT analysis is the peak at $\approx$ 30 TeV . This peak may be connected to the energy binning of the std ImPACT background model that has a course binning at high energies, i.e. above $\approx$ 10 TeV it may only have one energy bin [51], [79]. In the top right panel, the same analysis procedure is shown for std zeta analysis. In this case, the curve reveals larger uncertainties up to $\approx$ 10 TeV, but is smooth over the full energy range, i.e. it appears to be more reasonable than in the std ImPACT case. However, the order of magnitude of the curves of both reconstruction algorithms is comparable.

Estimation from high latitude runs ($|b| > 5°$)

The approach of estimating the systematic background uncertainty with high latitude runs has been introduced by Kaori Nakashima [79]. Detailed information can be found on the confluence page *Systematic studies of the HAP-HD background model* [19]. The underlying code that has

[19] `https://hess-confluence.desy.de/confluence/display/HESS/Systematic+studies+of+the+HAP-HD+background+model`

been used as starting point for the analysis performed in this thesis is publicly available on GitHub [20].
In short, the idea is to only look at observations at high latitudes ($|b| > 5°$) and away from the GC in longitude ($60° < l < 300°$). In total, 1497 HESS Iu runs are available for std ImPACT and 1502 for std zeta analysis chain following the standard quality criteria used in this thesis. For each of the runs, the background model is refitted using normalisation and tilt as free parameters. During this refitting process, known γ-ray emitting sources are masked. Afterwards, γ-ray and predicted background counts are saved as function of the energy for the single datasets with refitted background. Note that the single observations are not stacked to a full dataset in contrast to former analysis.
The high latitude runs are grouped into seven zenith bins. Thus, in a last step, the fractional residuals determined from event and background counts of all high latitude observations are weighted with the amount of runs per zenith bin of the IGS observations that have been used to build the stacked dataset used for the *Fermi* Bubbles analysis (i.e. 676 HESS Iu runs for std ImPACT and 675 for std zeta). The final results of the systematic uncertainty estimation using high latitude runs are presented in the bottom row of table 17. The course of these curves is consistent with the ones achieved from the reflected *Fermi* Bubbles ROI indicating that the reflected *Fermi* Bubbles ROI can be nicely used as an off-region without any drastic signal.
The last missing piece to use the determined systematic uncertainties quantitatively is a transformation of the fractional uncertainty to intensity units. This can be achieved by

$$I_{syst.}(E_\alpha) = \frac{|\text{counts}_\alpha - \text{bkg}_\alpha|}{\text{bkg}_\alpha} \cdot \frac{1}{\Delta E_\alpha \cdot \Delta\Omega_{FB}} \cdot \frac{\text{bkg}_{\text{FB},\alpha}}{\text{exposure}_{\text{FB},\alpha}} \tag{38}$$

where $|\text{counts}_\alpha - \text{bkg}_\alpha| / \text{bkg}_\alpha$ is the fractional uncertainty in energy bin α determined either within the reflected *Fermi* Bubbles ROI or outside the masked γ-ray emitting regions in case of the high latitude runs. The last multiplicand maps the fractional uncertainty to background intensity units within the original *Fermi* Bubbles ROI. $\text{bkg}_{\text{FB},\alpha}$ and $\text{exposure}_{\text{FB},\alpha}$ are the predicted background counts and exposure in energy bin α inside the *Fermi* Bubbles ROI. ΔE_α again denotes the with of the energy bin and $\Delta\Omega_{FB}$ the solid angle of the contributing part of the *Fermi* Bubbles template in units of sr.

8.6. Full HESS Iu spectra

In this section, the full spectra for the HESS Iu analysis with the HAP 3D background model are presented including the systematic uncertainty bands derived in the previous chapter 8.5.3.6. Additionally, PA differential flux points - achieved by a reflected background analysis using a *Fermi*-LAT data-based *Fermi* Bubbles template - are added to the plots. The PA spectra are computed by Alessandro Montanari using H.E.S.S. data between 2014 and 2020 as well as the same definition for the *Fermi*-LAT *Fermi* Bubbles template as presented in figure 4. Details on this analysis can be found on the confluence page *PA Reflected Background analysis* [21]. For comparison to HAP data, the PA observed flux points are taken into account. Deviating from the confluence page, observed flux points above 1.73 TeV have been also computed, but are statistically not significant [33]. However, these non significant points are correspondingly added to the plots as upper limits.
The spectra for HAP HESS Iu template analysis and added systematic uncertainty bands as well as PA differential flux points are shown for the *Fermi*-LAT template in figure 46 a) for std ImPACT and b) for std zeta analysis.

[20] https://github.com/kaoriinakashima/HESS_3Dbkg_syserror
[21] https://hess-confluence.desy.de/confluence/display/HESS/PA+Reflected+Background+analysis

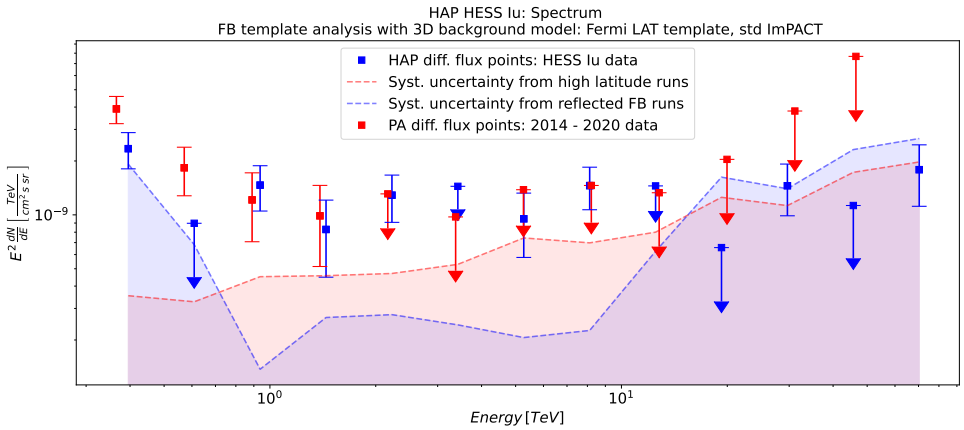

(a) std ImPACT

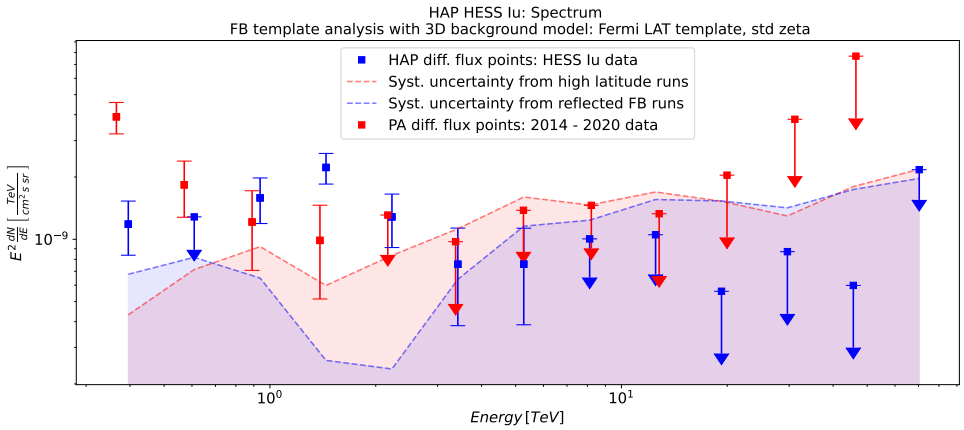

(b) std zeta

Figure 46: *Fermi* Bubbles template analysis using HESS Iu data: Spectra for the *Fermi*-LAT *Fermi* Bubbles template with systematic uncertainty bands and added PA flux points.

Having a look at the results of the std ImPACT analysis shown in figure 46 a), one notices that the derived HAP flux points are consistent with the PA flux points within the uncertainties at energies up to a few TeV. At higher energies, the PA upper limits are consistent with the HAP points, even though the HAP flux points may reveal a statistically significant signal while only upper limits are observed for PA data. In particular, the integrated statistical significance σ_{stat} for flux points achieved in the HAP HESS Iu *Fermi* Bubbles template analysis is larger than $6.4\,\sigma$ for all configurations as shown in table 18. The statistical significance is again larger when using the HESS Iu instead of the *Fermi*-LAT template. Moreover, the statistical significance is larger for std zeta compared to std ImPACT. This is consistent with the stronger residuals that have been observed in table 11 for std zeta compared to std ImPACT. Furthermore, the determined significance of the mean values of the fractional residual distributions calculated in chapters 8.5.3.1 and 8.5.3.2 have been found to be larger for std zeta compared to std ImPACT. For the PA flux points, σ_{stat} is found to be $\approx 2.54\,\sigma$.
Note that the two significant (i.e. more than $2\,\sigma$ statistical significance) HAP HESS Iu flux points in the std ImPACT analysis at high energies may occur due to low statistics on the one hand and large systematic uncertainties on the other hand. It is further interesting to observe that the HAP flux points are above the systematic uncertainty bands (from high latitude runs as well as from reflected *Fermi* Bubbles ROI) at energies between 1 and 10 TeV when using

Table 18: *Fermi* Bubbles template analysis using HESS Iu data: Statistical significance of the differential flux points between 1 and 10 TeV determined for different analysis configurations.

Algorithm + template	σ_{stat} between 1 and 10 TeV
std ImPACT + *Fermi*-LAT	$6.36\,\sigma$
std ImPACT + HESS Iu	$9.95\,\sigma$
std zeta + *Fermi*-LAT	$7.48\,\sigma$
std zeta + HESS Iu	$10.39\,\sigma$

the std ImPACT algorithm. Furthermore, the systematic uncertainty from high latitude runs is lower than for data from the reflected *Fermi* Bubbles ROI at low energies while it is vice versa between 1 and 10 TeV. At high energies (above $\approx$ 10 TeV) both uncertainty curves are similarly increasing.
For the std zeta analysis in figure 46 b), especially at the lowest energy bin, there is a large discrepancy between the HAP and PA data, i.e. the PA flux is a factor of three to four larger than for HAP analysis. However, at higher energies, HAP and PA results are consistent. In contrast to the std ImPACT analysis, the estimated systematic uncertainties are much higher at energies between $\approx$ 2 and 10 TeV, i.e. the flux in this energy range shows a high statistical significance, but may be dominated by systematics. The systematic uncertainty derived from the high latitude runs is larger than the one from the reflected *Fermi* Bubbles ROI at energies between 1 and 10 TeV.
The spectra for the HESS Iu analysis performed with the HESS Iu template are printed in appendix E.2 in figure E2. For both, std ImPACT and std zeta, the results achieved using the HESS Iu template are consistent with the results from the template analysis using the *Fermi*-LAT template.

8.7. HESS I and II analysis results

HESS I and II data are analysed in the same way as HESS Iu data (chapter 8.5). In particular, residuals significance maps are presented in this chapter as a first indicator.

HESS I data

The residual significance maps for HESS I data are shown in table 19 for std ImPACT as well as std zeta. The *Fermi*-LAT template has been used. Having a look at the bottom row, the maps do not reveal any emission between 1 and 10 TeV. The maps in the top row on the other side show a slight excess in the region around the GC and the *Fermi* Bubbles ROI. This excess seems to be again dominated by the low energies which can be checked by having a look at figure 47. This signal in the vicinity of the *Fermi* Bubbles ROI may be connected to runs with high muon efficiency since at low energies the runs with high muon efficiency result in a large-scale ring-like structure around the GC which may be not of physical origin, but more likely caused by systematical issues.
Coming back to figure 47, the only significant flux point in this case is the lowest energetic one. The systematic uncertainty curve for the reflected *Fermi* Bubbles ROI indicates that the systematics are very large at low energies. Interestingly, the systematic uncertainty from the reflected *Fermi* Bubbles ROI is way larger than the one from high latitude runs. In addition, the systematic uncertainty determined from the reflected *Fermi* Bubbles ROI decreases at high energies. The HESS I spectra for std zeta and HESS Iu template analysis are printed in figure E3 in appendix E.3. Note that in case of the HESS I analysis with the *Fermi*-LAT template, the

reflected *Fermi* Bubbles ROI is defined differently than for the HESS Iu analysis since at higher latitudes the exposure vanishes. The reflected *Fermi* Bubbles ROI in this case is indicated via the dashed contour in the top left panel of table 19. The reflected HESS Iu template is unchanged compared to before, i.e. it is the same as shown in the top right panel of table 13.

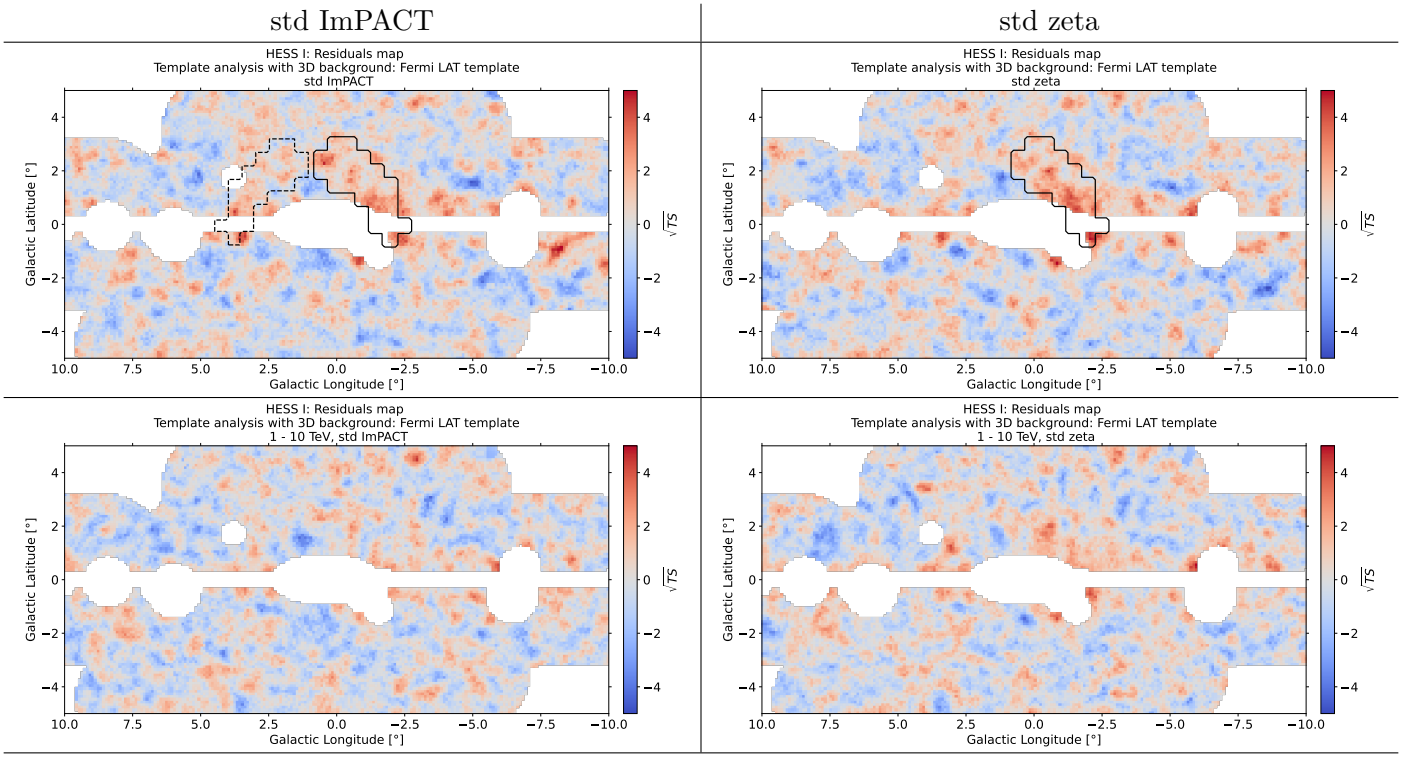

Table 19: *Fermi* Bubbles template analysis using HESS I data: Residual significance maps for the *Fermi* Bubbles template analysis performed with the *Fermi*-LAT template and both std ImPACT and std zeta. Top row: Maps summed over all energies. Bottom row: Maps summed over energies between 1 and 10 TeV.

HESS II data

The residual significance maps for HESS II data are shown in table 20 for std ImPACT as well as std zeta. In the right column where the results for std zeta analysis are presented, no remarkable signal in the vicinity of the *Fermi* Bubbles ROI is detected. In the left column, i.e. the std ImPACT analysis, there is a slight excess visible when residuals are summed over all energies. The bottom left panel reveals that there is furthermore a slight signal between 1 and 10 TeV. The brightest excess in this map directly borders on the CMZ and and thus seems to be connected to the CMZ excess.
The resulting spectra for the HESS II analysis are shown in figure E4. Note that a reflected *Fermi* Bubbles ROI has not been defined for HESS II data due to the low coverage of the full ROI. A look at the spectra reveals that most of the flux points are upper limits. There is one flux point at an energy of ≈ 1.4 TeV that appears as significant point in all plots except for the one determined for std zeta and HESS Iu template. However, this flux point is well above the uncertainty band. Nevertheless, a signal detection cannot be stated based on these plots.

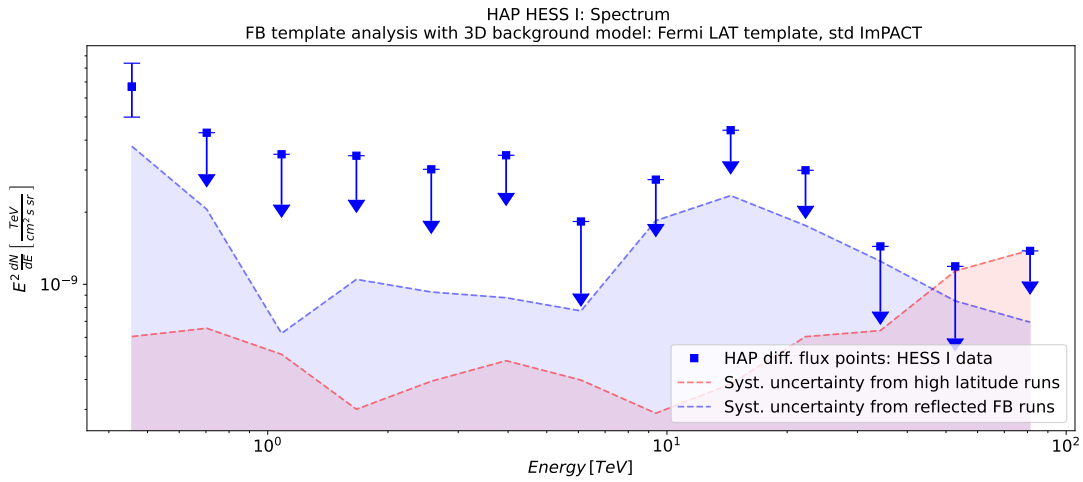

Figure 47: Spectrum for HESS I data and std ImPACT analysis with the *Fermi*-LAT template.

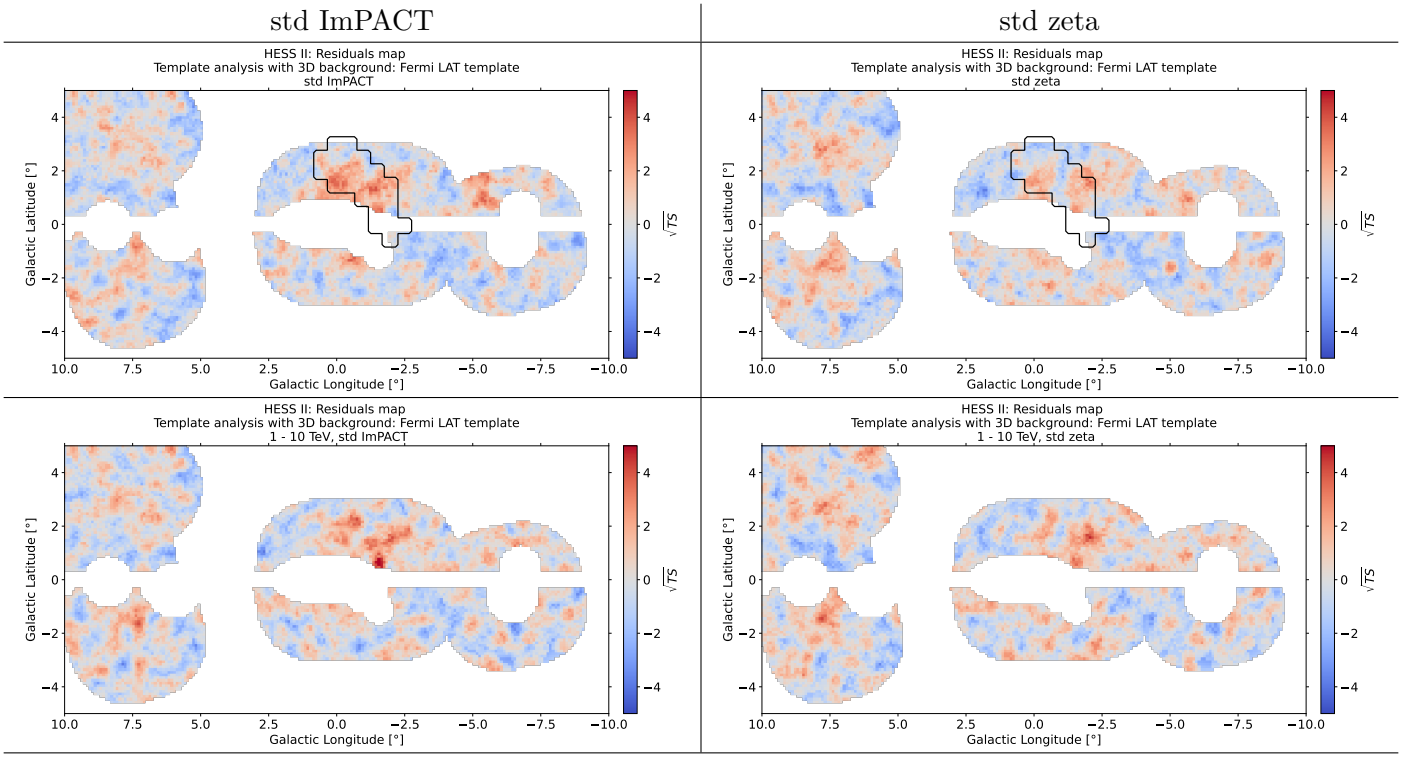

Table 20: *Fermi* Bubbles template analysis using HESS II data: Residual significance maps for the *Fermi* Bubbles template analysis performed with the *Fermi*-LAT template and both std ImPACT and std zeta. Top row: Maps summed over all energies. Bottom row: Maps summed over energies between 1 and 10 TeV.

8.8. Comparison of spectra from all H.E.S.S. eras

The spectra of all H.E.S.S. eras are compared in one plot as a consistency check. For the analysis with the *Fermi*-LAT template, PA data are also added to the plots in figure 48.
Having a look at the spectra for the different configurations, the added flux points of the HESS I and II analysis are consistent with the results from HAP HESS Iu and PA analysis. In particular, the upper limits determined from HESS I and II data are not in conflict with the HAP HESS Iu and PA analysis. The most interesting flux points are the HESS II points at $\approx$ 1.4 TeV that

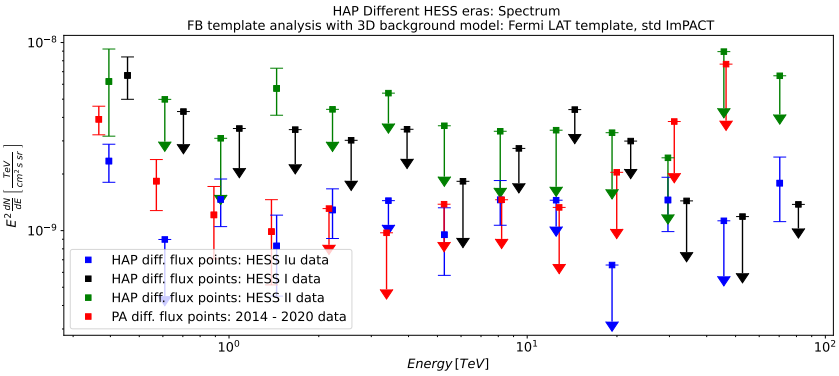

(a) std ImPACT + *Fermi*-LAT template

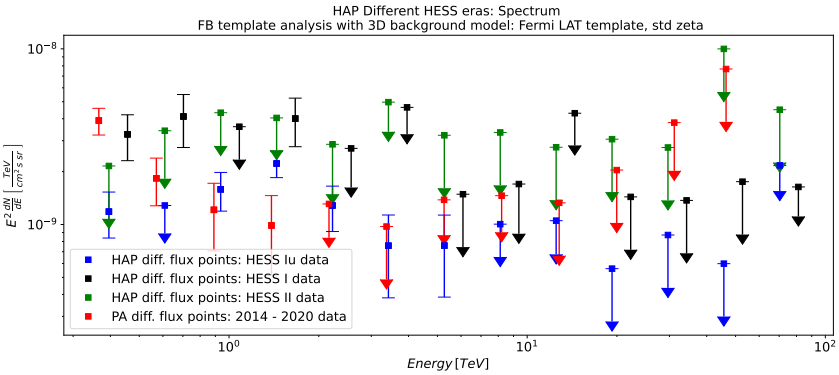

(b) std zeta + *Fermi*-LAT template

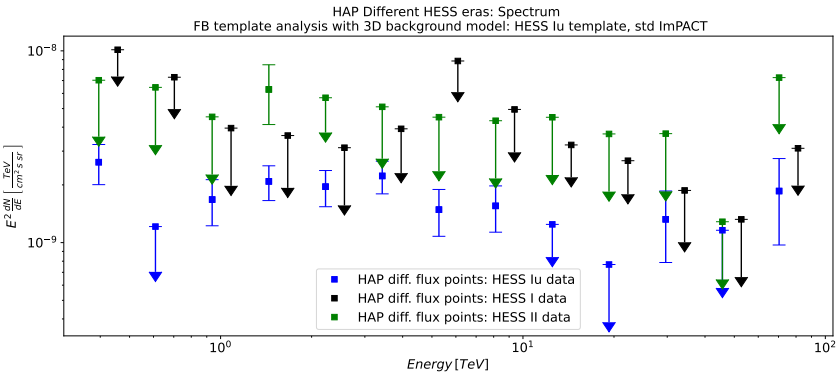

(c) std ImPACT + HESS Iu template

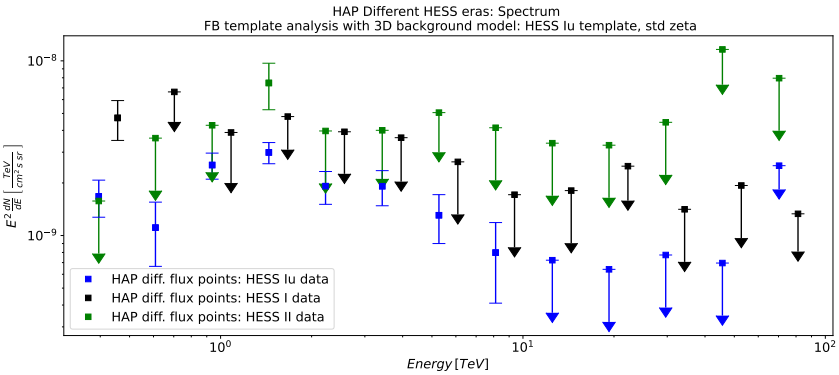

(d) std zeta + HESS Iu template

Figure 48: Spectra for all H.E.S.S. eras analysed using the *Fermi* Bubbles template analysis and the HAP 3D background model.

have already been pointed out in the previous chapter. Except for figure 48 b), this point is placed clearly above the upper limits and also by a factor of two to six higher than the significant points from other analyses But within its large statistical uncertainty (it is only slightly more significant than $2\,\sigma$) it is consistent with previous results.
Furthermore, the HESS I flux points at low energies are higher than for the other analyses, particularly when the std zeta chain is used. In figure 48 b) there are even three significant HESS I differential flux points. These are above the PA as well as the HAP HESS Iu points, but consistent within the uncertainties.

8.9. Stacked analysis results

As a final part of the *Fermi* Bubbles template analysis using the HAP 3D background model, a stacked analysis of the three H.E.S.S. eras is performed. For this purpose, the stacked datasets of the different H.E.S.S. eras are stacked. The overall background of this dataset is then refitted. The residual maps are shown in table 21 for the analysis with the *Fermi*-LAT template. The maps in the top row (summed over all energies) reveal a drastic excess inside the *Fermi*-LAT *Fermi* Bubbles ROI. Between 1 and 10 TeV (bottom row), an excess is observed that resembles the morphology found in the HESS Iu analysis (table 11) for this energy range. Since HESS Iu data have the highest exposure in the region of the expected *Fermi* Bubbles, it is supposed that the stacked analysis shows features similar to the HESS Iu analysis.

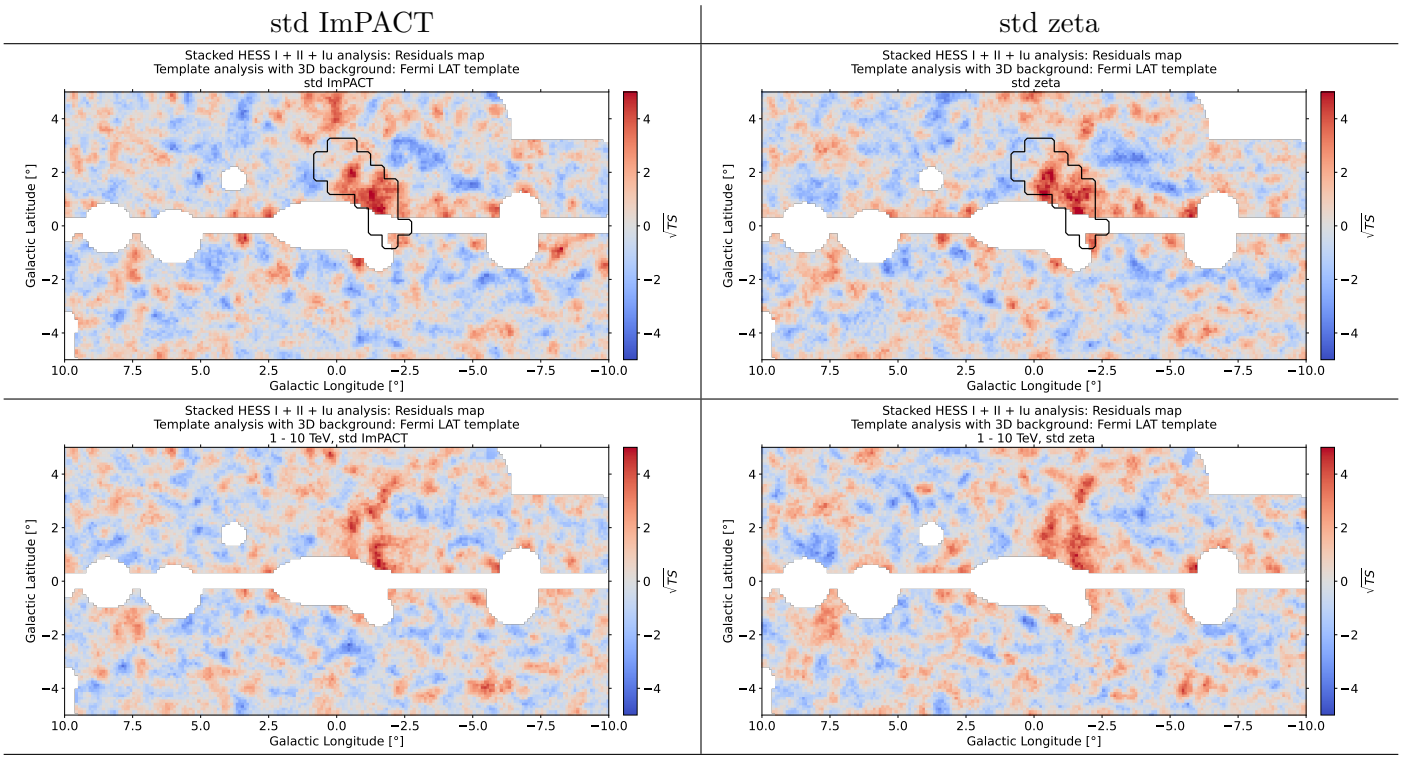

Table 21: *Fermi* Bubbles template analysis using stacked HESS I, II and Iu data: Residual significance maps for the *Fermi* Bubbles template analysis performed with the *Fermi*-LAT template and both std ImPACT and std zeta. Top row: Maps summed over all energies. Bottom row: Maps summed over energies between 1 and 10 TeV.

Additionally, the spectra for both templates as well as for std ImPACT and std zeta are calculated. For the determination of the systematic uncertainty bands using high latitude runs, the results achieved by the analysis of the single eras are stacked. In particular, the fractional residuals are computed using HESS I, II and Iu runs. The same reflected *Fermi* Bubbles template as

in the former HESS I analysis (i.e. as shown in the top left panel of table 19) is used to estimate the systematic uncertainty in the reflected *Fermi* Bubbles region. The resulting spectra are plotted in figure 49. Especially for the analysis with std ImPACT, the achieved results are in very good agreement with the PA flux points. The std zeta analysis shows larger deviations from PA data than the std ImPACT analysis at low energies. In total, the flux points of the stacked analysis resemble the ones from the HESS Iu analysis shown in figure 46 emphasising that the flux data inside the *Fermi* Bubbles ROI are dominated by HESS Iu. The results for the analysis performed with the HESS Iu template can be found in figure E5 in appendix E.5.

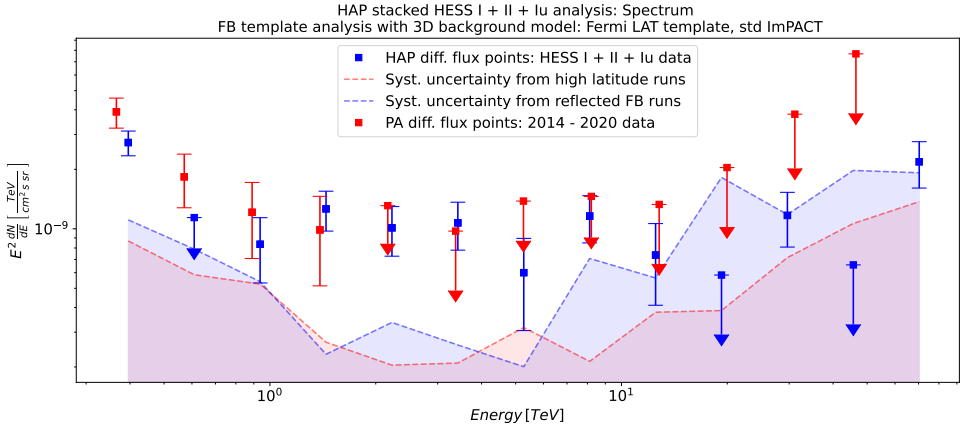

(a) std ImPACT

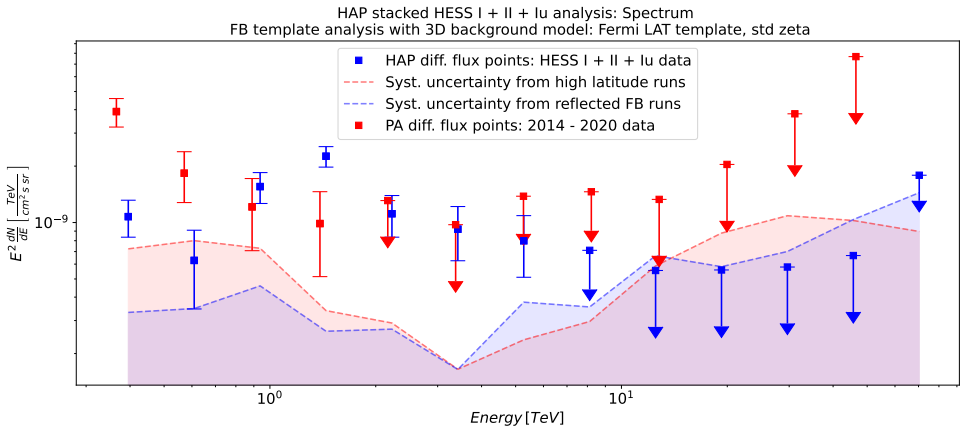

(b) std zeta

Figure 49: Stacked spectra for all H.E.S.S. eras analysed with the template analysis and the HAP 3D background model. Systematic uncertainty bands and PA flux points are added.

9. Analysis of the full ROI (HESS Iu data)

As mentioned in the previous chapter on the *Fermi* Bubbles template analysis, it has not been possible to apply a model to the excess in the *Fermi* Bubbles ROI for HESS Iu data. In this chapter, it is the objective to perform a cross-check of the template analysis. This time, an analysis similar to the one presented in chapter 5 is performed. The idea is to figure out whether the results of the *Fermi* Bubbles template analysis where HGPS sources, CMZ and the GP are completely masked can be also achieved in an analysis where these regions are described by models. The differences to the analysis in chapter 5 are the following:

- Use HESS Iu data instead of HESS I data
- GammaPy v0.19 instead of GammaPy v0.18.2
- Use CS map to model the CMZ excess instead of a diffuse emission template

9.1. Data selection and datasets

Th most important information are summarised as follows:

- H.E.S.S. era: HESS Iu
- ROI: $\pm 10^\circ$ in gal. longitude, $\pm 5^\circ$ in gal. latitude
- Analysis chain: HAP, version hap-18-pl05, tables version Prod05
- std ImPACT and std zeta
- Background model version (std ImPACT): hess_bkg_3d_v07c_fov_radec
- Background model version (std zeta): hess_bkg_3d_v06c_fov_radec
- Analysis software: GammaPy v0.19

The quality cuts are again the same as in chapter 5.1. The number of runs ans the energy thresholds are the same as given in chapter 8.2 for the HESS Iu data.

9.2. Background refitting per observation

For the background refitting, two different masks (for the two different *Fermi* Bubbles templates) are applied. The mask for the *Fermi*-LAT template has been already introduced in chapter 5.3 in figure 17. The mask for the HESS Iu template is shown in figure F1 in appendix F.1. The masked regions are excluded from the background refitting per observation (`mask_fit`).

9.3. Applied models

The models that are applied to the data for a full description of the ROI are mainly the same as in chapter 5.4. However, there a two exceptions regarding the astrophysical sources and the CMZ.

9.3.1. Astrophysical sources

The models of the astrophysical sources are again taken from the HGPS catalog [61]. One model that differs from the analysis in chapter 5.4 is the one of *HESS J1804-216*. In the former analysis with GammaPy v0.18.2, it has been read from the catalog as two single Gaussian spatial with power law spectral models. In the GammaPy v0.19 analysis, it is read as a `TemplateSpatialModel`. Its morphology is shown in figure 50 b). A `PowerLawNormSpectralModel` marks the spectral component.
The free and fixed parameters of the astrophysical sources are the same as in the tables 2 and 3 for sources with point-like and Gaussian-shaped spatial models. In case of *HESS J1731-347* representing the only source with a Shell spatial model, all spatial parameters had to be fixed, since the fit did not converge and showed unreasonable statistics otherwise.

9.3.2. Diffuse emission within the *Central molecular zone*

The second changed model has been already mentioned above: The diffuse emission template introduced in chapter 5.4 is replaced by the CS map [80] around the GC. The CS map is plotted in figure 50 a), it is used as `TemplateSpatialModel`. Since it is normalised to units of sr-1, a simple power law model that turned out to work better than a power law with exponential cutoff is chosen as spectral model.

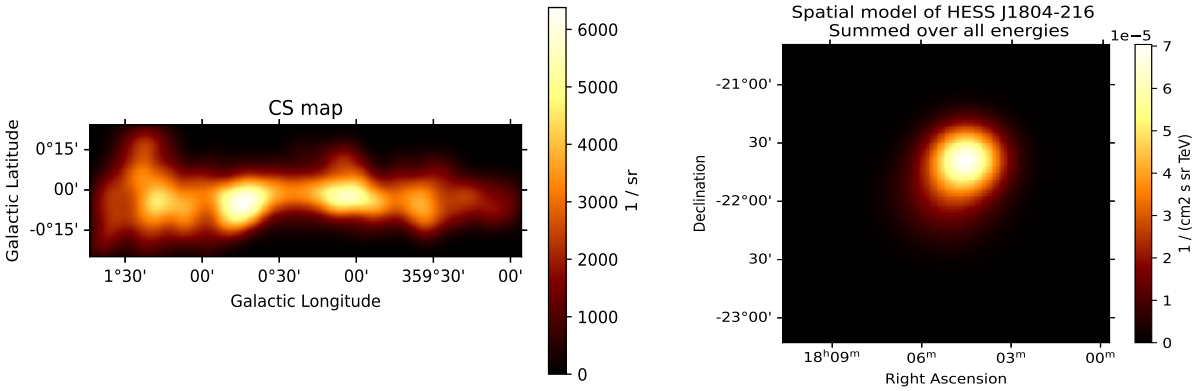

(a) CS map

(b) Spatial model of *HESS J1804-216*

Figure 50: Spatial components of the models that have changed compared to chapter 5.4. The template shown in b) is summed over all energies. For visualisation this does not play any role since its morphology is independent of the energy, even though the relative brightness changes with energy.

The free spectral parameters of the CMZ model are amplitude and index.

9.4. Fit results

The fitting procedure is again divided into two parts: The spatial parameters of the sources are fitted in a first step. Afterwards, the spectral ones are fixed and the spectral ones are fitted. Background normalisation and tilt as well as amplitude and index of the CMZ model are free parameters in both fitting steps. The results of the fit are investigated qualitatively using the residual significance maps shown in table 22.
The first thing to notice here is that there is no striking emission in the CMZ or at the positions of the HGPS sources, i.e. the applied models properly describe the regions. A comparison to the plots in table 11 shows that both sets of maps have the same morphology in the regions

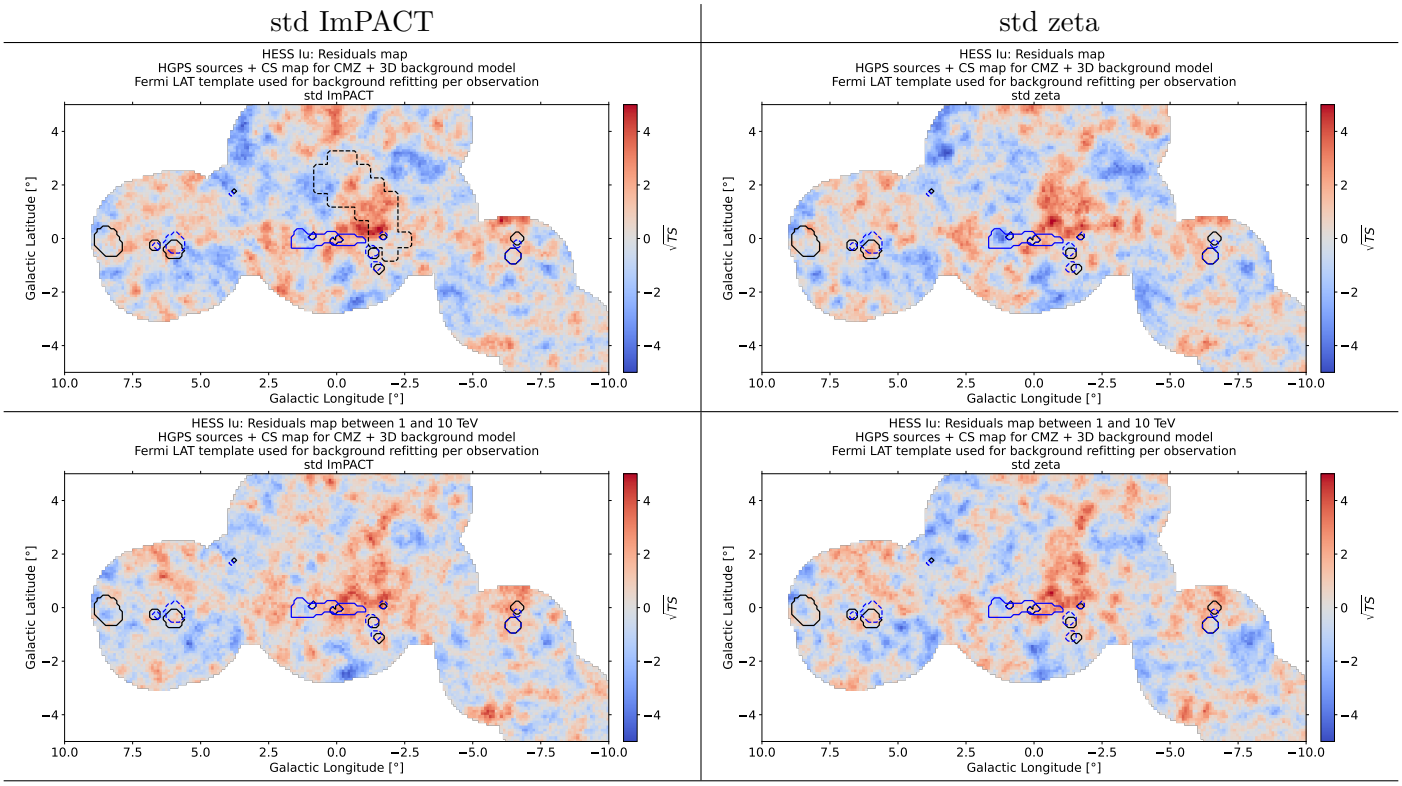

Table 22: HESS Iu analysis of the full ROI: Residual significance maps using the *Fermi*-LAT *Fermi* Bubbles template for background refitting of the single observations. The solid blue contour describes the shape of the CS map. The solid black contours represent the extension of the HGPS sources as given in the catalog, the blue dashed ones their extension after the fitting process. For Gaussian shaped sources, the 1 σ contour is plotted, for point-like ones, an extension of 0.1° is chosen . For visualisation of shell-like sources, the radius parameter is used. Top row: Maps summed over all energies. Bottom row: Maps summed over energies between 1 and 10 TeV.

away from GC and GP. Additional emission in table 22 is observed directly in between the *Fermi* Bubbles ROI and the CMZ. However, this is a promising first check that modelling all the emission regions leads to results that are consistent with the case where all these regions have been masked.

A first more quantitative approach to compare the results from this chapter to the ones from the template analysis is to have a look at the $\sqrt{TS}$ distribution inside the *Fermi* Bubbles ROI. This is exemplary done for the std ImPACT analysis and the *Fermi*-LAT template. The distribution in figure 51 a) is for the map summed over all energies, panel b) for energies between 1 and 10 TeV.

Both, figure 51 a) and b) reveal that the structure of the distributions is the same. In case of the template analysis where HGPS sources, CMZ and GP are completely masked, the distributions are shifted to slightly larger values, but the results nevertheless appear to be consistent. Note that the fit has not converged for std zeta analysis in combination with the HESS Iu template.

9.5. Description of the excess in the *Fermi* Bubbles region via a Gaussian *Fermi* Bubbles model

As a final check, the objective is to describe the observed excess in vicinity of the *Fermi* Bubbles ROI via an explicit model. For the analysis where the full ROI is modelled it turned out that

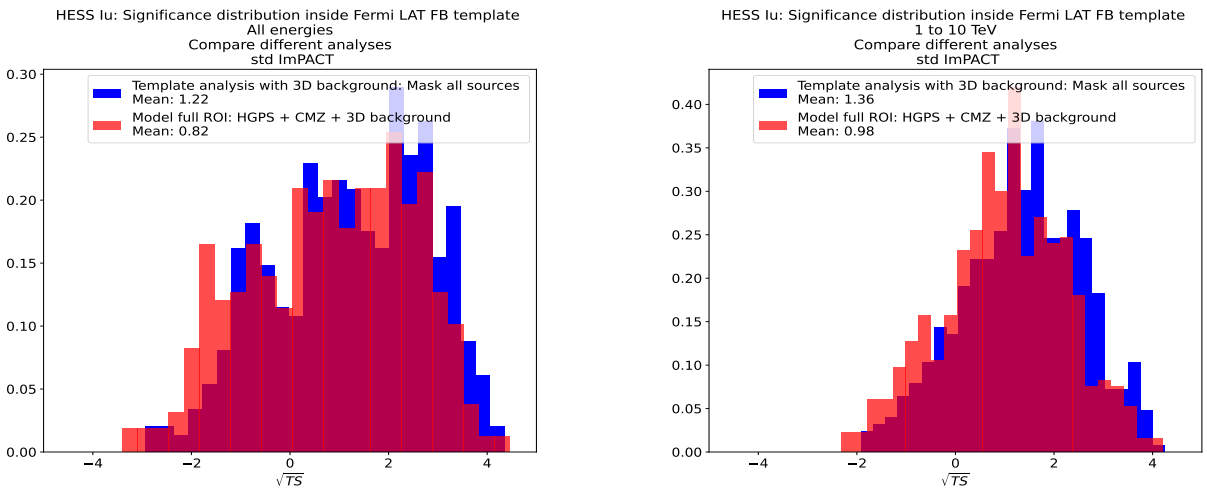

(a) Summed over all energies

(b) 1 - 10 TeV

Figure 51: HESS Iu analysis: Comparison of $\sqrt{TS}$ distributions achieved with and without a mask around HGPS sources, CMZ and GP inside the *Fermi*-LAT *Fermi* Bubbles ROI analysed with std ImPACT for a) all energies and b) energies between 1 and 10 TeV.

it is possible to fit a model to the observed excess. As starting point, a Gaussian spatial model in combination with a power law spectral model with or without exponential cutoff has been chosen. In the course of the fitting procedure, a symmetric Gaussian spatial model together with a power law spectral model with an exponential cutoff worked best for std ImPACT and std zeta. The free parameters of this additional models are the same as shown in table 6 for region 2. The residuals maps with this added *Fermi* Bubbles model are presented in table 23. Having a look at these maps, the remaining emission in the vicinity of the *Fermi* Bubbles ROI is clearly reduced. More quantitatively: When an additional Gaussian model is applied, the significance of the emission in this region can be estimated as $\approx 11\sigma$ using Wilks theorem (as described in chapter 4.4.1.1) for std ImPACT and the *Fermi*-LAT *Fermi* Bubbles template. In this case, there are again six additional degrees of freedom (three spatial and spectral ones). The estimated significance for std zeta and the HESS Iu template are comparable. A minor issue is, however, that the additional Gaussian *Fermi* Bubbles tends to overfit the data, especially if the std zeta algorithm is used. The best-fit parameters of the *Fermi* Bubbles models are printed in appendix F.2 in the tables F2 and F3. The full models of the analysis of the full ROI using HESS Iu data can be found in the folder [22] for std ImPACT, std zeta as well for the *Fermi*-LAT and HESS Iu template that have been masked from the run-wise background refitting. Note that both, the models with and without (previous sub-chapter) the added Gaussian *Fermi* Bubbles model are contained in this folder.
The Gaussian models fitted to the excess in the vicinity of the *Fermi* Bubbles ROI differ from the models that have been used to describe region 1 in chapter 6 (see e.g. tables B1 and B2). Not only the type of spectral models that is used is different, also the position and shape of the Gaussian spatial models show large variations. In first place, the Gaussian model describing region 1 is shifted $\approx 0.7°$ down in latitude compared to the one found in the description of HESS Iu data. Furthermore, its extension is larger by almost a factor of three. Particularly, the connection of the excess detected in region 1 and the *Fermi* Bubbles is still not clear.

[22] `https://github.com/fabian-richter/HESS_HAP_extended_emission_and_FB/tree/main/Modelling_of_the_full_ROI/HESS_Iu/models`

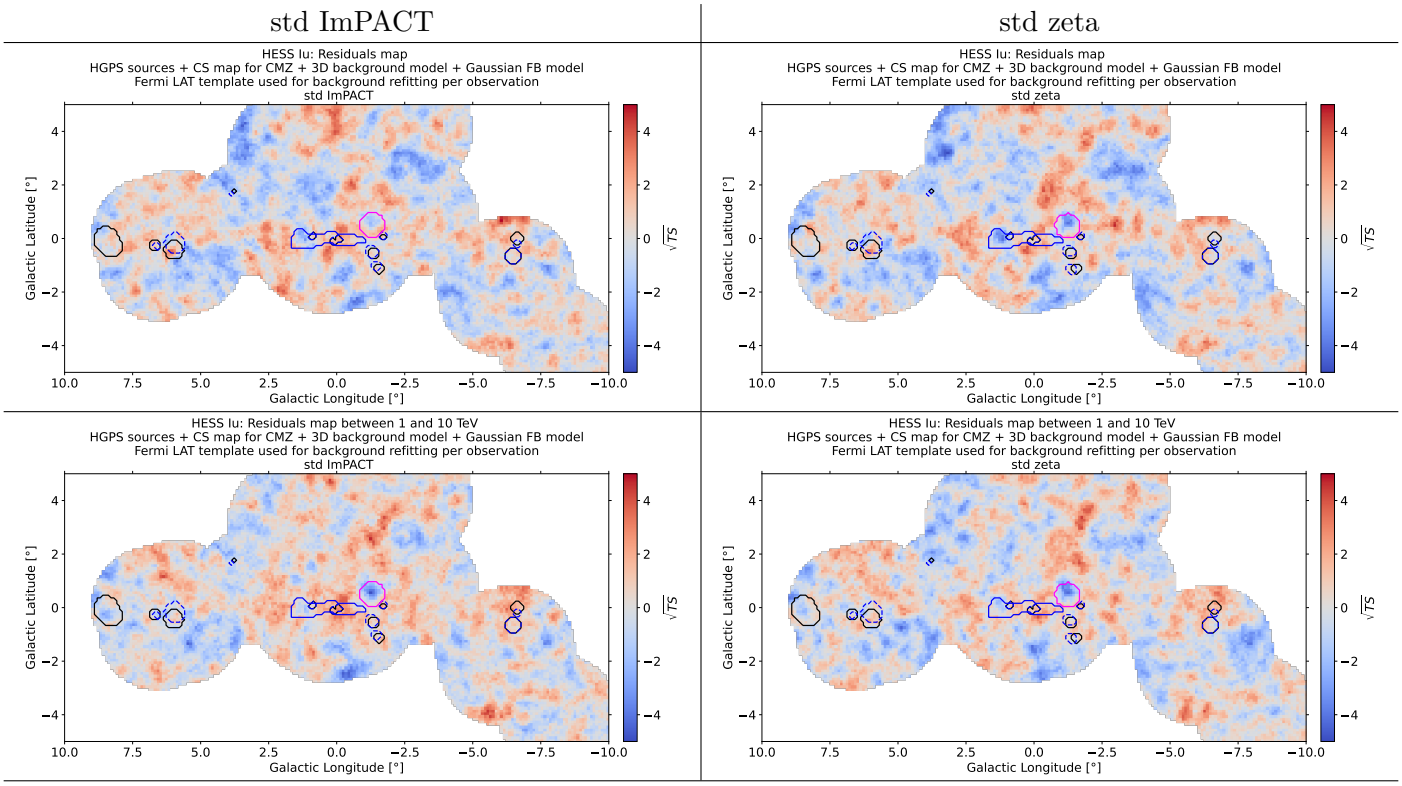

Table 23: HESS Iu analysis of the full ROI: Residual significance maps using the *Fermi*-LAT *Fermi* Bubbles template for background refitting of the single observations. Top row: Maps summed over all energies. Bottom row: Maps summed over energies between 1 and 10 TeV. The 1 σ region of the additional Gaussian model is represented by the magenta solid contour. The remaining colour code is the same as in table 22.

9.6. Comparison of the spectra from the full ROI analysis and template analysis

As a cross-check of the *Fermi* Bubbles template analysis, spectra for the datasets where HGPS sources, CMZ and the additional Gaussian *Fermi* Bubbles models are used to describe the data are calculated and compared to previous results. Therefore, two approaches, that are discussed in more detail in the following lines, are used.

9.6.1. Addition of the intensity of the *Fermi* Bubbles model and the remaining residuals within the *Fermi* Bubbles ROI

For this purpose, the intensity map of the *Fermi* Bubbles model is calculated using inbuilt Gammapy functionalities. This map contains the intensity of the *Fermi* Bubbles model for each energy bin separately. It is then multiplied by the mask of the *Fermi* Bubbles templates (either *Fermi*-LAT or HESS Iu) such that the area that is taken into account for the calculation of the spectra is the same as in the template analysis. The intensity map (for visualisation summed over all energies) of the *Fermi* Bubbles model is exemplary shown for std ImPACT and the *Fermi*-LAT template in figure 52 a) inside the full ROI. Sub-figure b) shows the same map, but only inside the *Fermi*-LAT *Fermi* Bubbles ROI. As the CMZ and a stripe along the GP have been masked in the template analysis, these regions are masked in the intensity map to ensure consistency.
The last step is to add up the *Fermi* Bubbles model intensity and the intensity of the remaining residuals computed as in equation (33) with the exception that predicted event counts and not

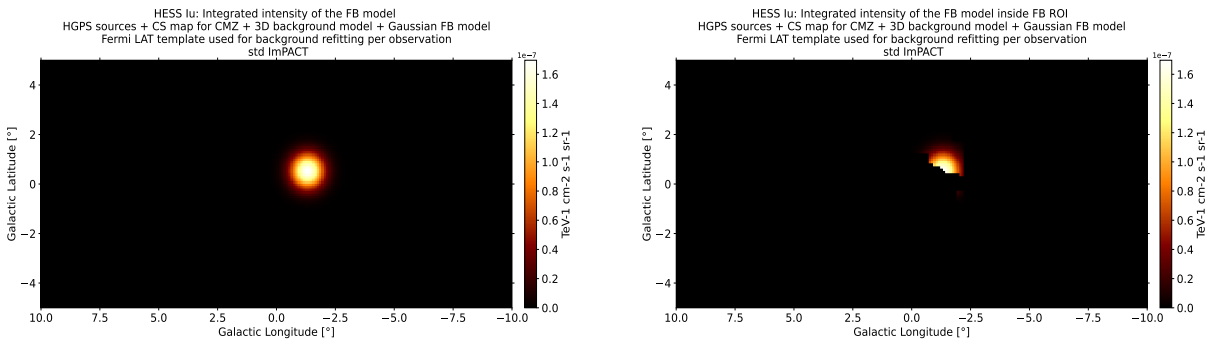

(a) Full ROI

(b) Inside the *Fermi* Bubbles ROI

Figure 52: Intensity maps of the *Fermi* Bubbles model summed over all energies for std ImPACT reconstruction and the *Fermi*-LAT template.

background model counts are subtracted from the detected counts, since the background model is not exclusively applied. The spectra achieved using this approach are compared to the ones of the template analysis in figure 53.
Especially the results for std ImPACT analysis and *Fermi*-LAT template (panel a)) are in good agreement. The same holds for the *Fermi*-LAT template analysis in combination with the std zeta reconstruction algorithm. Panel c) reveals that the agreement of the template analysis and the analysis with the Gaussian *Fermi* Bubbles model is worse when using the HESS Iu template compared to the Fermi LAT template. This effect may occur since the HESS Iu template extends to higher latitudes than the *Fermi*-LAT template and the *Fermi* Bubbles model. In particular, the intensity of the *Fermi* Bubbles model in the HESS Iu *Fermi* Bubbles ROI is rather low which can explain that the flux determined from the Gaussian *Fermi* Bubbles model and added residuals is below the one of the template analysis for most of the points.

9.6.2. Calculation of the differential flux points of the *Fermi* Bubbles model

The second approach is to directly compute the differential flux points of the *Fermi* Bubbles model. Therefore, the `FluxPointsEstimator` implemented in GammaPy is used. The energy binning for calculation of the flux points has been chosen identically as for the template analysis. The differential flux points from the `FluxPointsEstimator` return the results for the full containment of the Gaussian spatial model in units of TeV cm-2 s-1. These flux points are taken as a starting point. Within different containment regions of the Gaussian the spectra are then computed, i.e. the flux points are multiplied by the containment and divided by the area of these regions. Therefore, the 1.5σ (68 % containment) and 3σ (99 % containment) regions have been chosen. A short summary of the properties of these containment regions and the *Fermi* Bubbles templates are given in table 24. The area given for the *Fermi*-LAT template takes into account that is partially overlaid with the mask along the GP and thus does not contribute to the analysis with its full area.

Table 24: Properties of the containment regions of the Gaussian *Fermi* Bubbles models.

Algorithm + template	1.5 σ area in sr	3 σ area in sr	$\Delta\Omega_{FB}$ in sr
std ImPACT + *Fermi*-LAT	$5.1 \cdot 10^{-4}$	$2.1 \cdot 10^{-3}$	$1.6 \cdot 10^{-3}$
std ImPACT + HESS Iu	$5.2 \cdot 10^{-4}$	$2.0 \cdot 10^{-3}$	$1.2 \cdot 10^{-3}$
std zeta + *Fermi*-LAT	$5.3 \cdot 10^{-4}$	$2.1 \cdot 10^{-3}$	$1.6 \cdot 10^{-3}$

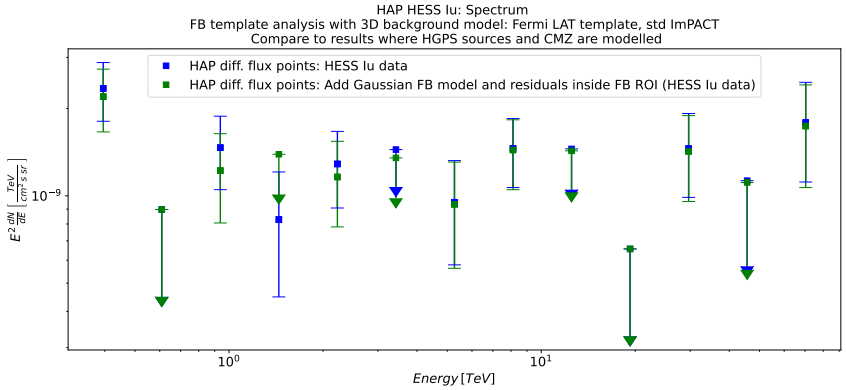

(a) std ImPACT + *Fermi*-LAT template

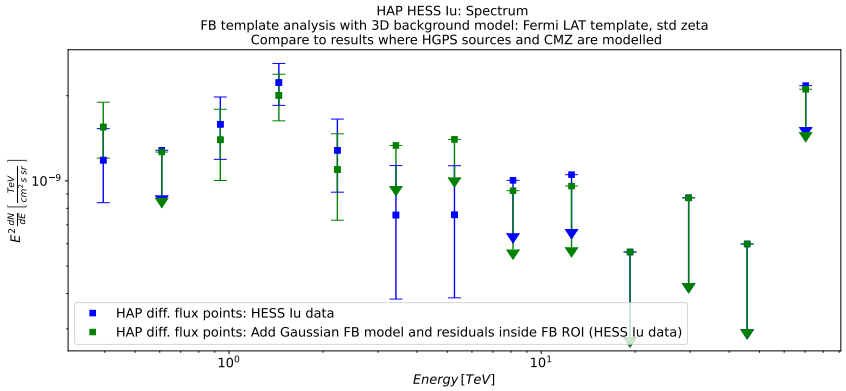

(b) std zeta + *Fermi*-LAT template

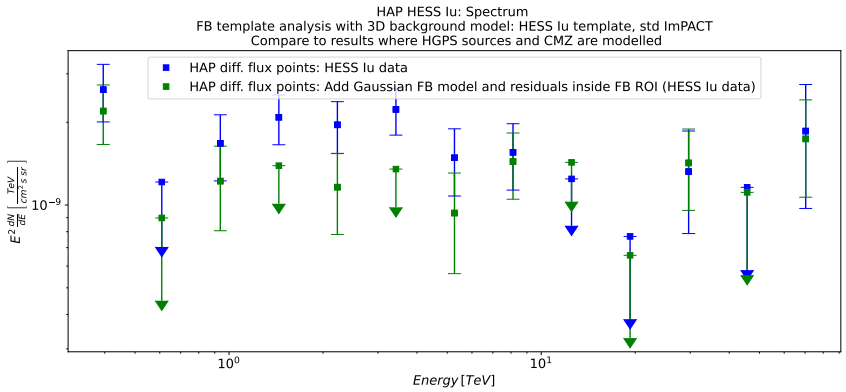

(c) std ImPACT + HESS Iu template

Figure 53: HESS Iu spectra: Differential flux points determined from added intensity of the Gaussian *Fermi* Bubbles model and the remaining residuals inside the *Fermi* Bubbles ROI compared to the results of the template analysis.

Inspecting the values in table 24, one finds that the area of the 3σ Gaussian containment is comparable to the one of the *Fermi*-LAT template indicating that the 3σ containment region may achieve results consistent with the ones from template analysis. This expected consistency for the *Fermi*-LAT template is observed in figure 54. In panel a), the flux points from the 3σ Gaussian region are almost perfectly overlaying the ones from the template analysis up to $\approx$ 10 TeV. At higher energies, the *Fermi* Bubbles model shows the expected cutoff (since the power law spectral model with exponential cutoff has been chosen) that is not observed in the spectrum of the template analysis. For the std zeta analysis and the *Fermi*-LAT template (panel c)), the flux of the *Fermi* Bubbles model shows even a steeper drop at high energies, but is also consistent with the results of the template analysis up to $\approx$ 10 TeV. Furthermore, an agreement for the HESS Iu template is found (panel c)). The differential flux points of the 1.5σ Gaussian region are clearly above the ones from template analysis for all investigated cases which may be related to the relatively small areas of these regions around the brightest spots of the Gaussian *Fermi* Bubbles models.
Finally, for HESS Iu data, the results of the analysis where the full ROI is modelled and a *Fermi* Bubbles model is added, are consistent with the *Fermi* Bubbles template analysis. This demonstrates on the one hand that the template analysis with the 3D background model is a reasonable approach and on the other hand that the description of the full ROI using the different models works properly.

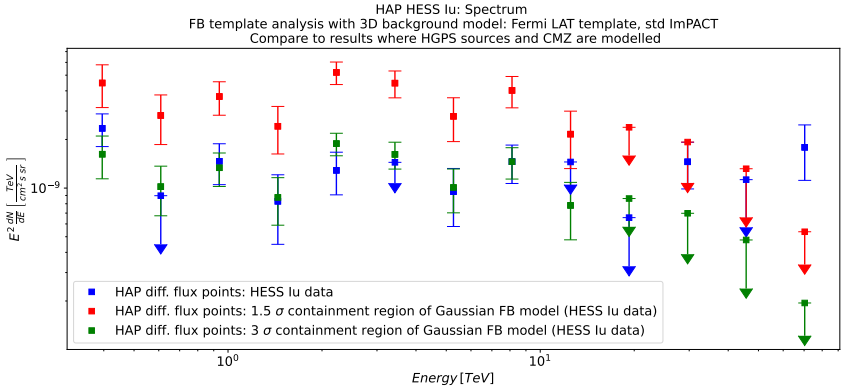

(a) std ImPACT + *Fermi*-LAT template

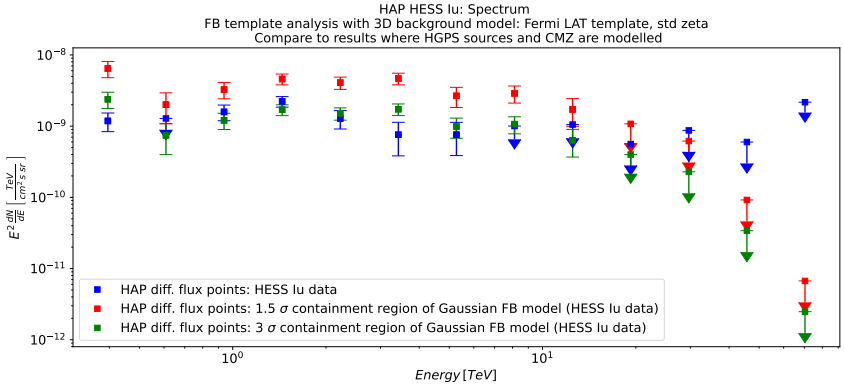

(b) std zeta + *Fermi*-LAT template

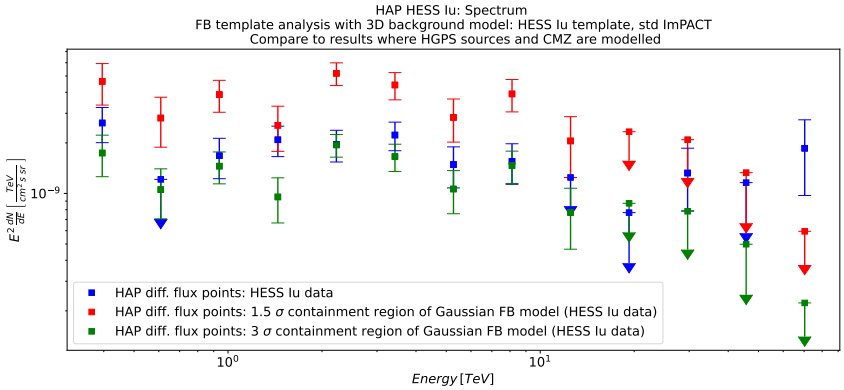

(c) std ImPACT + HESS Iu template

Figure 54: HESS Iu spectra: Differential flux points of the *Fermi* Bubbles model determined with the `FluxPointsEstimator` for different containment regions compared to the results of the template analysis.

10. Conclusion and outlook

In the first part of this thesis, it was searched for indications for *Fermi* Bubbles emission in HESS I data. Since the emission (if detected) is not necessarily spatially coincident with the emission detected with *Fermi*-LAT , an analysis of a ROI ranging from $\pm 10^\circ$ in galactic longitude and $\pm 5^\circ$ in galactic latitude was performed. All the sources known for strong γ-ray emission in this ROI, i.e. HGPS sources and CMZ, were modelled. Three remaining regions with large-scale emission were detected. Afterwards, these regions were described by simple Gaussian spatial models as a starting point. These models revealed a proper description of all three regions. The analysis was refined replacing the Gaussian spatial models by hydrogen templates. Especially for region 2, i.e. the region at $\approx 353^\circ$ in galactic longitude and above the HGPS sources *HESS J1729-345* and *HESS J1731-347* in galactic latitude showed a clear correlation with the molecular hydrogen column density.

However, the most interesting region regarding the *Fermi* Bubbles analysis was region 1 located in the GP and centred at a galactic longitude of $\approx 358^\circ$. This region shows a spatial coincidence with the base of the *Fermi* Bubbles as observed in *Fermi*-LAT data at latitudes $|b| < 1^\circ$. At higher latitudes, where the brightness in the *Fermi*-LAT map is comparable to the brightness at zero latitude, there is no remarkable signal detected in HESS I data. This may be related to the HESS I exposure that decreases with increasing distance to the GC and consequently also at higher latitudes. Interestingly, a simple power law spectrum described the data in this region better than a model with exponential cutoff, i.e. no cutoff is observed in the data.

The main *Fermi* Bubbles analysis presented in this thesis was performed using HESS Iu data and a mask around HGPS sources and CMZ as well as along the GP. std ImPACT and std zeta algorithms were used for background reconstruction. For this *Fermi* Bubbles template analysis, the HAP 3D background model was the only applied model. Furthermore, the spectra of the data inside the *Fermi*-LAT *Fermi* Bubbles ROI were calculated. Based on the std ImPACT residuals in this energy range found in the HAP HESS Iu analysis, the HESS Iu *Fermi* Bubbles template was defined as a cross-check. The results for both templates are consistent within the uncertainties.

In addition, various uncertainty studies were performed. Fractional residuals in an energy range between 1 and 10 TeV were calculated inside and outside the *Fermi*-LAT or HESS Iu data-based *Fermi* Bubbles ROI as well as in a reflected *Fermi* Bubbles ROI. The results revealed an excess in the fractional residuals of $\gtrsim 3.5\,\sigma$ up to $\approx 9\,\sigma$ depending on the used *Fermi* Bubbles template and background reconstruction algorithm.

Furthermore, it was shown that the signal in the *Fermi* Bubbles ROI nearly shows square root behaviour as function of fractional exposure in the *Fermi* Bubbles ROI. This gives a hint that the observed signal is very likely not dominated by single observations where background mismodelling occurred. The background model turned out to be robust regarding manipulation of the background data at energies above ≈ 1 TeV. At energies below 1 TeV, the results are stable for an introduced uncertainty of a few percent per degree. At higher uncertainties, i.e. 10 %, the result becomes distorted. Adding a spatial tilt in galactic longitude and latitude to the standard background model showed that the spatial tilt is dominated by the low energies and only showed slight variations at energies above 1 TeV. This reaffirmed the result of the previous background studies.

Systematic uncertainties were estimated using high latitude runs and data in a reflected *Fermi* Bubbles ROI. These systematic uncertainties were then visualised via contour bands in the spectral plots achieved using the *Fermi* Bubbles template analysis.

The results from the HAP analysis are consistent with the ones from PA analysis with 2014 to 2020 H.E.S.S. data. In contrast to latter, a statistically significant signal is observed at energies

between 1 and 10 TeV using std ImPACT as well as std zeta. In case of the std ImPACT analysis, this signal is well above the systematic uncertainty curve in this energy range. However, the systematic uncertainties determined in the std zeta analysis are in the same order of magnitude as the signal, i.e. the signal may be dominated by systematics. Neither for the std ImPACT nor the std zeta analysis, a cutoff in the spectrum is observed. Predicting a cutoff based on the used data is very difficult since there are low statistics and large systematic uncertainties at high energies.

The *Fermi* Bubbles template analysis was repeated for HESS I and II data. These analyses mainly revealed upper limits that are consistent with the HAP HESS Iu and PA spectra. As a last check of the *Fermi* Bubbles template analysis, the datasets of the different H.E.S.S. eras were stacked and analysed together. The determined spectra of this analysis were similar to the ones achieved in the HESS Iu analysis and are in good agreement with the PA data. This was expected as the HESS Iu IGS runs mainly pointed to the close vicinity of the *Fermi* Bubbles, while HESS I and II mostly covered the GC.

In the last part of this thesis, all sources in the full ROI ($\pm 10^\circ$ in galactic longitude and $\pm 5^\circ$ in galactic latitude) were modelled for HESS Iu data. The consistency of the results where the full ROI has been modelled and the *Fermi* Bubbles template analysis was checked. The spectra for both methods achieved in the *Fermi*-LAT *Fermi* Bubbles ROI are consistent indicating that the models of the γ-ray emitting sources are a proper description of the data. On the other hand, it is a reasonable approach to mask all the strong sources in the ROI and to only apply the 3D background model.

One possibility to improve the analysis results, especially at low energies, is to perform similar analyses using *Fermi*-LAT data and to joint-fit the data in Gammapy. Moreover, the upcoming Cherenkov Telescope Array (CTA) will have an improved energy and angular resolution which will allow for a more detailed study of the *Fermi* Bubbles in a broader energy range. Beyond the scope of this thesis is the physical modelling of the *Fermi* Bubbles.

Bibliography

[1] Victor F. Hess. Über Beobachtungen der durchdringenden Strahlung bei sieben Freiballonfahrten. *Physik. Zeitschr.*, XIII:1084–1091, 1912. URL: https://www.mpi-hd.mpg.de/hfm/HESS/public/HessArticle.pdf.

[2] Victor F. Hess – Biographical. NobelPrize.org. Nobel Prize Outreach AB 2022. https://www.nobelprize.org/prizes/physics/1936/hess/biographical/. [Online; Accessed: June 28, 2022].

[3] T. K. Gaisser, R. Engel, and E. Resconi. *Cosmic Rays and Particle Physics*. Cambridge University Press, 2 edition, 2016. doi:10.1017/CBO9781139192194.

[4] M. Thomson. *Modern Particle Physics*. Cambridge University Press, 2013. doi:10.1017/CBO9781139525367.

[5] Fermi Gamma-ray Space Telesope, NASA. https://fermi.gsfc.nasa.gov/science/overview.html. [Online; Accessed: June 28, 2022].

[6] H.E.S.S. collaboration: High Energy Stereoscopic System. https://www.mpi-hd.mpg.de/hfm/HESS/. [Online; Accessed: June 28, 2022].

[7] G. Dobler et al. The Fermi haze: A gamma-ray counterpart to the microwave haze. *The Astrophysical Journal*, 717:825–842, 2010. URL: https://iopscience.iop.org/article/10.1088/0004-637X/717/2/825, doi:10.1088/0004-637X/717/2/825.

[8] M. Su, D. Finkbeiner, and T. Slatyer. Giant gamma-ray bubbles from Fermi-Lat: Active galactic nucleus activity or bipolar galactic wind? . *The Astrophysical Journal*, 724:1044–1082, 2010. URL: https://iopscience.iop.org/article/10.1088/0004-637X/724/2/1044, doi:10.1088/0004-637X/724/2/1044.

[9] M. Ackermann et al. the spectrum and morphology of the Fermi bubbles. *The Astrophysical Journal*, 793:64 (34pp), 2014. URL: https://iopscience.iop.org/article/10.1088/0004-637X/793/1/64, doi:10.1088/0004-637X/793/1/64.

[10] S. L. Snowden et al. Rosat survey diffuse x-ray background maps. II. *The Astrophysical Journal*, 485:125–135, 1997. URL: https://www.researchgate.net/publication/253509468_ROSAT_survey_diffuse_X-ray_background_maps_2, doi:http://dx.doi.org/10.1086/304399.

[11] R. Crocker et al. A unified model of the fermi bubbles, microwave haze, and polarized radio lobes: Reverse shocks in the galactic center's giant outflows. *The Astrophysical Journal*, 808(2):107, jul 2015. URL: https://iopscience.iop.org/article/10.1088/0004-637X/808/2/107, doi:10.1088/0004-637x/808/2/107.

[12] NASA's Fermi Telescope Finds Giant Structure in our Galaxy. https://www.nasa.gov/mission_pages/GLAST/news/new-structure.html. [Online; Accessed: June 28, 2022].

[13] P. Mertsch and S. Sarkar. Fermi gamma-ray "bubbles" from stochastic acceleration of electrons. *Phys. Rev. Lett.*, 107:091101, Aug 2011. URL: https://link.aps.org/doi/10.1103/PhysRevLett.107.091101, doi:10.1103/PhysRevLett.107.091101.

[14] M. Ackermann et al. The Fermi Galactic Center GeV Excess and Implications for Dark Matter. *The Astrophysical Journal*, 849:3 (34pp), 2017. URL: https://iopscience.iop.

org/article/10.3847/1538-4357/aa6cab, doi:https://doi.org/10.3847/1538-4357/aa6cab.

[15] C. Grupen. *Astroparticle Physics*. Springer, 2 edition, 2020. doi:https://doi.org/10.1007/978-3-030-27339-2.

[16] G. Dobler. A last look at the microwave haze/bubbles with WMAP. *The Astrophysical Journal*, 750:17 (8pp), 2012. URL: https://iopscience.iop.org/article/10.1088/0004-637X/750/1/17, doi:10.1088/0004-637X/750/1/17.

[17] D. Malyshev. Fermi bubbles: an elephant in the gamma-ray sky. *EPJ Web of Conferences*, 136:03011, 04 2017. arXiv:1704.02629, doi:10.1051/epjconf/201713603011.

[18] A. Fox et al. Probing the Fermi bubbles in ultraviolet absorption: a spectroscopic signature of the Milky Way's biconical nuclear outflow . *The Astrophysical Journal*, 799:L7 (6pp), 2015. URL: https://iopscience.iop.org/article/10.1088/2041-8205/799/1/L7, doi:10.1088/2041-8205/799/1/L7.

[19] K.-S. Cheng, D. O. Chernyshov, V. A. Dogiel, C.-M. Ko, and W.-H. Ip. ORIGIN OF THE FERMI BUBBLE. *The Astrophysical Journal*, 731(1):L17, mar 2011. doi:10.1088/2041-8205/731/1/l17.

[20] R. M. Crocker and F. Aharonian. Fermi bubbles: Giant, multibillion-year-old reservoirs of galactic center cosmic rays. *Phys. Rev. Lett.*, 106:101102, Mar 2011. URL: https://link.aps.org/doi/10.1103/PhysRevLett.106.101102, doi:10.1103/PhysRevLett.106.101102.

[21] H.-Y.K. Yang, M. Ruszkowski, and E.G. Zweibel. Unveiling the origin of the fermi bubbles. *Galaxies*, 6:29, 2018. URL: https://www.mdpi.com/2075-4434/6/1/29, doi:10.1103/PhysRevLett.106.101102.

[22] F. Guo and W. Mathews. The Fermi Bubbles. I. Possible Evidence for Recent AGN Jet Activity in the Galaxy. *The Astrophysical Journal*, 756:181 (17pp), Sep 2012. doi:10.1088/0004-637X/756/2/181.

[23] F. Guo, W. Mathews, G. Dobler, and S. Pengh Oh. The Fermi Bubbles. II. The potential roles of viscosity and cosmic-ray diffusion in jet models. *The Astrophysical Journal*, 756:182 (14pp), Sep 2012. doi:10.1088/0004-637X/756/2/182.

[24] B.R. McNamara and P.E.J. Nulsen. Heating Hot Atmospheres with Active Galactic Nuclei. *Annual Review of Astronomy and Astrophysics*, 45:117–175, May 2007. doi:10.1146/annurev.astro.45.051806.110625.

[25] NASA web page: Hubble Space Telescope. https://www.nasa.gov/mission_pages/hubble/science/hercules-a.html. [Online; Accessed: June 28, 2022].

[26] D. Cox. The Three-Phase Interstellar Medium Revisited. *Annual Review of Astronomy and Astrophysics*, 43:337–385, Sep 2005. doi:10.1146/annurev.astro.43.072103.150615.

[27] J. Bland-Hawthorn, S. Veilleux, and G. Cecil. Galactic winds: a short review. *Astrophysics and Space Science*, 311(1-3):87–98, October 2007. doi:10.1007/s10509-007-9567-8.

[28] D. Strickland, T. Ponman, and I. Stevens. Rosat observations of the galactic wind in m82. 1996. URL: https://arxiv.org/abs/astro-ph/9608064, doi:10.48550/ARXIV.ASTRO-PH/9608064.

[29] T. Paumard et al. The Two Young Star Disks in the Central Parsec of the Galaxy: Properties, Dynamics, and Formation. *The Astrophysical Journal*, 643:1011–1035, Jun 2006. arXiv:astro-ph/0601268, doi:10.1086/503273.

[30] ESA web page: XMM-NEWTON'S VIEW OF MESSIER 82 (X-RAY/OPTICAL/UV). https://sci.esa.int/web/iya/-/44613-messier-82-with-xmm-newton-x-ray-optical-uv. [Online; Accessed: June 28, 2022].

[31] K. Zubovas, A.R. King, and S. Nayakshin. The Milky Way's Fermi bubbles: echoes of the last quasar outburst? *Monthly Notices of the Royal Astronomical Society*, 415:21–25, Jul 2011. URL: https://academic.oup.com/mnrasl/article/415/1/L21/965171, doi:10.1111/j.1745-3933.2011.01070.x.

[32] M. Su and D. Finkbeiner. EVIDENCE FOR GAMMA-RAY JETS IN THE MILKY WAY. *The Astrophysical Journal*, 753(1):61, jun 2012. doi:10.1088/0004-637x/753/1/61.

[33] Personal communication with Alessandro Montanari.

[34] J. Matthews. A Heitler model of extensive air showers. *Astroparticle Physics*, 22:387–397, 2005. URL: http://particle.astro.ru.nl/ps/astropart1415-wk7a.pdf, doi:10.1016/j.astropartphys.2004.09.003.

[35] H. J. Völk and K. Bernlöhr. Imaging very high energy gamma-ray telescopes. *Experimental Astronomy*, 25(1-3):173–191, Mar 2009. URL: http://dx.doi.org/10.1007/s10686-009-9151-z, arXiv:0812.4198, doi:10.1007/s10686-009-9151-z.

[36] M. de Naurois and D. Mazin. Ground-based detectors in very-high-energy gamma-ray astronomy. *Comptes Rendus Physique*, 16(6-7):610–627, Aug 2015. URL: http://dx.doi.org/10.1016/j.crhy.2015.08.011, arXiv:1511.00463, doi:10.1016/j.crhy.2015.08.011.

[37] W.R. Leo. *Techniques for Nuclear and Particle Physics Experiments*. Springer-Verlag Berlin Heidelberg GmbH, 2 edition, 1994.

[38] W. Heitler. *The Quantum Theory Of Radiation*. Dover Publications, 1954.

[39] M. Barranets et al. Atmospheric corrections of the cosmic ray fluxes detected by the solar neutron telescope at the summit of the sierra negra volcano in mexico. *Geofísica Internacional*, 57:253–275, 10 2018. doi:10.22201/igeof.00167169p.2018.57.4.2105.

[40] P.A. et al. Zyla. Review of Particle Physics. *PTEP*, 2020(8):083C01, 2020. doi:10.1093/ptep/ptaa104.

[41] V.L. Ginzburg. Radiation by uniformly moving sources (vavilov - cherenkov effect, transition radiation, and other phenomena). *Phys.-Usp.*, 39(10):973–982, 1996. URL: https://iopscience.iop.org/article/10.1070/PU1996v039n10ABEH000171.

[42] ECAP: The High Energy Stereoscopic System. https://ecap.nat.fau.de/index.php/research/gamma-ray-astronomy/h-e-s-s/. [Online; Accessed: June 28, 2022].

[43] A. M. Hillas. Cerenkov Light Images of EAS Produced by Primary Gamma Rays and by Nuclei. In *19th International Cosmic Ray Conference (ICRC19), Volume 3*, volume 3 of *International Cosmic Ray Conference*, page 445, August 1985. URL: https://ui.adsabs.harvard.edu/abs/1985ICRC....3..445H.

[44] R.D. Parsons and J.A. Hinton. A monte carlo template based analysis for air-cherenkov arrays. *Astroparticle Physics*, 56:26–34, Apr 2014. URL: http://dx.doi.org/10.1016/j.astropartphys.2014.03.002, doi:10.1016/j.astropartphys.2014.03.002.

[45] F. Aharonian et al. Observations of the crab nebula with hess. *Astronomy & Astrophysics*, 457(3):899–915, 2006. doi:10.1051/0004-6361:20065351.

[46] K. Bernlöhr. Simulation of imaging atmospheric cherenkov telescopes with corsika and sim_telarray. *Astroparticle Physics*, 30(3):149–158, 2008. URL: https://www.sciencedirect.com/science/article/pii/S0927650508000972, doi:https://doi.org/10.1016/j.astropartphys.2008.07.009.

[47] B. Khelifi et al. HAP-Fr, a pipeline of data analysis for the HESS-II experiment. In *34th International Cosmic Ray Conference*, volume ICRC2015, page 837, The Hague, Netherlands, July 2015. URL: https://hal.archives-ouvertes.fr/hal-01584586, doi:10.22323/1.236.0837.

[48] LAT IRFs (Instrument Response Functions). https://www.slac.stanford.edu/exp/glast/wb/prod/pages/sciTools_overview/overview_IRF.htm. [Online; Accessed: June 28, 2022].

[49] Gammapy v0.18.2 documentation. https://docs.gammapy.org/0.18.2/. [Online; Accessed: June 28, 2022].

[50] L. Mohrmann et al. Validation of open-source science tools and background model construction in astronomy. *Astronomy & Astrophysics*, 632:A72, 2019. doi:10.1051/0004-6361/201936452.

[51] Personal communication with Andreas Specovius.

[52] Gammapy v0.18.2 documentation: Shell spatial model. https://docs.gammapy.org/0.18.2/modeling/gallery/spatial/plot_shell.html#shell-spatial-model. [Online; Accessed: June 28, 2022].

[53] Gammapy v0.18.2 documentation: Gaussian spatial model. https://docs.gammapy.org/0.18.2/modeling/gallery/spatial/plot_gauss.html#gaussian-spatial-model. [Online; Accessed: June 28, 2022].

[54] G. Cowan. *Statistical Data Analysis*. Oxford science publications, 1998.

[55] L. Mohrmann. *Characterizing cosmic neutrino sources*. PhD thesis, Humboldt-Universität zu Berlin, Mathematisch-Naturwissenschaftliche Fakultät, 2015. doi:http://dx.doi.org/10.18452/17377.

[56] W. Cash. Parameter estimation in astronomy through application of the likelihood ratio. *The Astrophysical Journal*, 228:939–947, March 1979. doi:10.1086/156922.

[57] S. Algeri et al. Searching for new phenomena with profile likelihood ratio tests. *Nat Rev Phys*, 2:245–252, 2020. URL: https://www.nature.com/articles/s42254-020-0169-5, doi:10.1038/s42254-020-0169-5.

[58] S. S. Wilks. The large-sample distribution of the likelihood ratio for testing composite hypotheses. *The Annals of Mathematical Statistics*, 9(1):60–62, 1938. URL: http://www.jstor.org/stable/2957648.

[59] Bin-by-bin Likelihood Profiles. https://gamma-astro-data-formats.readthedocs.io/en/latest/spectra/binned_likelihoods/index.html. [Online; Accessed: June 28, 2022].

[60] Personal communication with Dmitry Malyshev.

[61] H.E.S.S. Collaboration. The H.E.S.S. Galactic plane survey. *Astronomy & Astrophysics*, 612:A1 (61 pp.), Apr 2018. URL: https://www.aanda.org/articles/aa/full_html/2018/04/aa32098-17/aa32098-17.html, doi:10.1051/0004-6361/201732098.

[62] TeVCat gamma-ray source HESS J1804-216. http://tevcat.uchicago.edu/?mode=1;id=113. [Online; Accessed: June 28, 2022].

[63] H.E.S.S. Collaboration: A. Abramowski et al. Acceleration of petaelectronvolt protons in the Galactic Centre. *Nature*, 531:476–479, 2016. doi:10.1038/nature17147.

[64] H.E.S.S. Collaboration: H. Abdalla et al. Characterising the VHE diffuse emission in the central 200 parsecs of our Galaxy with H.E.S.S. *Astronomy & Astrophysics*, 612:A9 (13 pp.), 2018. doi:10.1051/0004-6361/201730824.

[65] Personal communication with Yu Wun Wong.

[66] Status on Diffuse Emission in GC. https://hess-confluence.desy.de/confluence/display/HESS/2021+April+virtual+collaboration+meeting?preview=/241303560/255590405/2021-04-30-wong_gc_hess.pdf. Presentation by Yu Wun Wong at HESS Collaboration Meeting on April 30, 2021 (only available for Confluence members), Online; Accessed: June 28, 2022.

[67] H. Suzuki et al. Uniform distribution of the extremely overionized plasma associated with the supernova remnant G359.1-0.5. *The Astrophysical Journal*, 893(2):147, apr 2020. doi:10.3847/1538-4357/ab80ba.

[68] Y. Cui, G. Pühlhofer, and A. Santangelo. A young supernova remnant illuminating nearby molecular clouds with cosmic rays. *A&A*, 591:A68, 2016. doi:10.1051/0004-6361/201628505.

[69] H.E.S.S. Collaboration and Abramowski, A. A new snr with tev shell-type morphology: Hess j1731-347. *A&A*, 531:A81, 2011. doi:10.1051/0004-6361/201016425.

[70] E. Storm, C. Weniger, and F. Calore. SkyFACT: High-dimensional modeling of gamma-ray emission with adaptive templates and penalized likelihoods. *Journal of Cosmology and Astroparticle Physics*, 2017:022–022, Aug 2017. arXiv:1704.02629, doi:10.1088/1475-7516/2017/08/022.

[71] S. Funk. Ground- and space-based gamma-ray astronomy. *Annual Review of Nuclear and Particle Science*, 65(1):245–277, Oct 2015. arXiv:1508.05190, doi:10.1146/annurev-nucl-102014-022036.

[72] A. Strong and I. Moskalenko. Propagation of cosmic-ray nucleons in the galaxy. *The Astrophysical Journal*, 509:212–228, Dec 1998. arXiv:astro-ph/9807150, doi:10.1086/306470.

[73] GALPROP Version 54: Explanatory Supplement. https://galprop.stanford.edu/download/manuals/galprop_v54.pdf. [Online; Accessed: June 28, 2022].

[74] P. M. W. Kalberla et al. The Leiden/Argentine/Bonn (LAB) Survey of Galactic HI. *Astronomy & Astrophysics*, 440(2):775–782, Mar 2005. URL: https://www.aanda.org/articles/aa/abs/2005/35/aa1864-04/aa1864-04.html, doi:10.1051/0004-6361:20041864.

[75] T. M. Dame and P. Thaddeus. A large extension of the cfa galactic co survey, 2003. arXiv:astro-ph/0310102.

[76] A. W. Strong, I. V. Moskalenko, O. Reimer, S. Digel, and R. Diehl. The distribution of cosmic-ray sources in the Galaxy, γ-rays and the gradient in the CO-to-H_2 relation. *Astronomy & Astrophysics*, 422:L47–L50, July 2004. arXiv:astro-ph/0405275, doi:10.1051/0004-6361:20040172.

[77] M. Ackermann et al. Fermi-lat observations of the diffuse γ-ray emission: implications for cosmic rays and the interstellar medium. *The Astrophysical Journal*, 750(1):3, Apr 2012. URL: http://dx.doi.org/10.1088/0004-637X/750/1/3, doi:10.1088/0004-637x/750/1/3.

[78] Personal communication with Katrin Streil.

[79] Personal communication with Kaori Nakashima.

[80] Provided by Emmanuel Moulin.

A. Analysis of the full ROI (HESS I data)

This appendix contains supplementary information on the analysis where HGPS sources, CMZ and 3D background are added as models to the HESS I dataset.

A.1. Background refitting results

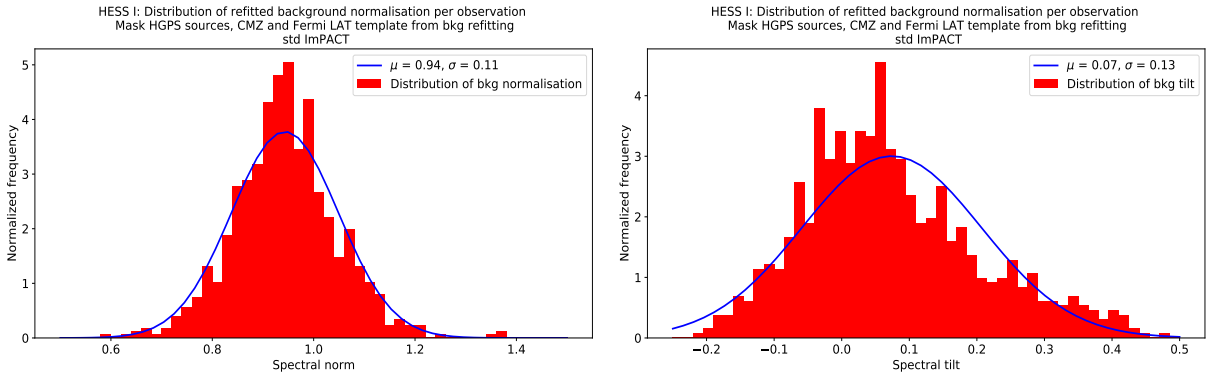

(a) Result for background normalisation

(b) Result for background tilt

Figure A1: HESS I analysis of the full ROI: Distribution of best-fit background model parameters per observation.

A.2. Spectra of the HGPS sources after fitting

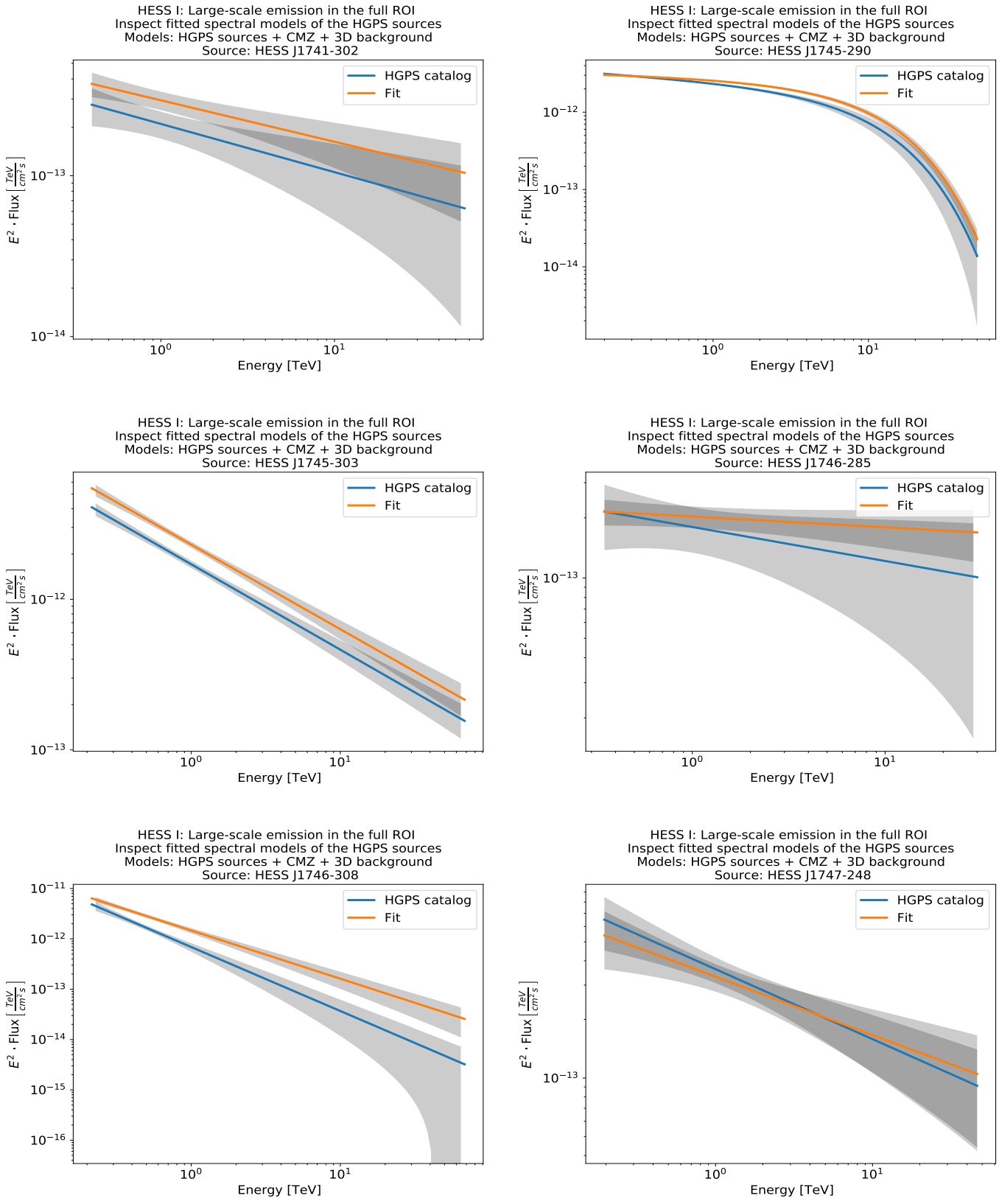

Figure A2: HESS I analysis of the full ROI: Spectra of the HGPS sources (not shown in chapter 5.5) after having applied models for overall background, CMZ and the HGPS sources.

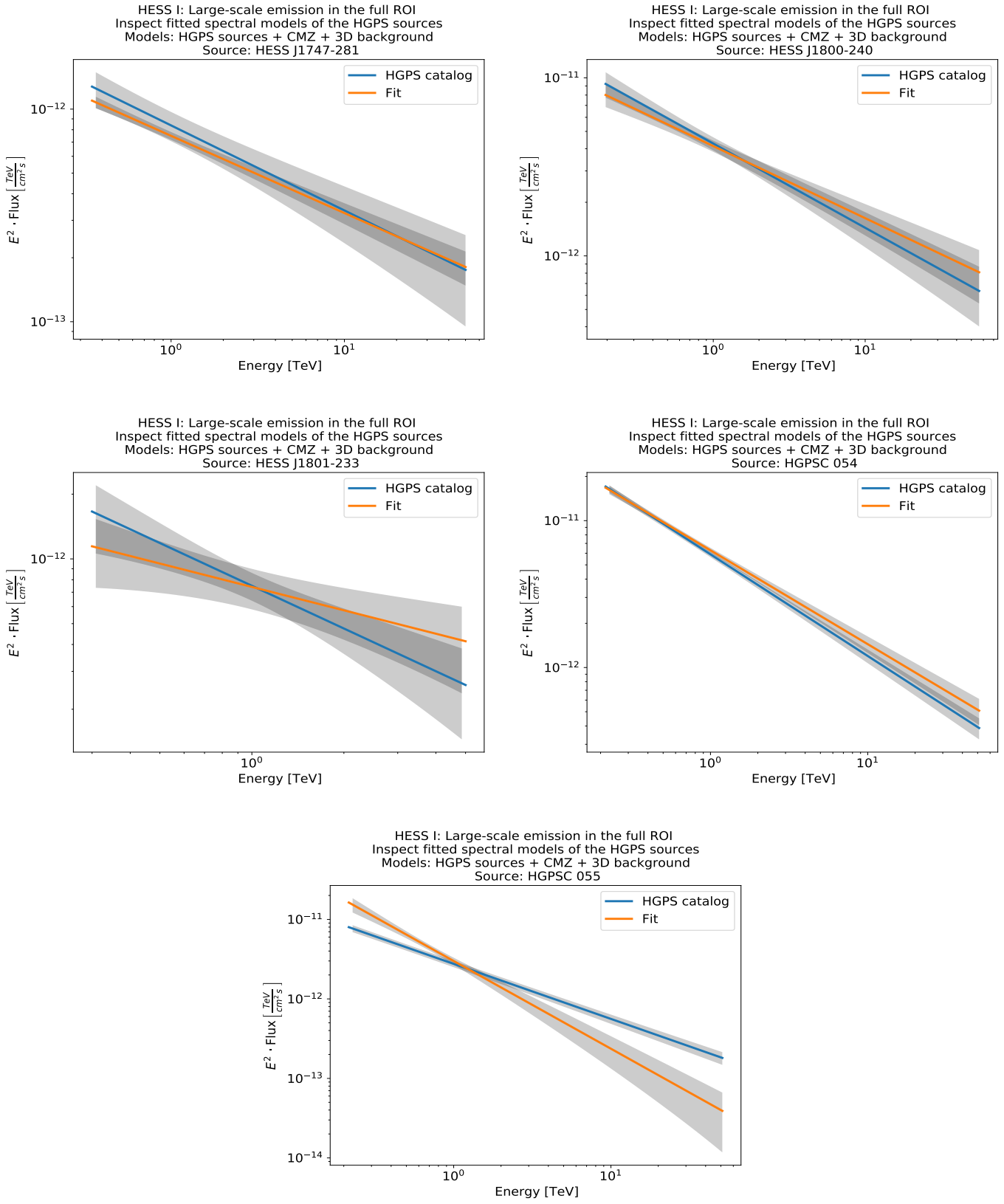

Figure A2: HESS I analysis of the full ROI: Spectra of the HGPS sources (not shown in chapter 5.5) after having applied models for overall background, CMZ and the HGPS sources (continued).

A.3. Residual significance map with HGPS sources labels

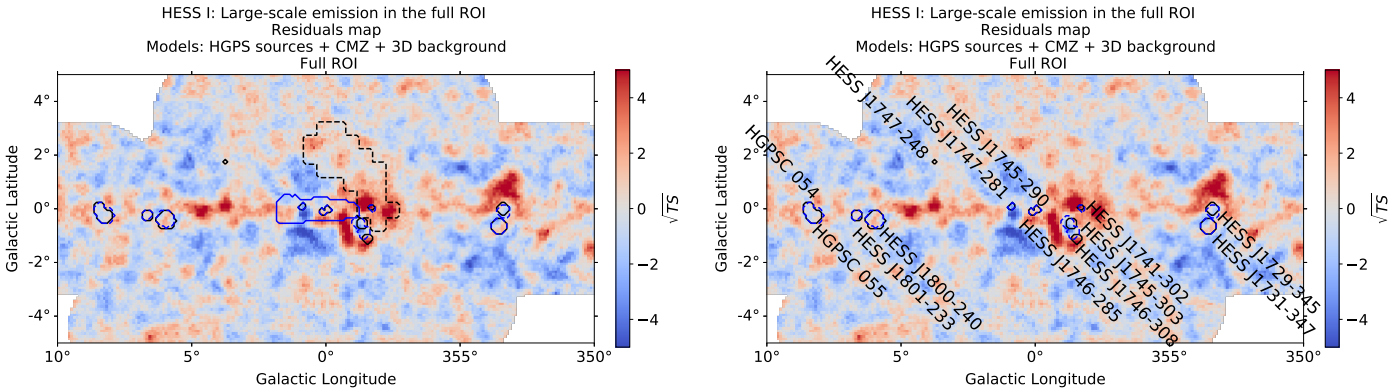

(a) Added contour of the *Fermi*-LAT template

(b) Labelled HGPS sources

Figure A3: HESS I analysis of the full ROI: Residual significance map for the ROI used in this thesis. Same data as shown in figure 21. a) The contour of the *Fermi*-LAT *Fermi* Bubbles template as shown in figure 4 is represented by the black dashed contour. b) Additionally, the names of the HGPS sources in the ROI are added as labels next to their contours for better visualisation.

A.4. Significance estimation of the diffuse emission regions

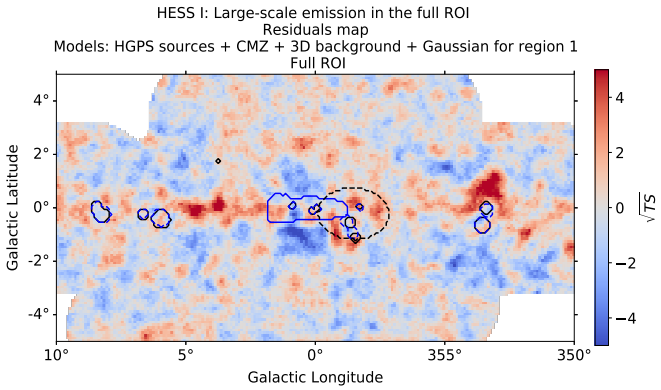

(a) Gaussian for region 1

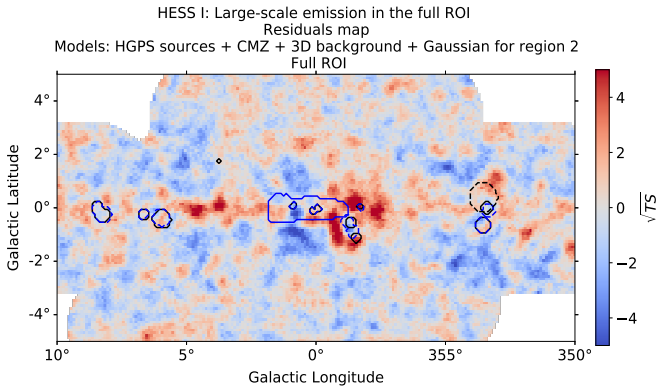

(b) Gaussian for region 2

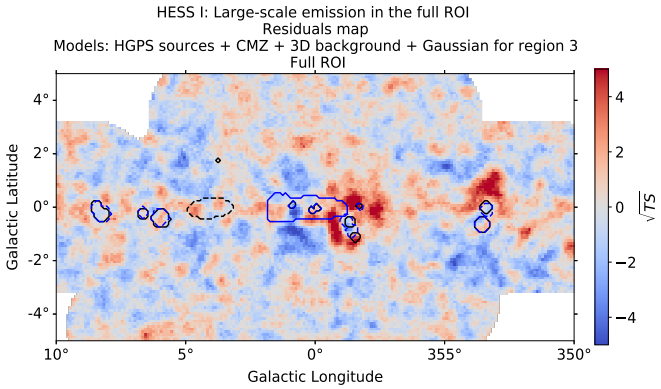

(c) Gaussian for region 3

Figure A4: HESS I analysis of the full ROI: Residual significance maps where each large-scale emission region has been separately described by one Gaussian. The definition of the contours is the same as in figure 21.

A.5. Spatial and spectral parameters of the three Gaussian models

Table A1: HESS I analysis of the full ROI: Fit results for the parameters of the Gaussian spatial models describing the three large-scale emission regions separately.

Region	lon in °	lat in °	σ in °	ϕ in °	e
1	358.52 ± 0.12	-0.23 ± 0.07	1.33 ± 0.05	88 ± 6	0.723
2	353.54 ± 0.08	0.40 ± 0.08	0.27 ± 0.04	90.0	0.001
3	4.06 ± 0.18	-0.03 ± 0.05	0.84 ± 0.08	95 ± 5	0.915

Table A2: HESS I analysis of the full ROI: Fit results for the parameters of the spectral models describing the three large-scale emission regions separately.

Region	Γ	Φ in cm-2 s-1 TeV-1	λ in TeV-1	α	E_0 in TeV
1	2.00 ± 0.03	$(9.17 \pm 0.6) \cdot 10^{-12}$	-	-	1.0
2	1.85 ± 0.10	$(3.1 \pm 0.4) \cdot 10^{-12}$	0.083 ± 0.021	1.0	1.0
3	2.06 ± 0.07	$(3.1 \pm 0.4) \cdot 10^{-12}$	-	-	1.0

B. Analysis of the full ROI (HESS I data): Add three Gaussians

This appendix contains information on the analysis where HGPS sources, CMZ and 3D background as well at three Gaussians at the same time are added as models to the HESS I dataset.

B.1. Spectra of selected HGPS sources after fitting

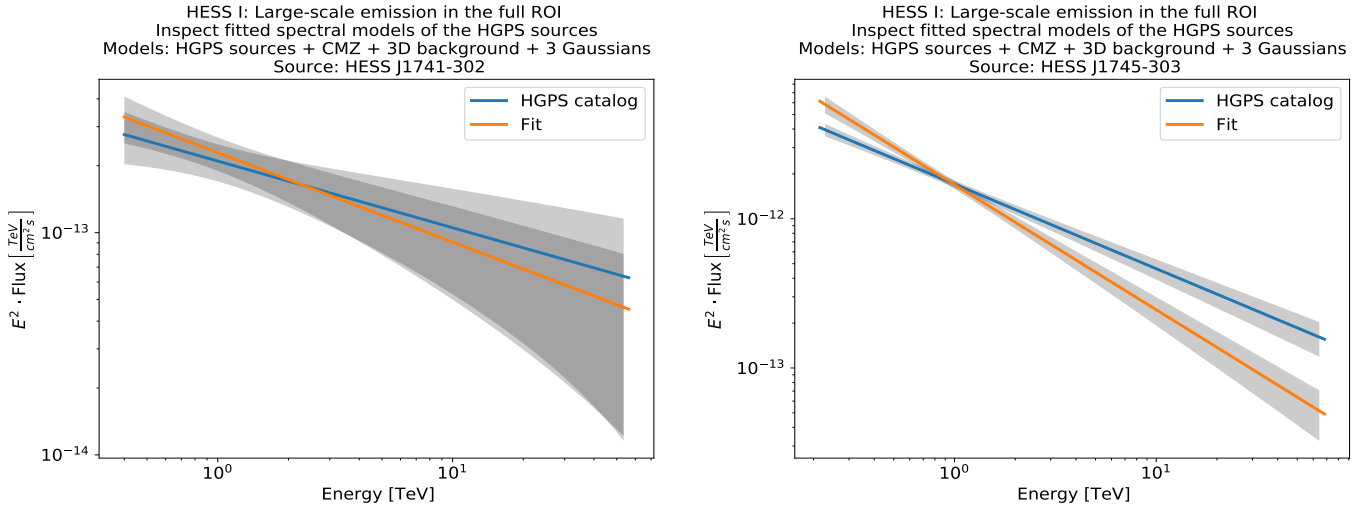

(a) Spectrum of *HESS J1741-302*

(b) Spectrum of *HESS J1745-303*

Figure B1: HESS I analysis of the full ROI: Spectra of the two remaining HGPS sources with remarkably changed spectral parameters when adding the three Gaussian models at the same time. For comparison, the spectra of these sources without added Gaussian spatial models are shown in figure A2 in the previous appendix.

B.2. Best-fit parameters of the three Gaussian models

Table B1: HESS I analysis of the full ROI: Fit results for the parameters of the Gaussian spatial models describing the three large-scale emission regions at the same time.

Region	lon in °	lat in °	σ in °	ϕ in °	e
1	358.48 ± 0.09	-0.24 ± 0.06	1.35 ± 0.04	88 ± 6	0.723
2	353.47 ± 0.06	0.36 ± 0.06	0.626 ± 0.027	90.0	0.001
3	3.75 ± 0.15	-0.00 ± 0.05	1.18 ± 0.08	93 ± 4	0.915

Table B2: HESS I analysis of the full ROI: Fit results for the parameters of the spectral models describing the three large-scale emission regions at the same time.

Region	Γ	Φ in cm-2 s-1 TeV-1	λ in TeV-1	α	E_0 in TeV
1	2.059 ± 0.023	$(1.23 \pm 0.06) \cdot 10^{-11}$	-	-	1.0
2	2.04 ± 0.07	$(6.8 \pm 0.5) \cdot 10^{-12}$	0.067 ± 0.016	1.0	1.0
3	2.09 ± 0.05	$(5.6 \pm 0.5) \cdot 10^{-12}$	-	-	1.0

B.3. Spectral parameters of 3D background and CMZ model

Table B3: HESS I analysis of the full ROI: Fit results for 3D background and CMZ model describing the three large-scale emission regions at the same time.

Model	normalisation	tilt δ
FoVBackgroundModel	0.9989 ± 0.0012	0.0059 ± 0.0014
CMZ model	1.44 ± 0.04	0.0 (fixed)

C. Fit results for HGPS sources in the ROI (HESS I data)

In this appendix, the fit results for the HGPS are shown for the HESS I analysis. Therefore, the best-fit values that have been achieved by fitting HGPS sources, CMZ and 3D background model (colour black) are compared to the best-fit values, when three Gaussian regions are added to the models at the same time (colour blue). The literature values from the HGPS catalog are given below the other two values in brackets.

C.1. Spatial parameters of the fitted HGPS sources

Table C1: HESS I analysis of the full ROI: Comparison of the fitted spatial parameters (Best-fit) of the HGPS sources with the literature values from HGPS catalog [61]. For sources described by Gaussian spatial models, e and ϕ are not printed, since they are fixed to zero for all sources.

Best-fit (ch. 5.5) Best-fit (ch. 6.3) (literature)	lon in °	lat in °	σ in °	radius in °	width in °
HESS J1729-345	353.36 ± 0.04	-0.12 ± 0.04	0.209 ± 0.015	-	-
	353.36 ± 0.04	-0.13 ± 0.04	0.208 ± 0.015	-	-
	(353.39 ± 0.04)	(-0.02 ± 0.05)	(0.19 ± 0.04)	-	-
HESS J1731-347	353.55005 ± 0.00025	-0.66907 ± 0.00022	-	0.257 ± 0.021	0.014
	353.550 ± 0.003	-0.669 ± 0.003	-	0.257 ± 0.021	0.014
	(353.542)	(−0.670)	-	(0.257 ± 0.021)	(0.014)
HESS J1741-302	358.272 ± 0.011	0.017 ± 0.011	-	-	-
	358.272 ± 0.011	0.017 ± 0.011	-	-	-
	(358.277)	(0.049)	-	-	-
HESS J1745-290	359.9421 ± 0.0009	0.0442 ± 0.0009	-	-	-
	359.9421 ± 0.0009	-0.0431 ± 0.0009	-	-	-
	(359.945)	(−0.044)	-	-	-
HESS J1745-303	358.782 ± 0.019	-0.520 ± 0.015	0.197 ± 0.009	-	-
	358.777 ± 0.019	-0.522 ± 0.015	0.195 ± 0.009	-	-
	(358.645 ± 0.030)	(-0.564 ± 0.030)	(0.179 ± 0.021)	-	-
HESS J1746-285	0.119 ± 0.009	-0.137 ± 0.008	-	-	-
	0.119 ± 0.009	-0.137 ± 0.008	-	-	-
	(0.140)	(−0.114)	-	-	-
HESS J1746-308	358.56 ± 0.04	-0.89 ± 0.05	0.193 ± 0.016	-	-
	358.56 ± 0.04	-0.91 ± 0.05	0.192 ± 0.016	-	-
	(358.45 ± 0.04)	(-1.12 ± 0.06)	(0.16 ± 0.04)	-	-
HESS J1747-248	3.805 ± 0.008	1.703 ± 0.008	$(4.42 \pm 0.07) \cdot 10^{-2}$	-	-
	3.805 ± 0.009	1.703 ± 0.008	$(4.649 \pm 0.017) \cdot 10^{-2}$	-	-
	(3.780 ± 0.015)	(1.715 ± 0.016)	(0.061 ± 0.013)	-	-

Table C1 Continued from previous page

Best-fit (ch. 5.5) Best-fit (ch. 6.3) (literature)	lon in °	lat in °	σ in °	radius in °	width in °
HESS J1747-281	0.8644 ± 0.0026	0.0749 ± 0.0025	-	-	-
	0.8644 ± 0.0026	0.0749 ± 0.0025	-	-	-
	(0.872)	(0.076)	-	-	-
HESS J1800-240	5.98 ± 0.04	-0.37 ± 0.04	0.291 ± 0.020	-	-
	5.98 ± 0.04	-0.37 ± 0.04	0.290 ± 0.020	-	-
	(5.96 ± 0.04)	(-0.42 ± 0.04)	(0.32 ± 0.04)	-	-
HESS J1801-233	6.68 ± 0.06	-0.21 ± 0.06	0.160 ± 0.030		
	6.68 ± 0.06	-0.21 ± 0.06	0.160 ± 0.030	-	-
	(6.657)	(-0.268)	(0.17 ± 0.04)	-	-
HGPSC 054	8.446 ± 0.009	-0.012 ± 0.009	0.191 ± 0.005		
	8.446 ± 0.010	-0.012 ± 0.009	0.191 ± 0.005	-	-
	(8.449 ± 0.021)	(0.004 ± 0.024)	(0.195 ± 0.013)	-	-
HGPSC 055	8.210 ± 0.030	-0.262 ± 0.030	0.270 ± 0.015		
	8.206 ± 0.030	-0.262 ± 0.030	0.270 ± 0.015	-	-
	(8.25 ± 0.07)	(-0.29 ± 0.09)	(0.25 ± 0.04)	-	-

C.2. Spectral parameters of the fitted HGPS sources

Table C2: HESS I analysis of the full ROI: Comparison of the fitted spectral parameters (Best-fit) of the HGPS sources with the literature values from HGPS catalog [61].

Best-fit (ch. 5.5) Best-fit (ch. 6.3) (literature)	Γ	Φ in cm-2 s-1 TeV-1	λ in TeV-1	α	E_0 in TeV
HESS J1729-345	2.58 ± 0.09	$(1.38 \pm 0.11) \cdot 10^{-12}$	-	-	1.156
	2.78 ± 0.15	$(8.4 \pm 1.2) \cdot 10^{-13}$	-	-	1.156
	(2.43 ± 0.10)	$((8.3 \pm 0.9) \cdot 10^{-13})$	-	-	(1.156)
HESS J1731-347	2.32 ± 0.05	$(4.89 \pm 0.24) \cdot 10^{-12}$	-	-	0.783
	2.32 ± 0.05	$(4.81 \pm 0.26) \cdot 10^{-12}$	-	-	0.783
	(2.32 ± 0.07)	$((4.67 \pm 0.20) \cdot 10^{-12})$	-	.	(0.783)
HESS J1741-302	2.26 ± 0.13	$(2.9 \pm 0.4) \cdot 10^{-13}$	-	-	1.0
	2.40 ± 0.19	$(2.29 \pm 0.4) \cdot 10^{-13}$	-	-	1.0
	(2.30 ± 0.21)	$((2.1 \pm 0.5) \cdot 10^{-13})$	-	-	(1.0)
HESS J1745-290	2.064 ± 0.022	$(2.79 \pm 0.06) \cdot 10^{-12}$	0.091 ± 0.007	1.0	1.0
	2.076 ± 0.023	$(2.78 \pm 0.06) \cdot 10^{-12}$	0.089 ± 0.007	1.0	1.0
	(2.140 ± 0.021)	$((2.55 \pm 0.05) \cdot 10^{-12})$	(0.093 ± 0.018)	(1.0)	(1.0)

Table C2 Continued from previous page

Best-fit (ch. 5.5) Best-fit (ch. 6.3) (literature)	Γ	Φ in cm-2 s-1 TeV-1	λ in TeV-1	α	E_0 in TeV
HESS J1745-303	2.56 ± 0.06	$(3.33 \pm 0.16) \cdot 10^{-12}$	-	-	0.867
	2.84 ± 0.09	$(2.54 \pm 0.16) \cdot 10^{-12}$	-	-	0.867
	(2.57 ± 0.06)	$((2.47 \pm 0.14) \cdot 10^{-12})$	-	-	(0.867)
HESS J1746-285	2.05 ± 0.08	$(2.04 \pm 0.26) \cdot 10^{-13}$	-	-	1.0
	2.08 ± 0.09	$(1.98 \pm 0.25) \cdot 10^{-13}$	-	-	1.0
	(2.17 ± 0.25)	$((1.8 \pm 0.5) \cdot 10^{-13})$	-	-	(1.0)
HESS J1746-308	2.96 ± 0.13	$(1.23 \pm 0.11) \cdot 10^{-11}$	-	-	0.488
	3.14 ± 0.16	$(1.08 \pm 0.11) \cdot 10^{-11}$	-	-	0.488
	(3.27 ± 0.23)	$((7.2 \pm 0.9) \cdot 10^{-12})$	-	-	(0.488)
HESS J1747-248	2.30 ± 0.16	$(1.90 \pm 0.30) \cdot 10^{-13}$	-	-	1.273
	2.28 ± 0.15	$(1.98 \pm 0.26) \cdot 10^{-13}$	-	-	1.273
	(2.36 ± 0.15)	$((2.1 \pm 0.4) \cdot 10^{-13})$	-	-	(1.273)
HESS J1747-281	2.36 ± 0.05	$(7.49 \pm 0.32) \cdot 10^{-13}$	-	-	1.0
	2.37 ± 0.05	$(7.6 \pm 0.4) \cdot 10^{-13}$	-	-	1.0
	(2.40 ± 0.12)	$((8.4 \pm 1.4) \cdot 10^{-13})$	-	-	(1.0)
HESS J1800-240	2.40 ± 0.08	$(4.6 \pm 0.4) \cdot 10^{-12}$	-	-	0.954
	2.42 ± 0.08	$(4.9 \pm 0.4) \cdot 10^{-13}$	-	-	0.954
	(2.47 ± 0.09)	$((4.8 \pm 0.5) \cdot 10^{-12})$	-	-	(0.954)
HESS J1801-233	2.36 ± 0.24	$(7.4 \pm 1.6) \cdot 10^{-13}$	-	-	1.0
	2.34 ± 0.20	$(8.3 \pm 1.6) \cdot 10^{-13}$	-	-	1.0
	(2.66 ± 0.28)	$((7.5 \pm 1.2) \cdot 10^{-13})$	-	-	(1.0)
HGPSC 054	2.64 ± 0.05	$(1.52 \pm 0.06) \cdot 10^{-11}$	-	-	0.716
	2.64 ± 0.05	$(1.51 \pm 0.07) \cdot 10^{-11}$	-	-	0.716
	(2.69 ± 0.04)	$((1.45 \pm 0.07) \cdot 10^{-13})$	-	-	(0.716)
HGPSC 055	3.10 ± 0.17	$(8.5 \pm 0.8) \cdot 10^{-12}$	-	-	0.716
	2.97 ± 0.16	$(9.0 \pm 0.9) \cdot 10^{-12}$	-	-	0.716
	(2.69 ± 0.04)	$((6.8 \pm 0.7) \cdot 10^{-12})$	-	-	(0.716)

D. Analysis of the full ROI (HESS I data): Add hydrogen templates

D.1. Definition of the galactocentric rings

Table D1: Definition of the galactocentric rings and the conversion factor X_{CO} that is chosen as constant for the used rings.

Ring	Distance in kpc	X_{CO} in 10^{20} s cm-2 K-1 km-1
1	$1.49 - 1.99$	1.5
2	$1.99 - 2.49$	1.5
3	$2.49 - 3.00$	1.5
4	$3.00 - 3.50$	1.5
5	$3.50 - 4.00$	1.5
6	$4.00 - 4.50$	1.5
7	$4.50 - 5.00$	1.5
8	$5.00 - 5.50$	1.5
9	$5.50 - 6.50$	1.5
10	$6.50 - 7.00$	1.5
11	$7.00 - 7.99$	1.5

E. *Fermi* Bubbles analysis

Additional plots (mostly spectra) that were not shown in the main part due to lack of space are presented here.

E.1. Fractional residuals distributions for std zeta analysis

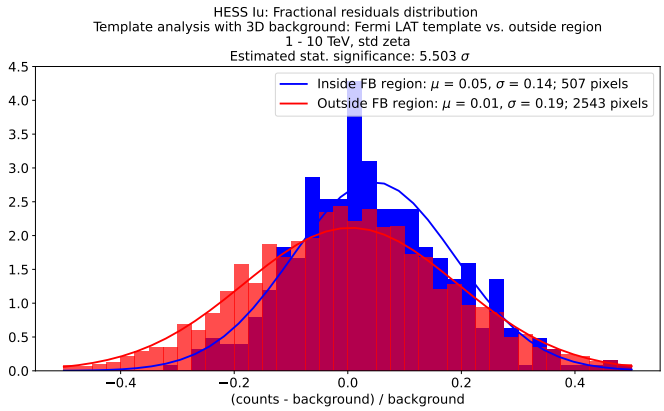

(a) std zeta + Fermi LAT template (in vs. out)

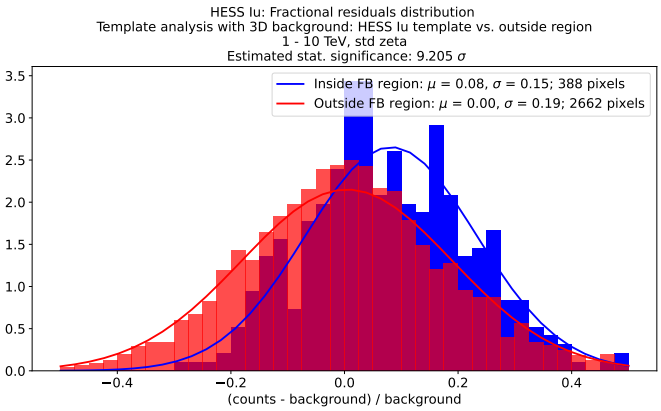

(b) std zeta + HESS Iu template (in vs. out)

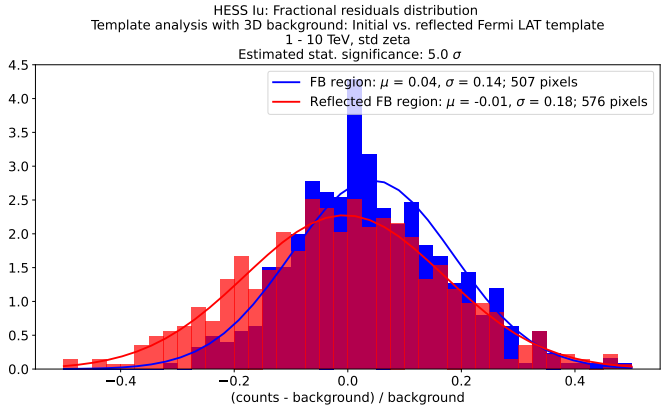

(c) std zeta + Fermi LAT template (in vs. refl.)

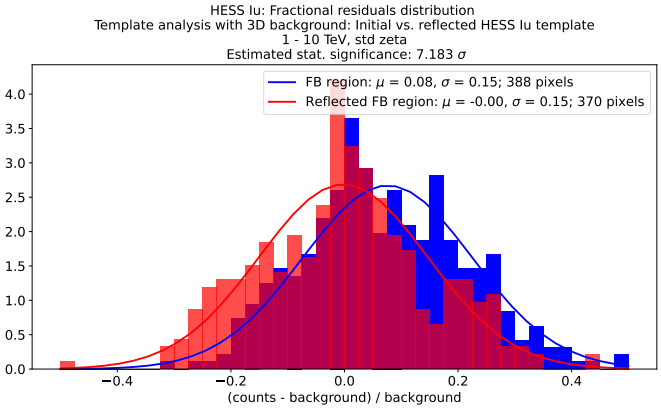

(d) std zeta + HESS Iu template (in vs. refl.)

Figure E1: *Fermi* Bubbles template analysis with HESS Iu data: Fractional residuals distributions for *Fermi*-LAT and HESS Iu template using the std zeta analysis.

E.2. Additional spectra for HAP HESS Iu analysis

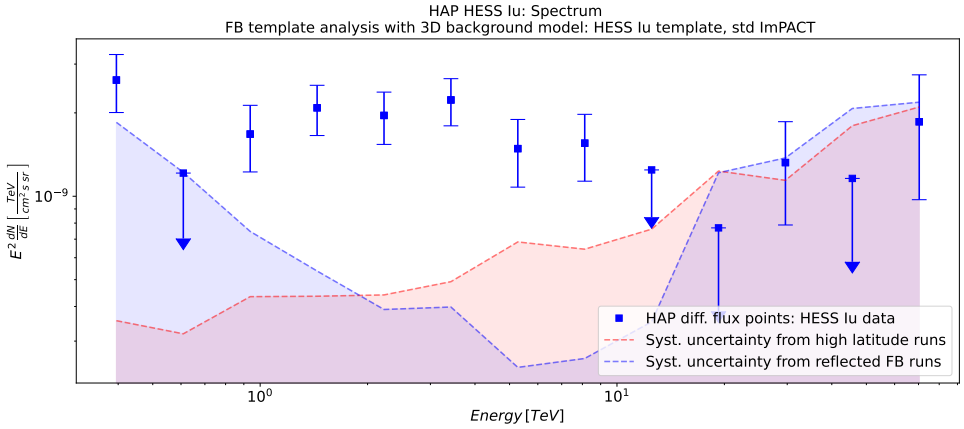

(a) std ImPACT

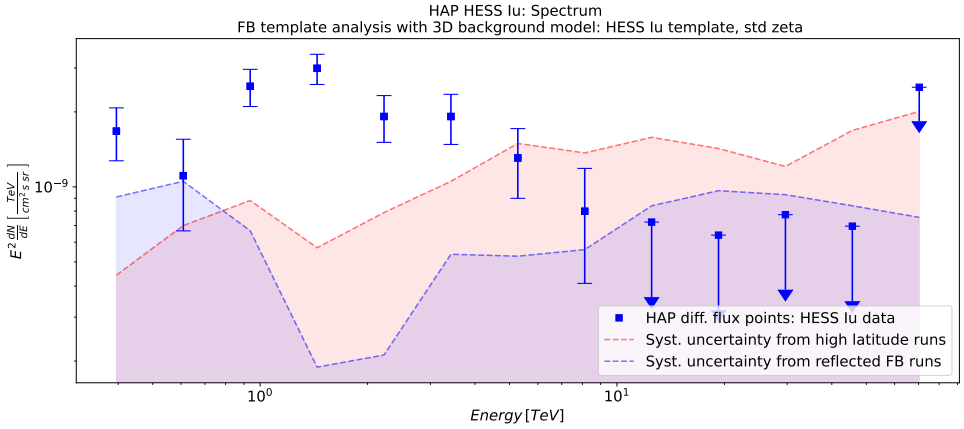

(b) std zeta

Figure E2: *Fermi* Bubbles template analysis with HESS Iu data: Additional spectra achieved with the HESS Iu *Fermi* Bubbles template. Systematic uncertainty bands are added.

E.3. Additional spectra for HAP HESS I analysis

The systematic uncertainty band for high latitude runs is computed based on 3255 (std ImPACT) and 3307 (std zeta) HESS I runs.

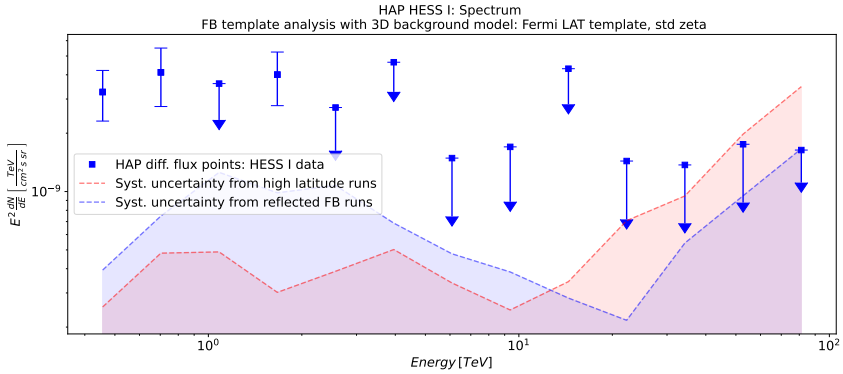

(a) std zeta + Fermi LAT template

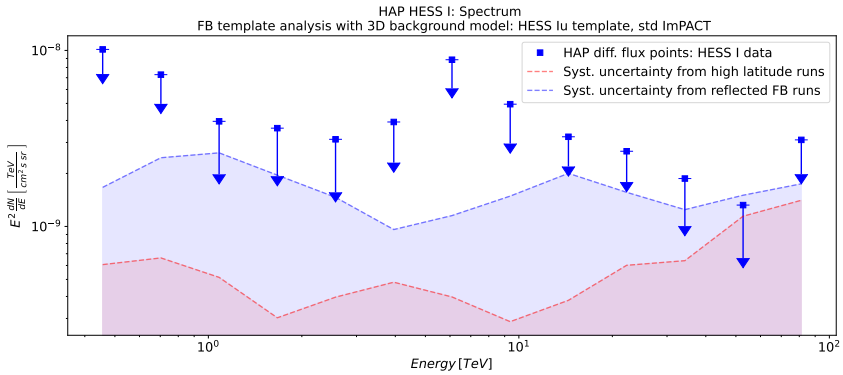

(b) std ImPACT + HESS Iu template

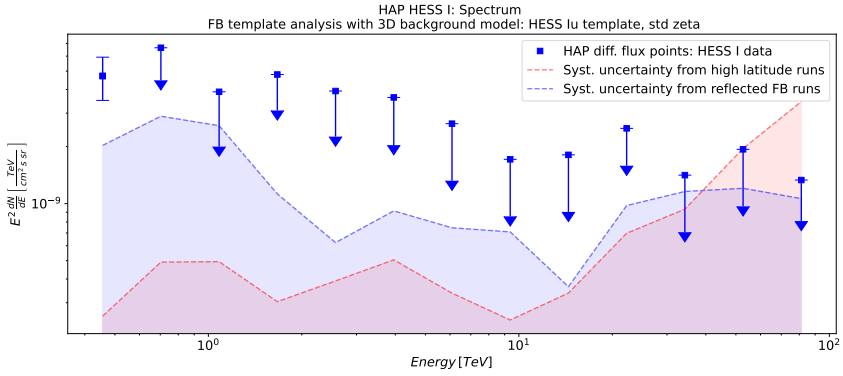

(c) std zeta + HESS Iu template

Figure E3: *Fermi* Bubbles template analysis with HESS I data: Additional spectra with systematic uncertainty bands.

E.4. Additional spectra for HAP HESS II analysis

The systematic uncertainty band for high latitude runs is computed based on 670 (std ImPACT) and 688 (std zeta) HESS II runs.

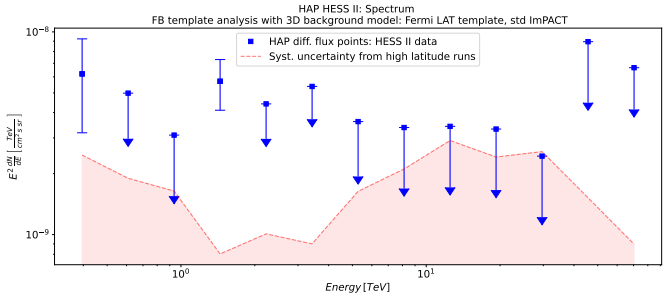

(a) std ImPACT + Fermi LAT template

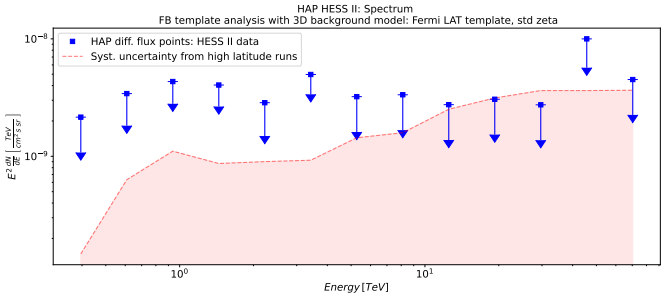

(b) std zeta + Fermi LAT template

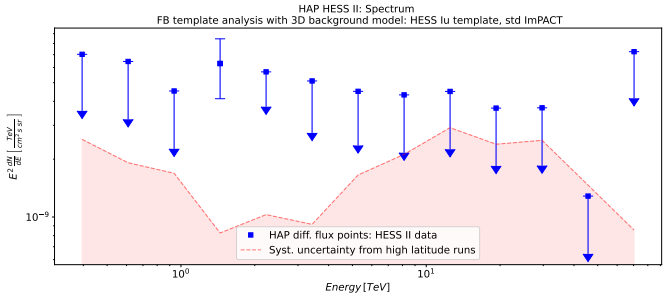

(c) std ImPACT + HESS Iu template

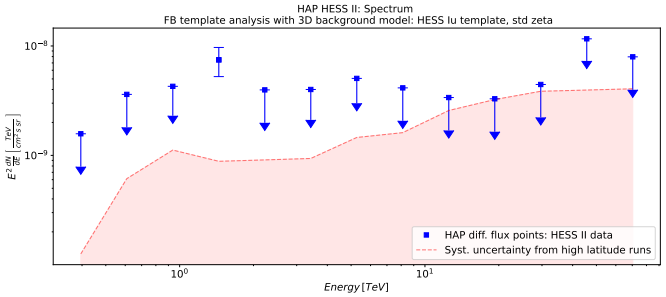

(d) std zeta + HESS Iu template

Figure E4: *Fermi* Bubbles template analysis with HESS II data: Additional spectra with systematic uncertainty bands.

E.5. Additional spectra for HAP stacked HESS I, II and Iu analysis

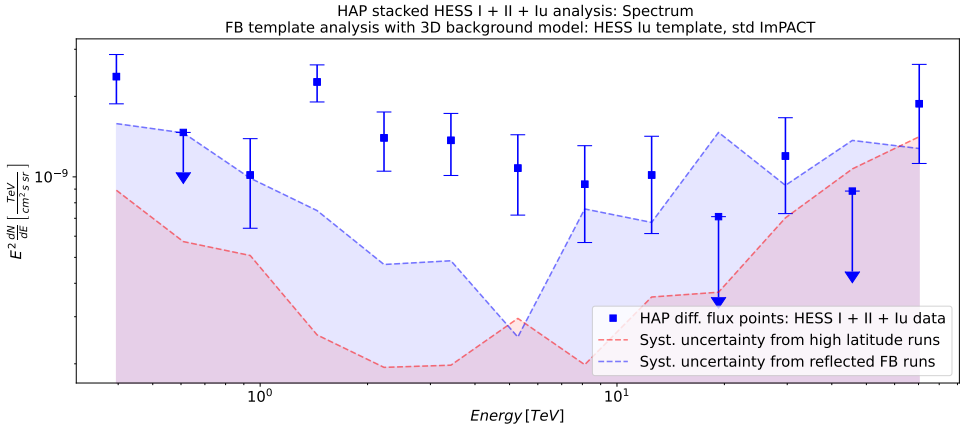

(a) std ImPACT

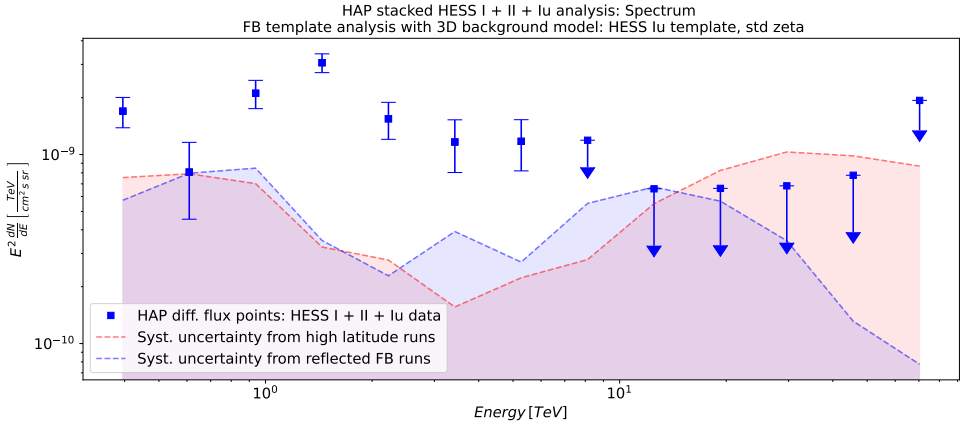

(b) std zeta

Figure E5: HAP stacked HESS I, II and Iu spectra with systematic uncertainty bands for the HESS Iu template.

E.6. Uncertainty estimation: Background manipulation

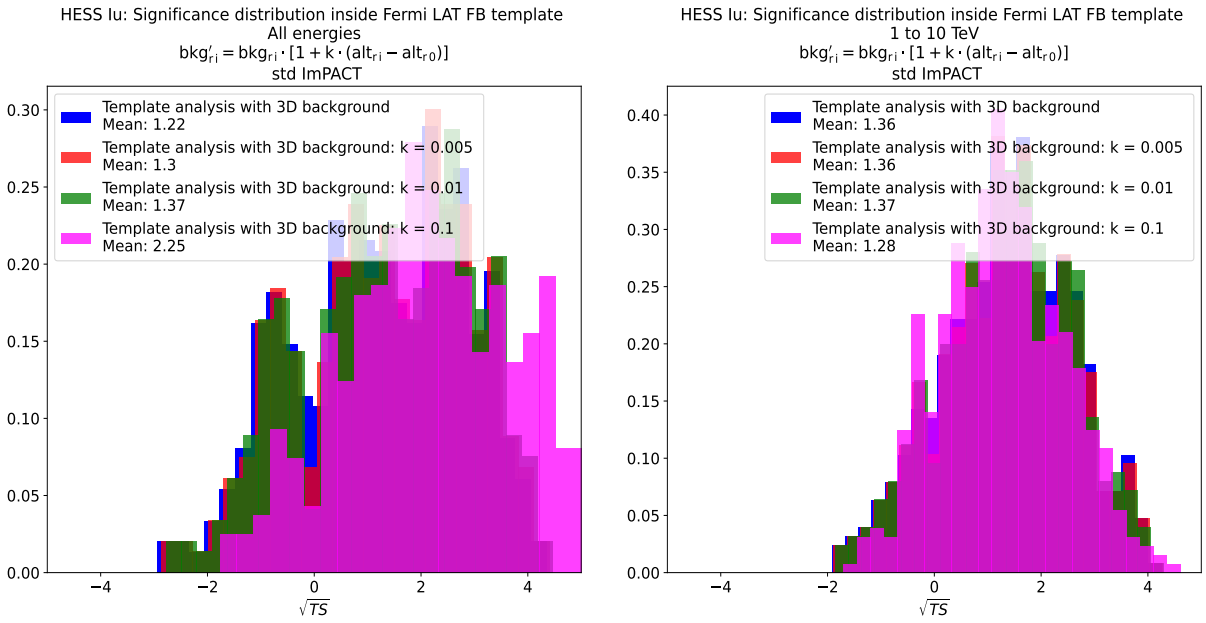

(a) Summed over all energies

(b) 1 - 10 TeV

Figure E6: *Fermi* Bubbles template analysis using HESS Iu data: $\sqrt{TS}$ distribution in the *Fermi*-LAT *Fermi* Bubbles ROI for the stacked dataset with and without manipulated background of single observations before refitting using std ImPACT algorithm. The plus case is shown.

F. Analysis of the ROI (HESS Iu data)

This appendix contains supplementary information on the analysis where HGPS sources, CMZ and 3D background are added as models to the HESS Iu dataset.

F.1. Background refitting per observation

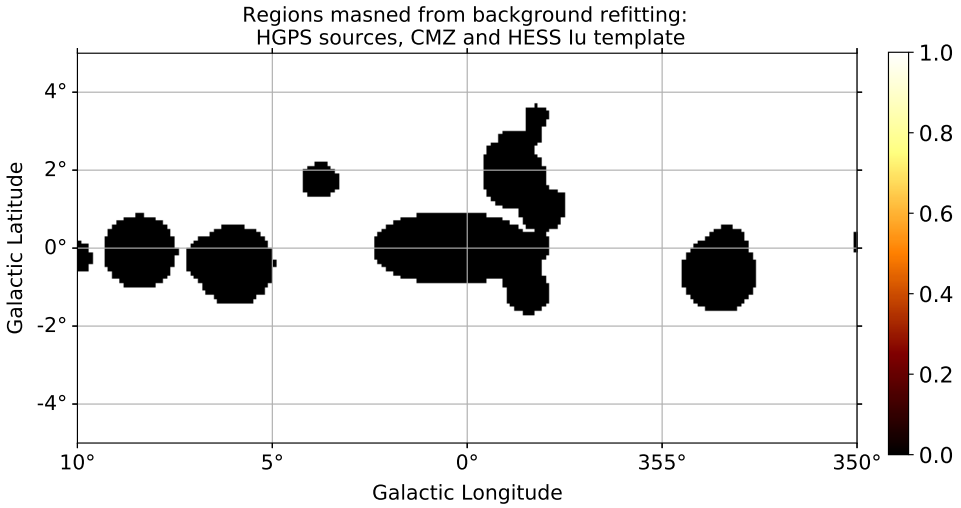

Figure F1: Exclusion mask around HGPS sources, CMZ and the HESS Iu residuals based template.

Template	std ImPACT		std zeta	
	bkg norm	bkg tilt	bkg norm	bkg tilt
Fermi LAT	0.92 ± 0.11	0.03 ± 0.09	0.96 ± 0.11	0.02 ± 0.08
HESS Iu	0.92 ± 0.11	0.03 ± 0.09	0.96 ± 0.11	0.02 ± 0.08

Table F1: HESS Iu analysis of the full ROI: Bkg refitting results for the different *Fermi* Bubbles templates and reconstruction algorithms.

F.2. Best-fit parameters of the *Fermi* Bubbles models

Table F2: HESS Iu analysis of the full ROI: Fit results for the parameters of the Gaussian spatial models of the *Fermi* Bubbles models. ϕ is fixed to 0° and e to 0 as the Gaussian is symmetric. Thus, both parameters are not listed here.

Configuration	lon in °	lat in °	σ in °
std ImPACT + Fermi LAT template	358.69 ± 0.13	0.50 ± 0.15	0.49 ± 0.06
std ImPACT + HESS Iu template	358.66 ± 0.16	0.53 ± 0.15	0.49 ± 0.06
std zeta + Fermi LAT template	358.77 ± 0.08	0.46 ± 0.07	0.493 ± 0.027

Table F3: HESS Iu analysis of the full ROI: Fit results for the parameters of the power law spectral models with exponential cutoff of the *Fermi* Bubbles models. α is fixed to 0 and E_0 to 0 TeV. Thus, both parameters are not listed here.

Region	Γ	Φ in cm-2 s-1 TeV-1	λ in TeV-1
std ImPACT + Fermi LAT template	1.64 ± 0.23	$(3.1 \pm 0.4) \cdot 10^{-12}$	0.13 ± 0.06
std ImPACT + HESS Iu template	1.68 ± 0.10	$(3.2 \pm 0.4) \cdot 10^{-12}$	0.125 ± 0.024
std zeta + Fermi LAT template	1.60 ± 0.12	$(3.6 \pm 0.5) \cdot 10^{-12}$	0.19 ± 0.04

G. Exposure maps

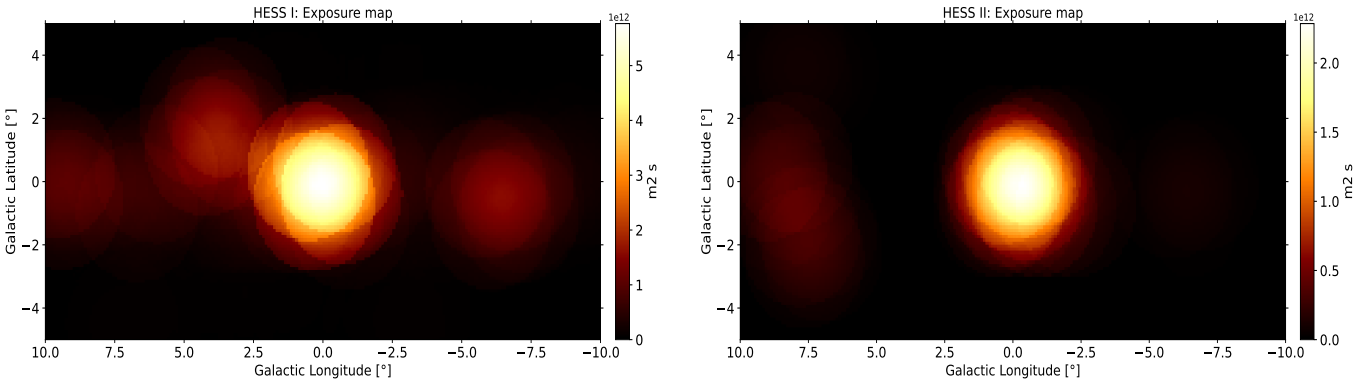

(a) HESS I

(b) HESS II

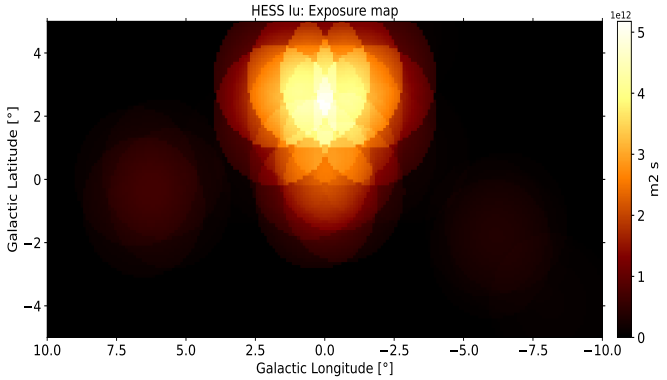

(c) HESS Iu

Figure G1: Exposure maps for the different H.E.S.S. eras

Acknowledgements

Last but not least, I would like to thank everyone who supported me in writing this thesis:

- **Prof. Dr. Stefan Funk** for offering this exciting topic and the helpful suggestions in our 3D Analysis Meetings.
- **Dr. Dmitry Malyshev** for answering all the questions that I've asked, coming up with lots of suggestions and proofreading. Thank you for motivating and supporting me throughout my thesis!
- The whole **gamma group from ECAP** for critical questions, comments and suggestions in the 3D Analysis Meetings. And thanks for the great time in Austria and Paris!
- The **H.E.S.S. *Fermi* Bubbles group** (Alessandro Montanari, Emmanuel Moulin, Denys Malyshev and Dmitry Malyshev) for the huge amount of input and comments in our weekly meetings on Friday motivating me to update the results for the next meeting.

A big thank to all of **my friends** for distracting from everyday stress, spending lots of wonderful days with irreplaceable memories and always having an open ear to listen to the stories of my failures, not only during my master's thesis, but all of my physics studies. Most of the time you even had useful words of wisdom!
Finally, I want to thank **my family** for always being there and supporting me during my studies. When I started studying physics almost six years ago, I never thought I would make it this far. But I struggled through, even if I sometimes took my frustrations out on you. Without you, none of this would have been possible!

Erklärung

Hiermit versichere ich, dass ich die vorliegende Arbeit selbständig und ohne unerlaubte Hilfsmittel verfasst habe.
Ich habe keine anderen als die angegebenen Quellen und Hilfsmittel benutzt und alle wörtlich oder dem Sinn nach aus anderen Texten entnommenen Stellen als solche kenntlich gemacht. Dies gilt für gedruckte Texte wie für Texte aus dem Internet.

Erlangen, 1.7.2022 Fabian Richter